



TECHNISCHE
UNIVERSITÄT
WIEN
Vienna | Austria



Master Thesis

Analysis of reconstituted and native collagen fibrils modified by mineralization

carried out for the purpose of obtaining a degree of Master of Science (MSc or Dipl.-Ing. or DI),
submitted at TU Wien, Faculty of Mechanical and Industrial Engineering, by

Arpad Bakonyi

Mat.Nr.: 0926406

under the supervision of

Andreas Rohatschek, Univ.Ass., Dipl.-Ing,

Philipp Thurner, Univ.Prof. Dipl.-Ing. Dr.sc.nat.

Institute of Lightweight Design and Structural Biomechanics, E317

Vienna, October 2020

Affidavit

I declare in lieu of oath, that I wrote this thesis and performed the associated research myself, using only literature cited in this volume. If text passages from sources are used literally, they are marked as such.

I confirm that this work is original and has not been submitted elsewhere for any examination, nor is it currently under consideration for a thesis elsewhere.

City, Date

Signature

Abstract

Collagens are the most abundant and structurally the most important proteins of the human extracellular matrix. Therefore, the mechanical properties of the collagen building blocks, that are collagen fibrils in mineralized and non-mineralized form, are of crucial importance. In spite of their important role, the mineralization process of collagen fibrils *in vitro* as it relates to the mechanical properties has not been studied comprehensively. In this study, the mechanical properties of *in vitro* mineralized native and reconstituted collagen fibrils were investigated at different stages of mineralization using Atomic Force Microscopy (AFM) based nanoindentation. A measurement protocol was developed which allows the investigation of several fibrils within the same measurement run. First, native and reconstituted fibrils were selected and imaged using AFM in the contact mode. Second, fibrils were preconditioned in PBS buffer at 37 °C, for either 2h or 48h. Third, indentation force maps of the already selected fibrils were measured in contact mode in PBS at sample areas of 1 x 2 µm. Fourth, the mineralization process was initiated by adding a mineralization buffer and, fifth, force maps in contact mode were taken after 20h, 40h, and 60h of mineralization time. Per force map, 16 indentation points on the longitudinal axis and at least 10 indentation points on the cross-sectional axis of the fibril were measured. A custom-built Matlab script was used for the analysis of the indentation data (depth, deflection, reaction force), and the calculated modulus. The mechanical properties of samples across the mineralization stages were compared. The results suggest that a sample of reconstituted fibrils could well resemble the mechanical properties of native fibrils, and even provide less variance among fibrils compared to native samples. As a result of the mineralization procedure, crystal formation was detected on the fibrils in all samples. The presence of intrafibrillar mineralization was suggested by the results but could not be significantly verified. EDTA was successfully used after some mineralization steps to clear off surface crystallization, but may have also influenced intrafibrillar mineral deposits. It was found, that pre-conditioning in PBS significantly reduced the subsequent softening behavior, which may partially suppress the stiffening effect of mineralization. Additionally, important methodological developments emerged from the study, such as the use of a mica disc for the sensitivity calibration of the AFM, as well as an iterative method for the choice of the cantilever. Overall, the use of AFM nanoindentation with a sharp pyramidal tip proved to impose frequent complications when measuring mineralized fibrils. Tensile tests might be a more promising alternative in future studies.

Kurzzusammenfassung

Kollagene sind die häufigsten und strukturell sowie mechanisch wichtigsten Proteine der menschlichen extrazellulären Matrix. Daraus ergibt sich, dass die mechanischen Eigenschaften der Grundbausteine in der hierarchischen Struktur der Gewebe, der sogenannte Kollagenfibrillen in mineralisierter sowie nicht mineralisierter Form, von entscheidender Bedeutung sind. Generell gibt es wenig wissenschaftliche Daten in Bezug auf die mechanischen Eigenschaften von Kollagenfibrillen; insbesondere liegen für mineralisierte Kollagenfibrillen überhaupt keine Daten vor. In diesem Zusammenhang ist auch der *in vitro* Mineralisierungsprozess von Kollagenfibrillen in Bezug auf deren mechanischen Eigenschaften noch nicht untersucht worden. Daher war es das Ziel dieser Arbeit, die mechanischen Eigenschaften von *in vitro* mineralisierten nativen und rekonstituierten Kollagenfibrillen in verschiedenen Mineralisierungsstadien unter Verwendung von Rasterkraftmikroskopie (AFM) im Nanoindentationsmodus zu untersuchen. Hierfür wurde ein Messprotokoll entwickelt, welches die Untersuchung mehrerer Fibrillen innerhalb der gleichen Messreihe erlaubt. Zunächst wurden hier native und rekonstituierte Fibrillen selektiert und unter Verwendung von AFM im Kontaktmodus abgebildet. In weiterer Folge wurden diese selektierten Fibrillen zuerst in PBS-Puffer bei 37 °C für entweder 2 Stunden oder 48 Stunden vorkonditioniert. Danach wurden von den bereits ausgewählten Fibrillen mittels AFM Nanoindentation sogenannte Indentationskarten in PBS auf einer Probenfläche von $1 \times 2 \mu\text{m}$ aufgenommen. Danach wurde der Mineralisierungsprozess durch Hinzufügen einer Mineralisierungslösung eingeleitet. Darauffolgend wurden weitere Indentationskarten entweder sofort nach Initialisierung der Mineralisierung oder nach 20, 40 und 60 Stunden Mineralisierungszeit gemessen. Pro Indentationskarte wurden 16 Indentationspunkte auf der Längsachse, und mindestens 10 auf der Querschnittsachse der Fibrille gemessen. Für die Analyse der Messdaten wurde ein Matlab-Skript verwendet um Fibrillenhöhe sowie Indentationsmodul zu berechnen. Die mechanischen Eigenschaften der Proben wurden über die einzelnen Mineralisierungsstufen hinweg verglichen. Die Ergebnisse zeigen, dass rekonstituierte Fibrillen den mechanischen Eigenschaften nativer Proben ähneln und eine geringere Variation des Indentationsmoduli zwischen verschiedenen Fibrillen aufweisen. Der Mineralisierungsprozess hat offensichtlich Kristallbildung auf der Oberfläche von Fibrillen zur Folge. Das Vorhandensein einer intrafibrillären Mineralisierung wurde durch die Ergebnisse nahegelegt, konnte jedoch nicht mit statistischer Genauigkeit nachgewiesen werden.

EDTA wurde nach einigen Mineralisierungsschritten zur wirkungsvollen Reinigung von auftretenden Oberflächenkristallen eingesetzt, konnte aber gegebenenfalls auch intrafibrilläre Mineralablagerungen reduzieren oder ganz auflösen. Im Zuge der Arbeit konnte eine signifikante Reduzierung der Indentationssteifigkeit aufgrund von Vorkonditionierung in PBS nachgewiesen werden, was ebenfalls einen Versteifungseffekt durch Mineralisierung verschleiern könnte. Trotz der aufgetretenen Probleme wurden in dieser Arbeit wichtige methodische Weiterentwicklungen erarbeitet, wie z.B. die Verwendung von Glimmer für die Kalibrierung der Cantilever-Sensitivität, sowie eine iterative Methode zur Auswahl geeigneter Cantilever. Die ermittelten Zusammenhänge, sowie die methodischen Weiterentwicklungen werden insgesamt einen wertvollen Beitrag für zukünftige mechanische Untersuchungen an mineralisierten Kollagenfibrillen leisten.

Acknowledgement

Most importantly, I would like to thank my advisor, Univ-Ass. Andreas Rohatschek for the supervision and guidance of my thesis.

I would like to express my deepest gratitude to my second advisor, Prof. Philipp Thurner, Dr.sc.nat, for his guidance during my entire work, his valuable comments on this thesis, and for the management of the Biomedical Engineering courses as the study dean at the Vienna University of Technology.

I would also express my gratitude to the Vienna University of Technology, for providing the infrastructure and laboratory equipment and for the organizational support.

Additionally, I would like to express my appreciation to my colleagues in the work group, Univ-Ass. Mathis Nalbach for his valuable advice during my experiments, and Senior Scientist Orestis Andriotis, PhD, for the proper lab management and for providing his important and wide-ranging expertise.

Finally, I would like to express my gratitude towards my parents for their unconditional support and encouragement throughout my years of study, along with my entire family and friends for motivating me. This accomplishment would not have been possible without them. Thank you.

Abbreviations

ACP – Amorphous calcium phosphate
AFM – Atomic force microscopy
BMD – Bone mineral density
BMDD – Bone mineral density distribution
CaP – Calcium-Phosphate
DW – Distilled water
ECM – Extracellular matrix
EDTA – Ethylenediamine-tetraacetic acid
GAG - Glycosaminoglycan
HA – Hydroxyapatite
InvOLS – Inverse optical lever sensitivity
MCF – Mineralized collagen fibril
MEMS – Micro-electro-mechanical system
NCP – Non-collagenous protein
OLS – Optical lever sensitivity
PSD – Power spectral density
PG – Proteoglycan
PLL – Poly-l-lysine
QI – Quantitative Imaging ©
SD – Standard Deviation
TC – Tropocollagen

Table of contents

Abstract	I
Kurzzusammenfassung.....	II
Acknowledgement	IV
Abbreviations.....	V
Table of contents.....	VI
1. Introduction.....	1
1.1. Motivation.....	1
1.2. Aim of the study	1
1.3. Structure of the thesis	2
2. Background.....	3
2.1. Human tissue.....	3
2.1.1. Skeletal tissue	3
2.1.1.1. Tendons and ligaments.....	3
2.1.1.2. Bone tissue.....	5
2.1.2. Connective tissue	9
2.2. Collagen fibril	10
2.2.1. Composition of collagen fibrils.....	11
2.2.2. Collagen fibrillogenesis	12
2.2.3. Mineralized collagen fibrils.....	14
2.2.3.1. Controlling collagen mineralization.....	15
2.2.4. Mechanical properties of collagen fibrils.....	15
2.2.4.1. Native collagen fibril mechanics.....	15
2.2.4.2. Determinants of collagen fibril mechanics.....	16
2.2.4.3. Mineralized collagen fibril mechanics	17
2.3. Previous studies on collagen mechanics.....	17
3. Methods	19
3.1. Sample preparation.....	19
3.1.1. Native fibril extraction	19
3.1.2. Mineralization.....	20
3.1.3. Control mineralization	21
3.1.4. Phosphate-buffered-saline solution.....	21
3.2. The concept of AFM experiments on collagen fibrils.....	21
	VI

3.2.1.	The principles of AFM nanoindentation.....	22
3.2.1.1.	Optical lever.....	23
3.2.1.2.	Indentation process.....	25
3.2.2.	AFM nanoindentation in practice.....	26
3.2.2.1.	Essential instrument settings.....	26
3.2.2.2.	Calibration of the optical lever sensitivity (OLS).....	27
3.2.2.3.	Tip stiffness and the reference slope.....	28
3.2.3.	Application of AFM imaging and indentation of collagen fibrils.....	28
3.3.	AFM measurements applied in this thesis.....	29
3.3.1.	The used AFM equipment.....	29
3.3.2.	Instrument settings.....	31
3.3.3.	Employed working modes of the AFM.....	32
3.3.3.1.	Imaging.....	32
3.3.3.2.	Quantitative Imaging (QI).....	32
3.3.3.3.	Force mapping.....	33
3.3.4.	DZ-relation and the reference slope.....	34
3.3.5.	Calibration for sensitivity and determination of spring constant.....	34
3.3.5.1.	Sensitivity in air.....	35
3.3.5.2.	Measurement of cantilever spring constant.....	35
3.3.5.3.	Sensitivity in PBS.....	35
3.3.6.	Choice of cantilever.....	37
3.3.6.1.	Measurement algorithm for the choice of cantilever.....	38
3.3.7.	Cantilever tip shape determination.....	40
3.4.	Problems affecting the measurements.....	41
3.4.1.	Fibril identification.....	41
3.4.2.	Measurement of the reference slope and calibration of sensitivity.....	42
3.4.3.	Contaminations on the fibril.....	44
3.4.4.	Laser interference.....	45
3.4.5.	Indentation depth.....	46
3.4.6.	Fibril softening.....	46
3.5.	Final measurement protocol.....	47
3.5.1.	Additional experiments.....	49
4.	Data analysis.....	53
4.1.	Measurement preferences.....	53

4.1.1.	Reference slopes	53
4.1.2.	Cantilever tip shape.....	53
4.2.	Sample analysis	55
4.2.1.	Morphology	55
4.2.2.	Indentation modulus.....	56
5.	Results	59
5.1.	Sample preparation.....	59
5.1.1.	Reconstituted fibril resources.....	59
5.1.2.	Native fiber dissection	59
5.2.	Fibril morphology.....	60
5.2.1.	Comparison of reconstituted and native fibril morphologies.....	60
5.2.2.	Fibril swelling behavior	62
5.2.2.1.	D-banding appearance	63
5.2.3.	Morphology of mineralized fibrils.....	64
5.2.3.1.	Morphology in control mineralization (Min0).....	64
5.2.3.2.	Morphology in mineralization	66
5.3.	Mechanical properties.....	69
5.3.1.	Comparison of unmodified reconstituted and native fibrils.....	69
5.3.2.	The effect of mineralization	69
5.3.3.	Reconstituted fibrils (R5) in different mineralization stages	70
5.3.4.	Native fibril (N5) in different mineralization stages.....	71
5.3.5.	The effect of the Min0 step (A1)	72
5.3.6.	The effect of the preconditioning (A2-A3)	72
6.	Discussion.....	75
6.1.	Interpreting the results	75
6.1.1.	Assessment of the morphology.....	75
6.1.2.	Effect of hydration.....	76
6.1.3.	Assessment of mechanical properties	77
6.2.	Methodology	78
6.2.1.	Control mineralization	78
6.2.2.	Contaminations.....	79
6.2.3.	Adhesion of native fibril samples	80
6.2.4.	Appropriate substrate for reference slope and sensitivity calibration.....	80
6.2.5.	Interference in the optical lever mechanism.....	82

6.2.6. Indentation depth	82
6.2.7. Data analysis algorithm.....	83
6.3. Assumptions.....	85
7. Conclusion	87
Bibliography.....	89
Annex A – Mineralization protocol	
Annex B – Reconstitution protocol	

1. Introduction

Collagen is not only the most abundant protein in the human body, but also the most important extracellular structural component of human tissues, providing passive mechanical function, and determining the shape of organs. One of the unique features of collagen is its hierarchical organization into multi-level structures. The mechanical function of these structures originate from the biomechanical properties of collagen fibrils. Hence, there is a fundamental need to determine these at different scales and levels of hierarchy. The detailed mechanical examination of collagen fibrils is not only essential for the macroscopic analysis of tissue biomechanics, but also contributes to a better understanding of the micro-structure of collagen fibrils themselves.

1.1. Motivation

It is widely accepted that the bone mineral content directly relates to the hardness and stiffness of bone [1]–[3]. Meanwhile, on the microstructural level, a direct proof of the influence of mineral content on the mechanical properties of mineralized collagen fibrils (MCFs) is still missing. The key length scale to understand bone mechanics, fracture mechanics and scaffold architectures is the submicroscale, represented by MCFs [4].

In general, a solid knowledge about the mechanical properties of the lowest hierarchical level of bone can contribute to the development of collagen biomaterials and synthetic grafts, and to a better understanding of bone fractures. Today's existing models for synthetic scaffolds use an arbitrary value for the fibril stiffness [5], lacking experimental data. With the help of models using experimentally sourced inputs, synthetic scaffolds can be developed more effectively.

The experimental observation of MCF mechanical properties still represents a gap in basic knowledge. Therefore, a robust methodology to test MCFs is desired.

1.2. Aim of the study

The primary purpose of this study is to produce MCFs *in vitro* with the help of an established mineralization protocol, and to verify the production methodology itself by subsequent mechanical testing of the MCFs. An additional, essential goal of these experiments is the extraction of mechanical properties of single MCFs, which has not been done yet.

Reconstituted and native Type I collagen fibrils shall be measured in their unmodified state and after repeated steps of mineralization *in vitro*. The mechanical properties of the fibrils shall be examined by nanoindentation using Atomic Force Microscopy (AFM) in different stages of mineralization. By AFM, the indentation modulus of the fibrils can be assessed.

The elementary expected outcome of the tests is then a change in mechanical properties of the fibrils across multiple mineralization stages, expecting a converging behavior towards a characteristic end value of indentation modulus, verifying the mineralization methodology. The final mineralized state of reconstituted and native fibrils can be also compared to draw conclusions about the reproducibility and applicability of mineralized reconstituted fibrils.

1.3. Structure of the thesis

This master thesis is structured as follows: after a brief introduction about the goals of the work and the problem field, which called for this experimental research, the required background knowledge is explained, starting with the structure of collagenous tissues. Afterwards, the mechanical properties of collagenous tissues, and previous achievements in observing their behavior are introduced and discussed.

In the following methods part, the measurement principle and measurement modes of Atomic Force Microscopy (AFM), and the development of the experimental methodology are introduced. The process of sample preparation, imaging, and the measurement of material properties by nanoindentation is described, followed by an explanation of the calculations and statistical methods applied to yield the expected relations and comparisons from the measurement data.

After the description of the methods, the outcomes from the experiments and calculations are presented. Statistical values, plots, and images are introduced in the results section, and significant measurement outcomes are presented. In the following part, the results are interpreted and discussed, considering their accuracy and significance, contemplating the role of present study in the field of collagen mechanics. Finally, conclusions are drawn and suggestions are made for the further extension of this study.

2. Background

2.1. Human tissue

The human body is built from various tissues, which demonstrate a high variety in their constitution and function. One of the most important features of the body and its organs is having a well-defined structural organization, shaped by their comprising tissues. Skeletal tissues constitute features of the body which provide stability and support, enabling locomotion while protecting inner organs. Without skeletal tissues, the human body would only be an amorphous mass.

2.1.1. Skeletal tissue

2.1.1.1. Tendons and ligaments

The tissue of tendons and ligaments can be noticed by a characteristic shiny white extracellular matrix, resulting from the content of collagen fibers (Figure 1). These are arranged in a dense connective tissue structure, shaping regular bundles, containing fibroblast (collagen secreting cell) inclusions. The scarcity of blood supply and active cells limit the tendon to redevelop properly, so that the healing process after a damage is elongated compared to other tissues [6].

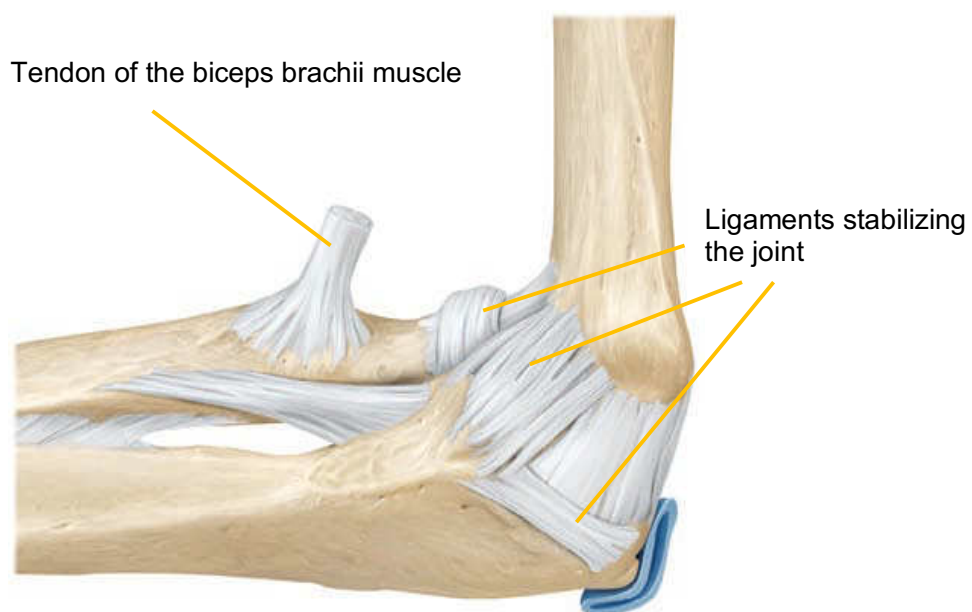


Figure 1: Medial view of an elbow joint [6]

Tendons and ligaments play a key structural role in the human body along with bones. Ligaments provide strong attachments between bones, and provide mechanical stability by smoothly constraining and guiding joint motion, while they bear tensile and torsional loads. Tendons connect muscles to bones and transfer dynamic forces, whereby they must have less ductility and higher stiffness compared to ligaments, to directly and effectively transfer loads. Due to their hierarchical rope-like architecture, tendons and ligaments can withstand tensile loads up to 30 MPa, with an average stiffness of 1.2 GPa [7]. This value is lower in comparison to bone tissue (20 GPa) [8], which is comprised of the much stiffer mineralized collagen fibril. The tensile behavior of bone and tendons will be described in more detail in Chapter 2.2.4.

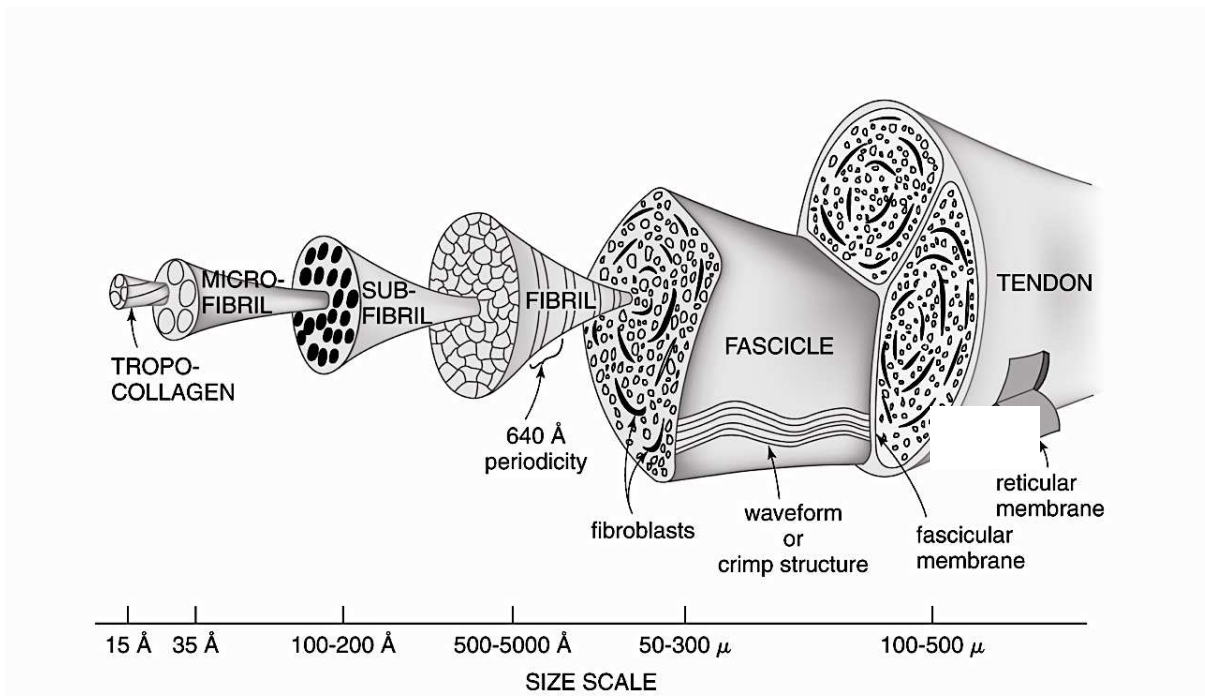


Figure 2: The hierarchical structure of a tendon [9]

The hierarchical architecture of a tendon can be described as follows (Figure 2): a tendon consists of several thick fascicles of 50 – 300 μm diameter, separated by their fascicular membrane. The fascicles basically accommodate bundles of collagen fibrils, the fibers, along with important supplemental blood vessels, nerves and the fibroblast cells. The basic building block of tendons and ligaments is the type I collagen fibril (Chapter 2.2.), incorporating type III molecules, with a diameter spanning on the 100 nm scale [9]. Fibrils are further comprised of tropocollagen strands (see 2.2.1), which can be organized in microfibrils or subfibrils. Tendons of vertebrate origin further act as the most important source of native collagen fibrils.

2.1.1.2. Bone tissue

During embryonic development, bone tissue evolves by the replacement and calcification of cartilage tissue, or by direct mineralization of the osteoid matrix. In the comprising ECM of bone, the collagen fibril (type I) occurs in a modified state, in which calcium-phosphate (CaP) mineral platelets are embedded in the fibrils of the ECM. The calcified collagenous connective tissue is then arranged hierarchically. This can be described on seven levels as on Figure 4 [10].

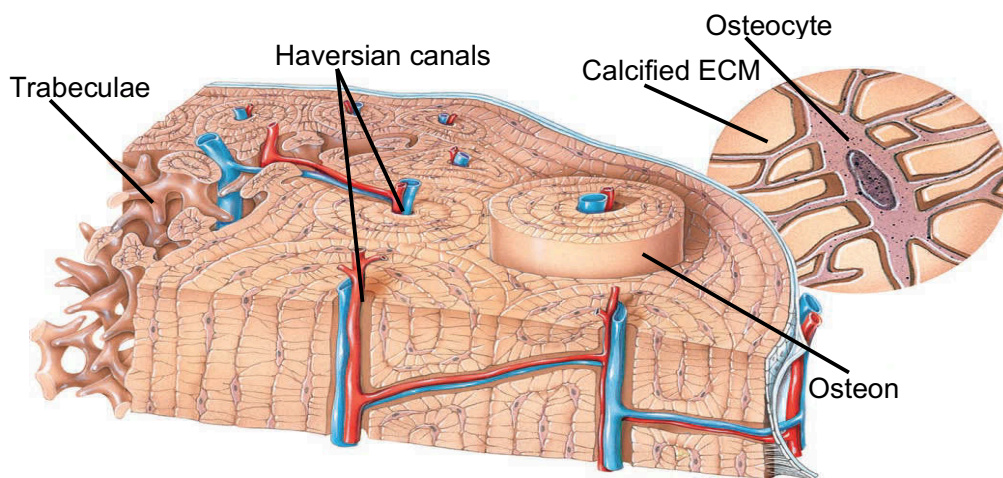


Figure 3: Bone structure on level 6, and illustration of an osteocyte embedded in calcified ECM [6]

A whole bone (level 7), in its bulk shape consists of two remarkably different arrangements of calcified tissue on the macroscopic level 6 (Figure 3): compact and trabecular bone. Compact bone consists of osteons, which consist of concentric lamellar tubes. The lamellae are built of calcified collagen fibers. Tight gaps of lacunae are located between lamellae. Other elements of the calcified ECM such as osteocytes are tightly embedded in this dense structure. The Haversian canals, the central axial void of osteons, include the network of blood vessels which is spread across the compact bone structure and supplies the tissue [6].

In contrast, trabecular (spongy) bone is built of small struts and plates called trabeculae. The trabeculae build an open porous network, which allows for the accommodation of the bone marrow. Generally, spongy bone fills the inside cavity of small sized bones and the epiphysis and metaphysis of long bones, building a mesh which follows load trajectories, while the compact bone provides the essential structural strength, comprising the shell of bones, creating their shape. Thus, bones are structured as a hollow, creating an optimal mass/strength ratio [6].

Compact bone has a specific basic building block as their main constituent on the next lower level (level 5): the osteon is a circular columnar structure of concentric lamellae circumventing a central tunnel. The outer diameter of one osteon lies between 200 – 250 μm [11] in adult human bones. The osteon evolves due to the remodeling process of the bone tissue which is uncommon for any other calcified tissue. During remodeling, the tissue is reabsorbed by osteoclast cells at locations with decreased load. Then, osteoblasts fill up the cavities again, secreting calcified tissue onto the surface, allocated depending on the specific load distribution. The new tissue is deposited in layers on each other so that in the end the thin Haversian canal remains only, surrounded by the bone tissue [10].

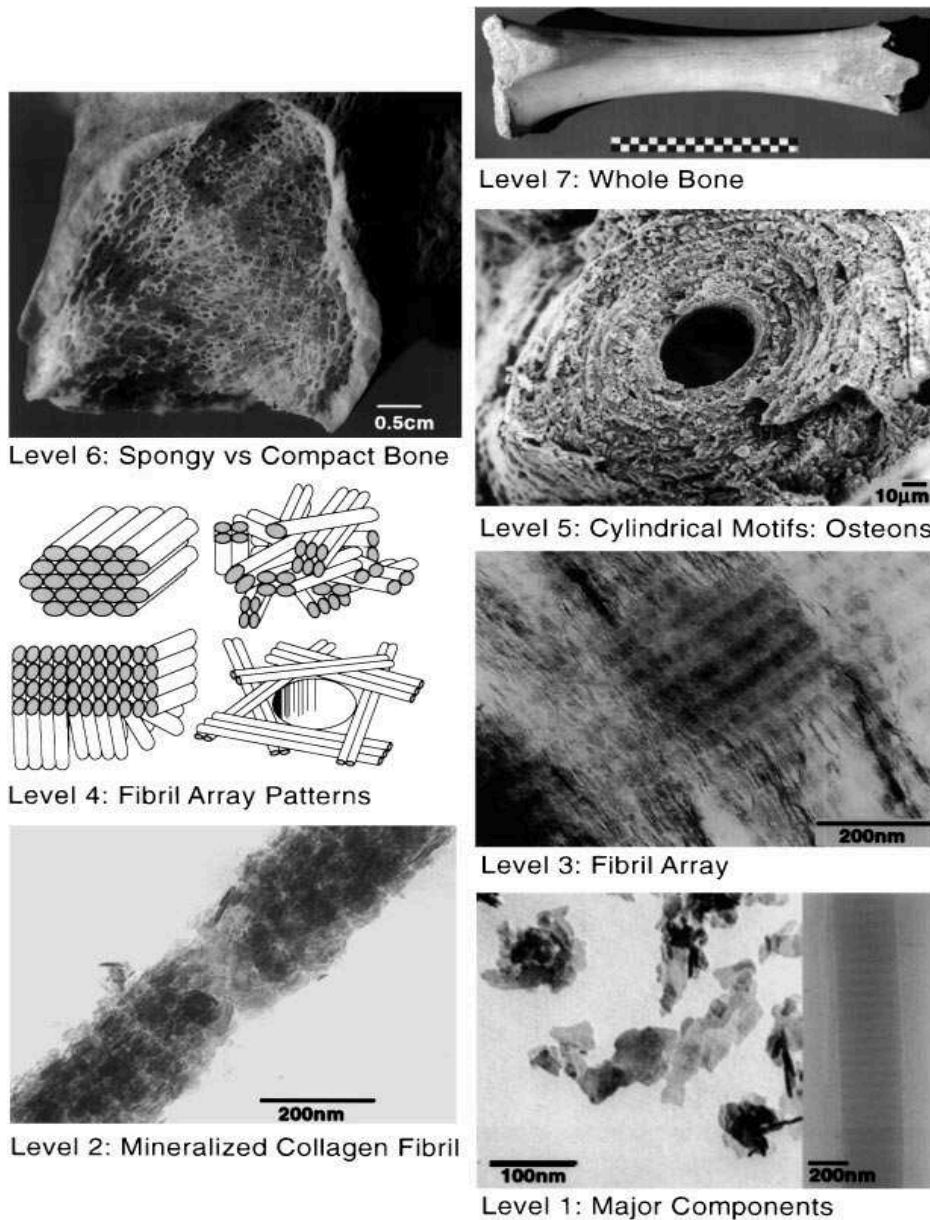


Figure 4: Organization of bone tissue on different hierarchical levels [10]

On the same level (level 5), the trabecular microstructure of spongy bone becomes visible. The struts and plates (a few millimeters long and several hundred micrometers wide) consist of trabecular packets with lengths on the 10 – 100 μm scale and thicknesses on the 1 – 10 μm scale. These consist of lamellae of calcified extracellular tissue, with osteoclasts and osteoblasts shaping the trabecular architecture according to the load to bear [6].

The calcified fibrous ECM, building the lamellae of both of the compact and trabecular microarchitectures, can take up different arrangements (level 4) on the suprafibrillar level (1 μm order of magnitude). The fibril bundles (level 3) can be arranged in random stacks (woven bone), parallel, or in a plywood formation (Figure 5 - c). The plywood arrangement is the common structure of the human lamellar bone, having different layers of fibers, each layer with a certain orientation. The structural strength evolves due to the angular change of the layer orientations, changing gradually from 0° at the first layer to an orthogonal last layer [10].

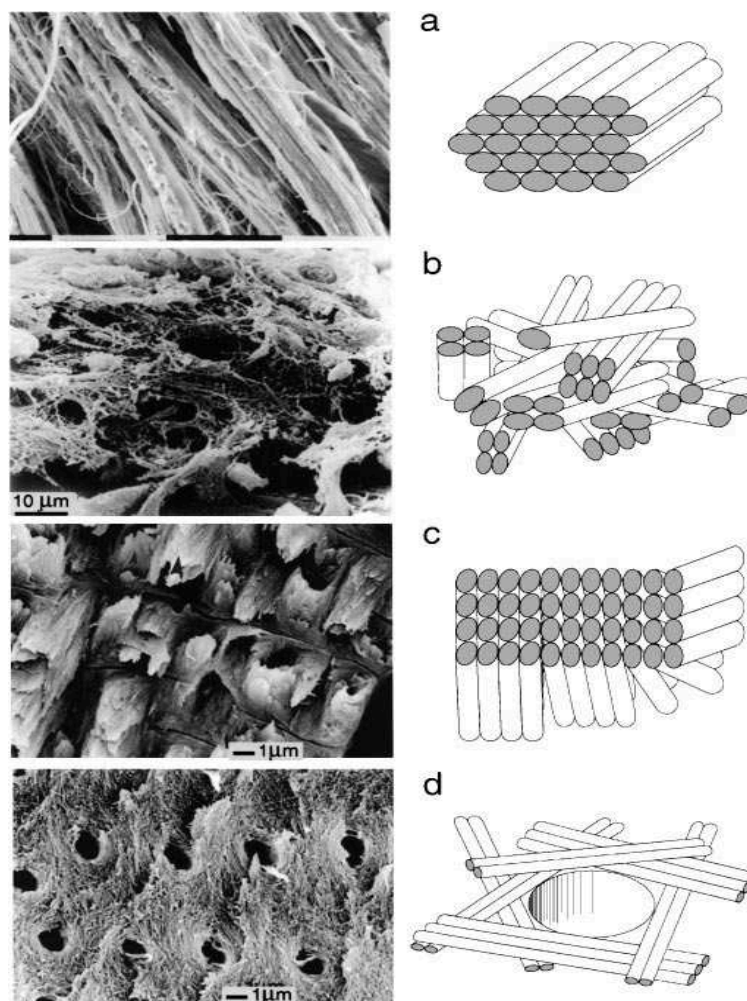


Figure 5: Possible arrangements of fibril bundles on level 4 [10]

The fibril bundles consist of mineralized collagen fibrils (MCFs, Figure 4), additionally surrounded by an extrafibrillar mineral matrix [12]. The MCF is the basic building block of bone, denoted as level 2 by WEINER & WAGNER [10], with the collagen (type I) fibril as the level 1 constituent. It has a length on the μm -, and a thickness on the 100 nm length scale.

Collagen is not the only protein comprising bone tissues: several other proteins play a key functional and structural role in the effective synergy of collagen and CaP minerals. These non-collagenous proteins (NCPs), such as osteopontin, osteocalcin or osteonectin, control and maintain the nanoscale assembly and the mineralization process. They provide <10% of the bone mass [13], [14], and directly impact bone fracture mechanics.

The strength of bones results from the above discussed multi-level architecture, the overall bone matrix volume (BMV), and the level of bone mineralization. BMV is commonly referred to as bone mass, and is sometimes interchangeably used with the bone mineral density (BMD). In fact, they represent different properties. While BMV [%] reflects the amount of bone tissue mass in a volume element, BMD describes the degree of mineralization in the bone matrix [15]. Additionally, BOIVIN et al. established the bone mineral density distribution (BMDD). BMDD is a statistical distribution, describing the examined area by a histogram of mineral contents, while BMD is given in a ratio of g/cm^2 [16].

Bone remodeling activity is the key determinant of BMD and BMDD, directly impacting bone mechanical properties [16]. During remodeling, the organic matrix is synthesized and deposited first at desired locations. The new matrix begins to mineralize after 5-10 days, in 2 phases.

Due to these special mineralization kinetics, deviations in BMDD can serve as an important indicator for different diseases, whereas the values of healthy individuals demonstrate an insignificant biological variance [16].

The bone tissue, tendons, and ligaments are the most relevant examples of connective tissues in structural biomechanics. Their function and mechanical properties on the micro scale can be best understood by examining their comprising connective tissues.

2.1.2. Connective tissue

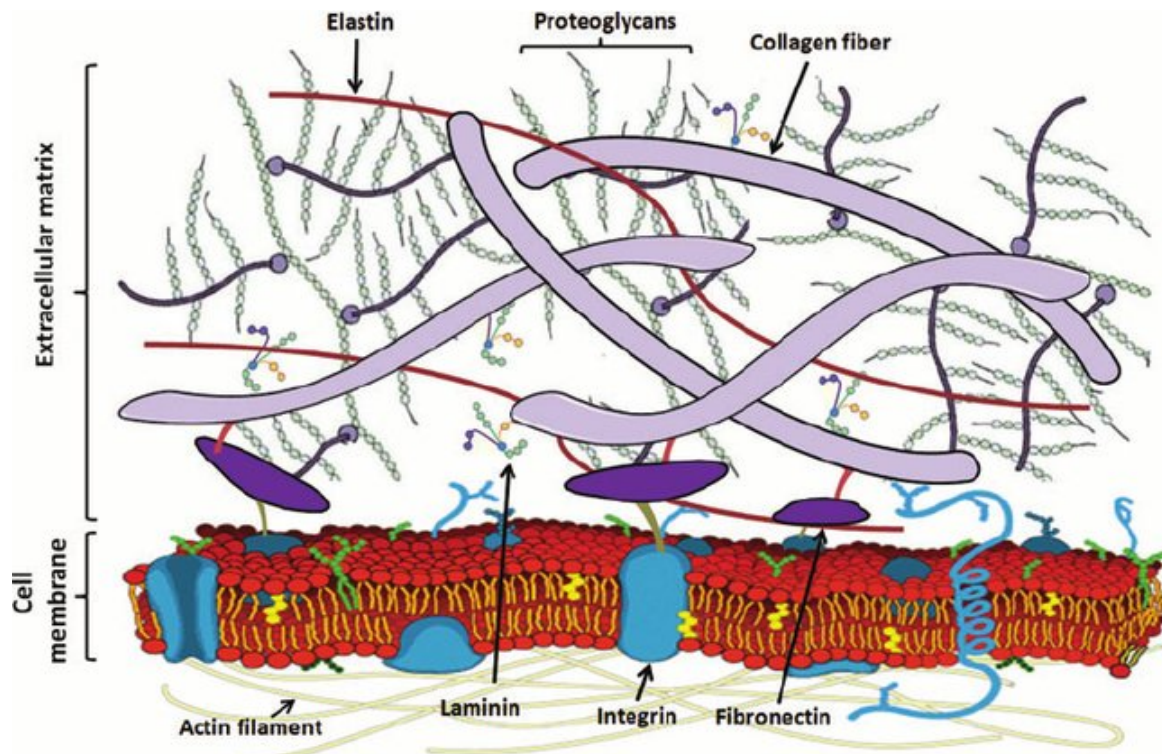


Figure 6: Illustration of major ECM components surrounding a cell membrane [17]

Connective tissues consist of two basic elements: extracellular matrix and cells. The type of cells, but especially the constituents of their extracellular matrix (ECM) characterize the tissue, defining its unique mechanical and biochemical properties, and thus predestinating its specific functions and anatomic location. The cells of the connective tissue are widely spaced, giving enough space for the ECM. The ECM consists of special protein fibers and other basic substances like proteoglycans (PGs), mucopolysaccharides, glycosaminoglycans (GAGs), as illustrated in Figure 6. The type of the comprising extracellular protein fibers is always characteristic for the particular tissue, and as such secreted by the appropriate connective tissue cells. The most abundant protein fibers are collagen, reticular fibers and elastin [6].

Elastic fibers consist of molecules of the protein elastin bound together with the glycoprotein fibrillin to form a fibrous network. The formed elastic connective tissue is capable of large reversible deformations. This kind of elasticity is necessary e.g. in artery walls, in the trachea, or in the tissue of the vocal chords [6].

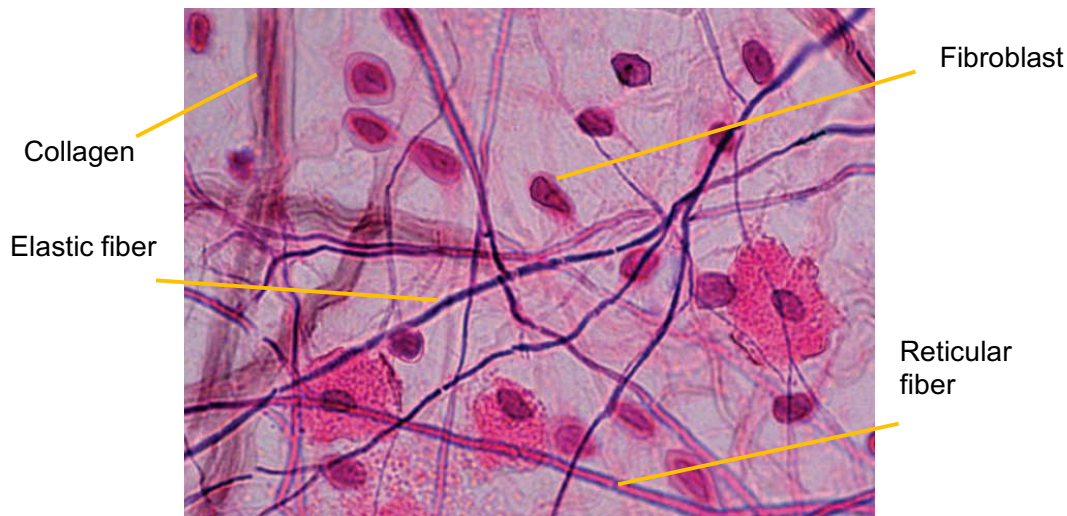


Figure 7: Histological image of human connective tissue [6]

Reticular fibers consist of collagen, however, the collagen molecules are arranged in looser bundles coated by glycoprotein which also fills the space in between. On a higher scale, a loose network is built by these fibers, to provide strength to sheath organs such as alveoli or arterial walls. They are most abundant in the reticular connective tissue, which forms the basement membrane and the stroma, the embedding, capsuling coating tissue of soft organs [6].

Collagens are the most important structural fibers in human tissues, whereby they are also present in non-vertebrates. The variable molecular assembly possibilities of collagens provide a wide range of different collagen types.

2.2. Collagen fibril

Collagen fibrils primarily consist of collagen molecules, often including other inorganic (mineral) or organic compounds. There are 28 types of collagen in mammals, designated by numerals I-XXVIII, each of them having different structure-mechanical capabilities [18].

Only certain types of collagen form fibrils: types I, II, III, V, and XI are the most important fibrillary collagens, which self-assemble during a special biokinetic process. Among these, type I collagen is the major fibrillary collagen: it is present in most tissues acting as the main structural constituent of tendons, ligaments and bones. Different types of tropocollagens can also combine, e.g. by type I merging with a type III network, modifying its properties [19].

2.2.1. Composition of collagen fibrils

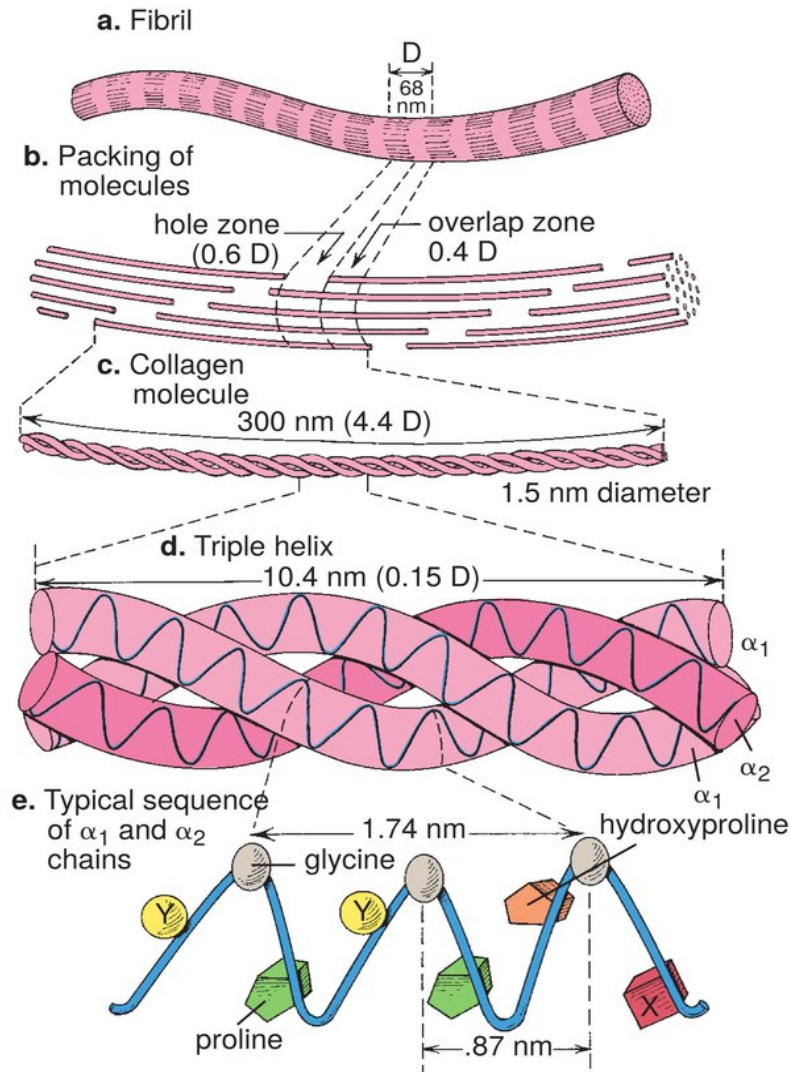


Figure 8: The molecular self-assembly process of a collagen fibril [20]

Collagen molecules consist of three helical polypeptide chains (so called α -chains), which assemble into a triple-helix (trimer). In case of the human ECM, the different α -chains are denoted by the chain type (Arabic numbers) and their comprised collagen type (Roman numerals), e.g. $\alpha_1(\text{I})$. Various combinations of α -chains yield the wide-range of collagen types. If the collagen assembly involves different α -chains, it results in a heterotrimer, while in case the same α -chains comprise the triple-helix, it is denoted as a homotrimer. For instance, type I heterotrimer collagen is built by the combination of two chains of $\alpha_1(\text{I})$ and one chain of $\alpha_2(\text{I})$, type II collagen contains three identical chains of $\alpha_1(\text{II})$, so it is a homotrimer [18].

Studies on collagen have revealed, that both native and reconstituted fibrils demonstrate a considerable change in diameter in fluidic environment in contrast to dry ambient conditions [21]–[25]. This reversible phenomenon is accounted for the ability of water molecules to incorporate in between the hydrophilic intrafibrillar TC molecules. This increases the intermolecular distance. A diameter increase of around 70% is typically observed in phosphate-buffered-saline (PBS) solution [23], [26].

2.2.2. Collagen fibrillogenesis

Let us proceed with the introduction of the molecular self-assembly process of collagen type I (Figure 8). The process is essentially similar to the assembly of other collagen types. The two $\alpha_1(I)$ -chains, and the $\alpha_2(I)$ chain are peptide-chains with different amino acid sequences, where every third amino acid residue is a glycine, resulting in a characteristic Gly-X-Y pattern. Among all other residues, proline and hydroxyproline are the most frequent. The polypeptide chains are generated in a fibroblast cell and each separately evolve into a secondary structure of left-handed helices. Tertiary, the three helices arrange themselves into a right-handed triple-helix, folding in a zipper-like manner resulting from the pattern of amino acid residues [27].

The triple-helices are synthesized in the endoplasmic reticulum as soluble procollagens with free ends. Thereafter, a specific proteinase cleaves the start- and end-propeptides, so that the rod-like, already non-stretchable tropocollagen (TC) with the characteristic length of 300 nm is yielded, which is then secreted out of the fibroblast cell [28].

The TC molecules further assemble by an entropy-driven process into fibrils, with the help of specific covalent cross-linking [19]. The assembly is characterized by a staggered arrangement of TC molecules (Figure 9), leading to a characteristic array of a 40 nm gap and a 27 nm overlap zones and resulting in the formation of the unique 67 nm D-spacing pattern (Figure 9) as described by the Hodge-Petruska model [29]. Regarding the fibril's cross section, a cylindrical structure of a radial packing density of $0.5 \frac{1}{nm^2}$ is established, where each TC is surrounded by six neighbors [30].

Type I fibrils further arrange into fibers and fascicles to comprise tendons and ligaments (2.1.1.1) or act as the basic building block of bones in their mineralized form (2.1.1.2).

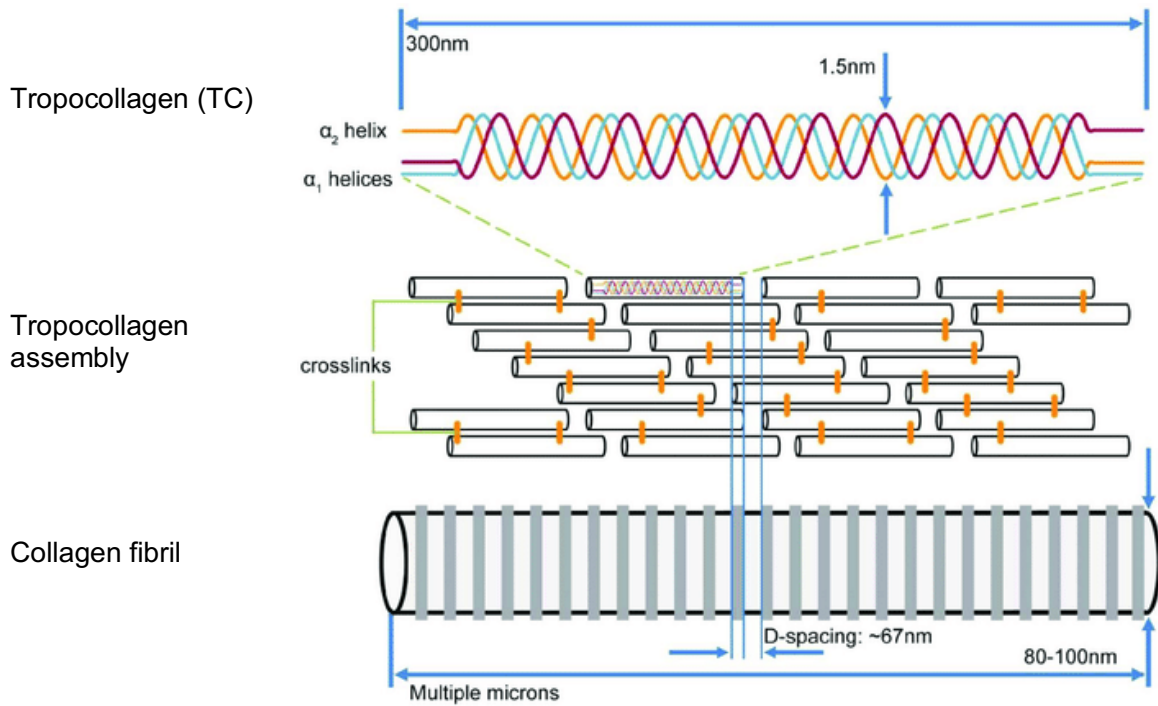


Figure 9: The evolution of the D-spacing pattern [27]

The *in vitro* growth mechanism of reconstituted fibrils eventually requires the presence of additional agents and enzymes, which would fine-tune the generation process towards a result which is comparable to an average native fibril [31]. Often, *in vitro* developed fibrils develop an irregular, structure, appearing less robust than that of an average native fibril (Figure 10).

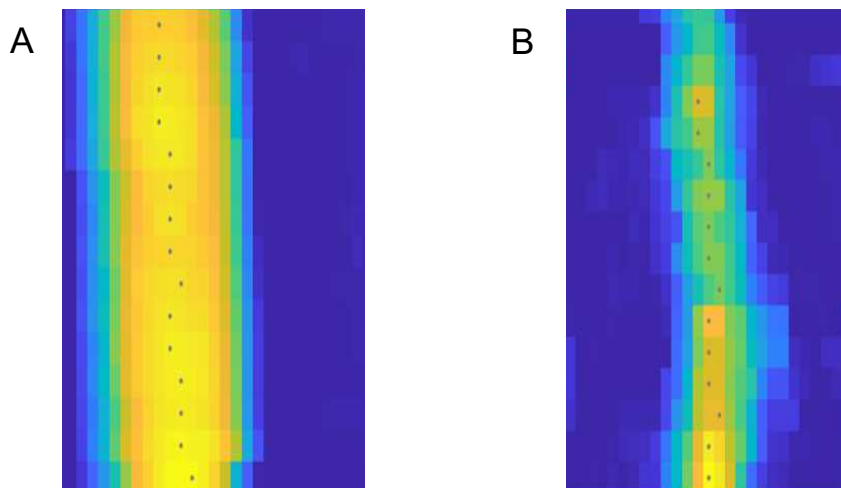


Figure 10: Qualitative height images of native (A) & reconstituted (B) fibril segments of $2\mu\text{m}$ length

2.2.3. Mineralized collagen fibrils

The property which makes collagen fibrils a unique substance, is their morphological and mechanical versatility due to the combinational ability with other substances such as Hydroxyapatite (HA) minerals, GAGs, PGs, or NCPs.

Calcification occurs primarily in the gap zone of the fibril. The mineralizing substance precipitates from cells, near the prospective growth zone in the form of amorphous calcium phosphate (ACP) globules, with sizes ranging from 1.3 – 1.6 nm [32], enabling the substance to penetrate the gaps [16]. Thereafter, the chemical phase transformation into the thermodynamically more stable solid phase occurs highly organized, via homogeneous nucleation without organic substances involved [33]. The crystalline platelets can grow to a size of 1– 7 nm in thickness, 15– 200 nm in length, and 10– 80 nm in width depending on the gap size and the chemical potential of the environment.

The formation of the Hydroxyapatite ($\text{Ca}_{10}(\text{PO}_4)_6(\text{OH})_2$) crystals is initiated in spatially distinct nucleation spots in the hole zone region, with the long axes of the crystals aligned parallel to the long axis of the fibril (Figure 11). The primary growth of the crystals occurs longitudinally, followed by a thickening in width [3]. The increase in size is part of the secondary nucleation process (2.1.1.2) in a long period [34]. The evolving crystals within the fibrils also extend into the pores of the overlap zone so that the available space within the fibrils is filled [33], [35].



Figure 11: Schematic illustration of a mineralized fibril, crystallized between staggered TC struts [36]

Basically, the higher the protein content in the tissue, the less degree of calcification can be established. For instance, cancellous bone has the highest density of collagen fibrils, and the lowest degree of mineralization resulted by that [37]. Based on the theoretical modelling study of DEPALLE et al., fibril stiffness and toughness increase with mineralization, and reach a maximum at 30% of intrafibrillar mineral concentration. Additionally, while the fibril keeps its initial length during crystallization, an increased mineral content induces internal stresses [38].

2.2.3.1. Controlling collagen mineralization

The terminal ends of the collagen molecules in the gap region contain clusters of both positively and negatively charged amino acids, which act as attractive nucleation sites for HA. That is, collagen in fact controls the infiltration and the nucleation process of HA. The influence of the collagen itself is larger than that of the space availability, that is why crystals also nucleate in the overlap regions [34]. Apart from the side-chains of collagen molecules, the conditions for the mineralization process are defined by NCPs of the ECM through inhibition and promotion.

The serum protein fetuin is the most important agent which controls mineral formation. Its primary effect lies in the inhibition of pathological precipitation of calcium phosphate in the serum, thus enabling the mineral substance to stay in its small-sized amorphous phase, until reaching the target collagen fibrils [37]. In general, larger molecules, also including fetuin itself, cannot penetrate the fibril. Thus, fetuin carries out its effect everywhere exterior to the fibril, while in the gap zones the formation of mineral is not inhibited [34].

2.2.4. Mechanical properties of collagen fibrils

ECM on the whole can be observed as a continuum, if deformations and stresses are examined on the tissue level. This approach is enabled by the large difference between the length scale of the tissue level and the smallest comprising element (fibril). However, to better understand the tissue behavior and in order to analyze events rooting at a lower scale constituent, the structure-mechanical assessment is favorable, examining underlying components of the tissue [28].

2.2.4.1. Native collagen fibril mechanics

Collagen fibrils and the comprising TC are considered as transversely isotropic structures [39], primarily bearing axial load, so their stress-strain relationship is commonly assessed by tensile testing. Experimental studies defined the axial tensile modulus of the TC molecule in the range of 3 – 10 *GPa* [28], [40], while molecular dynamics simulations yielded results within the range of 3– 16 *GPa* [41]. TC gives in to axial loads first by unfolding of the triple helix, then by stretching and finally unfolding of the α -helices, which results in a high stiffness. TC molecules are connected with covalent cross links to comprise fibrils. These crosslinks account for the initial shear mode in case of fibril stretching during tensile tests, followed by the uncoiling of TC molecules resulting in a stiffness of 2 – 7 *GPa* [22], [39], [40].

Furthermore, on the tendon level, an initial non-linear behavior is observed: at first, the fibril-fibril bonds bear load, causing a lower modulus in a stress-strain relationship [42]. Meanwhile, the bone tissue comprised by MCF is more stiff and behaves more linearly (Figure 12).

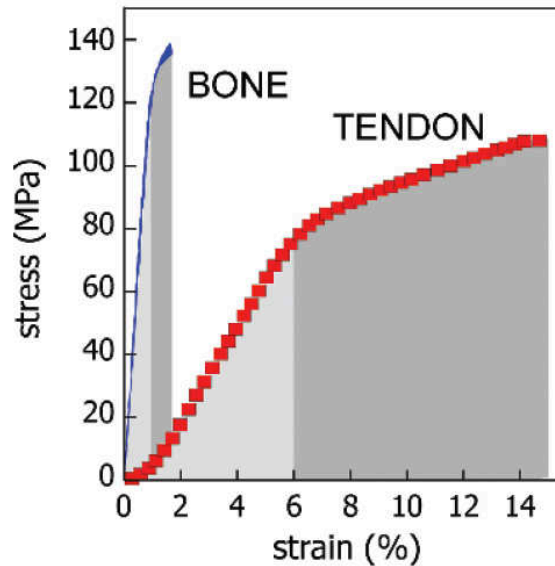


Figure 12: Illustration of the tensile stress-strain relationship of tendon and bone. Areas under the curves correspond to the energy stored (lighter grey) or dissipated (darker grey) at deformation [8].

Recent tensile tests along with theoretical models suggest, that the hydrated native fibril tensile modulus lies around 1 GPa [25], [26], [43], [44]. Meanwhile, indentation moduli lie at the 1 MPa order of magnitude [21], [24], [45]. Generally, it has been observed, that the material properties at each scale are directly linked to the ones of its lower scale constituents [43].

2.2.4.2. Determinants of collagen fibril mechanics

The difference between the dry ambient and wet hydrated state of the fibril does not only affect its morphology (swelling), but also its mechanical properties. The hydrated, wet state mimics the physiological condition better, and is thus of special interest. The stiffness is by 40% lower in wet state compared to the ambient dry state [45], and even by several orders of magnitude compared to a chemically dehydrated state [22], [23]. It was also found that osmotic pressure reversibly affects mechanical properties. While the effective contribution of the embedding matrix is negligible concerning stiffness enhancement, it plays an important role in establishing viscoelastic tendon mechanics [43].

In viscoelastic experimental studies on collagen fibrils, a pattern of increasing relaxation times is observed upon increasing tendon hierarchical levels, implying an enhanced viscous behavior resulting from the involvement of various additional compounds in the fibrous structure [41]. Additionally, long-term temperature exposure and the height of temperature affects the stiffness of fibrils negatively [24], [46].

2.2.4.3. Mineralized collagen fibril mechanics

Studies have proven that the mineralized state of a collagen fibril corresponds to an increased hardness and stiffness in contrast to the unmineralized state [1], [16]. The microhardness of a pure collagen matrix is significantly lower than that of the calcified matrix [2], and the elastic stiffness also correlates with BMD [1], [16].

Hydration has a similar impact on the mineralized fibril mechanics as on non-mineralized collagen fibrils, and variations in the mineral content also affect the water distribution inside the fibril, thus directly impacting mechanical properties [47]. In a physiological-like hydrated state, an indentation modulus of 1.5 *GPa* on dentin MCF was obtained by BALOOCH et al. [48].

2.3. Previous studies on collagen mechanics

One of the approaches to study the behavior of collagenous tissues is to create molecular and micromechanical computational models with specific modifications, evading the complexity of experimental methods. Computational models of the MCF revealed a solid relationship of mineral content and modulus [49], [38]. WANG and URAL additionally established the close relation between the global modulus of bone tissue and the modulus of the building MCFs [5]. While it is useful to have an impression based on theoretical models, the experimental values revealed in this study may provide more realistic data.

Along with computational models, experimental tests on animal and human collagenous tissues already predicted their general mechanical characteristics on the tendon and fiber level [40], and the relation of their tensile stiffness to their mineral content [16], [35], [50]. These high-level studies provide good understanding for tissue behavior, but still lack fibril-level data.

Lately, micromechanical methods such as micro-electro-mechanical systems (MEMS) and atomic force microscopy (AFM) have been employed, to directly measure native collagen fibrils. An extensive review of GOH et al. from year 2014, summarizing the results on native collagen fibrils, serves as a comparable basis regarding their morphology and mechanics [28].

AFM was first used in relation to collagen fibrils for imaging purposes, which continued to be a primary aspect of fibril observations, revealing subfibrillar structural features [48], [51]–[54]. Since OLIVER and PHARR [55] set the basics for the data analysis of the indentation of soft materials, various types of biological tissue samples have been tested for their mechanical properties by AFM nanoindentation [56], [57]. Only few of these studies measured vertebrate collagen fibrils in the wet state, and none of them assessed the single mineralized fibril. However, BALOOCH et al. registered a decrease of the indentation modulus of dentin fibrils through stepwise demineralization [48], serving as a comparable example, but lacking data about the direct effect of mineralization on an unmineralized native fibril.

Other studies mainly focused on measuring the outcomes of certain environmental influences on the fibril, including the effect of various thermal treatments [46], or different hydration states [21], [58]. It has been shown, that the Ca^{2+} concentration in the fibril environment increases its mechanical properties [59], which justifies current study on the effect of *in vitro* mineralization.

Specific studies have further improved AFM nanoindentation methods [26], [39], [60]–[62]. Especially, the study of ANDRIOTIS et al. [39] serves as a framework for this thesis, who developed an experimental methodology and elaborated a data evaluation process.

3. Methods

The research work was conducted on three different fields: sample preparation & *in vitro* mineralization, nanomechanics and data analysis. The workflow is introduced in Figure 13. Essentially, collagen fibril samples of different origins were sourced and subsequently modified by mineralization in multiple steps. The samples were examined in each step of mineralization by AFM nanoindentation, and the measurement data was analyzed by statistical methods.

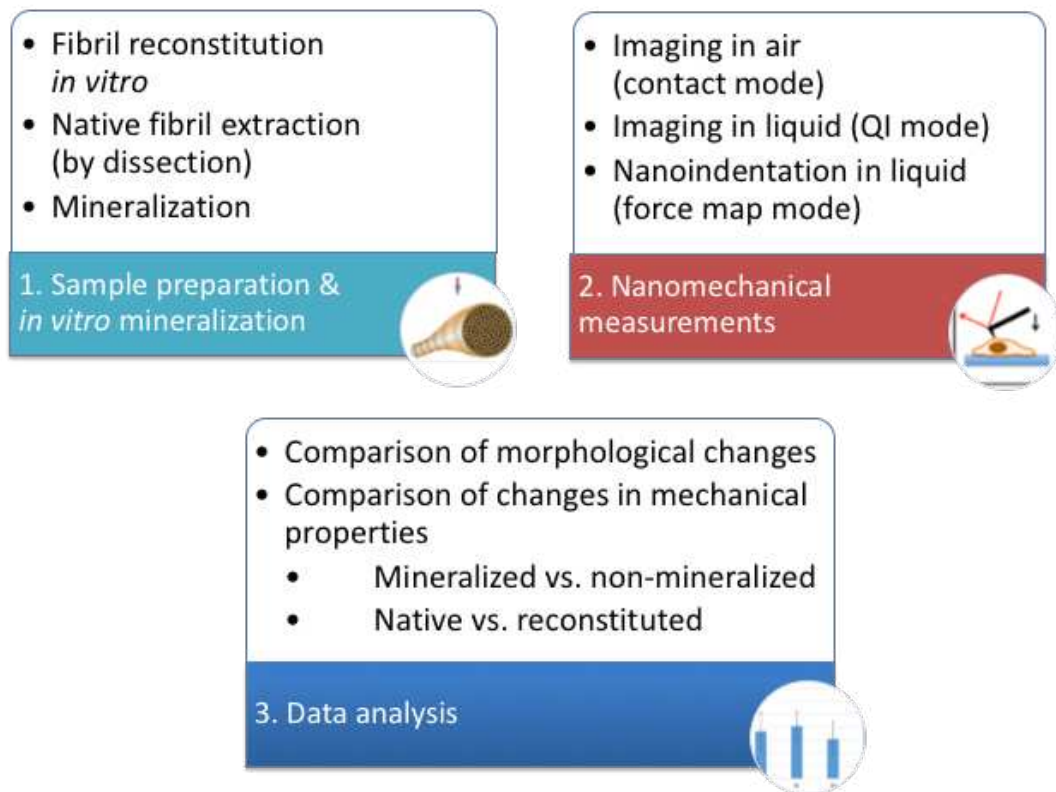


Figure 13: Definition and contents of the different fields of working methods

3.1. Sample preparation

3.1.1. Native fibril extraction

A tendon segment from the tail of a six-month-old male mouse was harvested with scalpel. The cadaveric tail had been stored at $-80\text{ }^{\circ}\text{C}$ before it was exposed to ambient air. Poly-l-lysine (PLL) coated glass slides (Thermo Scientific USA, Gerhard Menzel B.V.&Co.KG Braunschweig, Germany) of size $75 \times 25\text{ mm}$ were used as substrates providing sufficient adhesion.

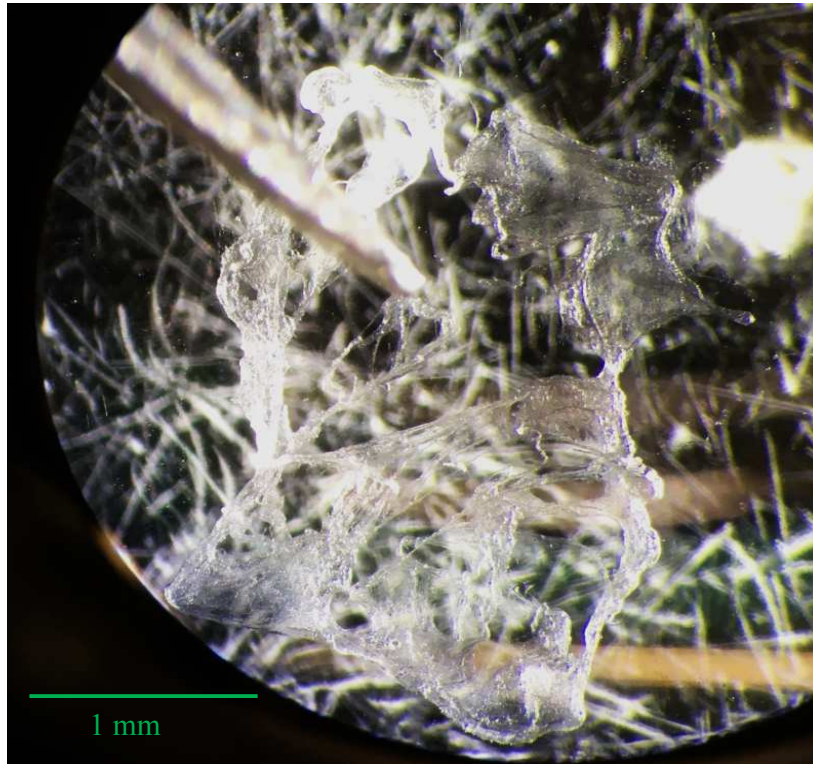


Figure 14: A fascicle smeared over a sample slide by a tweezer, exposing fibrils (5X magnification)

A bundle of collagen fibers was dissected from the mouse tail tendon, and a single fiber was deposited onto the PLL slide. It was essential to keep the sample under the right level of hydration to carry out smearing. This was achieved by the appropriate size of a distilled water droplet on the fiber bundle. The fiber was smeared over the substrate using a tweezer to reveal fascicles and to expose the collagen fibrils (Figure 14). The sample was then left drying in ambient air.

10 sample slides originating from the same mouse tail tendon, containing multiple exposed collagen fibrils, were prepared for experiments by this process. The most promising samples, having a large amount of distinct individual fibrils, were then used for subsequent experiments.

3.1.2. Mineralization

Mineralization steps were established to modify the sampled fibrils by producing intrafibrillar crystals. A buffer solution, containing fetuin, was prepared by a protocol (Annex A) developed by BURNS [63], based on the experiments of NUDELMAN et al. [37] and PRICE et al. [64], who both reported successful in vitro mineralization of individual collagen fibrils.

In subsequent mineralization steps (denoted as “Min1”, “Min2“ & “Min3” steps), a sample slide was immersed entirely in the mineralizing solution in a polypropylene slide tube mailer (Deltalab S.L., Rubi Barcelona, Spain), and placed in an incubator for 20 hours at 37 °C. Before immersing the glass slide, the tube with the mineralizing solution was already heated to 37 °C to reduce immersion time by the time needed for warming up.

3.1.3. Control mineralization

Preceding the actual mineralization steps, the fibril samples were subjected to a control mineralization step (see Figure 37). This step was carried out with the same workflow and parameters as “conventional” mineralization, however, fetuin was not included in the mineralization buffer solution. Thus, in this step, denoted as “Min0”, the measured sample slide was immersed in the control mineralization solution in a polypropylene slide tube mailer (Deltalab S.L., Rubi Barcelona, Spain), and placed in an incubator for 20 hours at 37 °C.

In this step, intrafibrillar mineralization was not meant to take place, and thereby solely the effects of the tempered ionic fluidic environment could be assessed for a comparison (6.2.1).

3.1.4. Phosphate-buffered-saline solution

200 mL of PBS solution of pH 7.4 was prepared, by dissolving a phosphate-buffered-saline tablet (Sigma Aldrich Corp., St. Louis, Missouri, USA) in 200 mL of distilled water. This buffer served as a fluidic environment in all indentation steps of the following experiments.

3.2. The concept of AFM experiments on collagen fibrils

Soft tissues have been tested before on the macroscopic level (e.g. [65]–[67]), traditionally with uniaxial or biaxial tensile tests. Flat, network-like structures are preferably assessed by a biaxial strain or stress state, while structures with a unidirectional fibrous architecture are better tested with a uniaxial tensile test. Additionally, different constituents of bone tissue have been mostly tested for their (micro)hardness, and for their tensile stiffness (e.g. [68], [69]).

Atomic force microscopy (AFM) has been primarily utilized for imaging purposes, and lately the mechanical testing of biological materials has become popular, applying AFM.

One particular protocol of the AFM allows for axial tensile testing, by gluing one end of the fibril to the cantilever and the other to a substrate, thus being able to control and monitor axial tension and displacement (Figure 15) [23], [26].

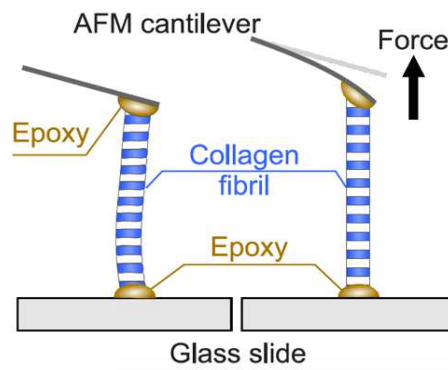


Figure 15: Experimental setup of an AFM-tensile test on a collagen fibril [23]

The most employed experimental method for nanomechanical experiments on collagen fibrils employing AFM is nanoindentation [39], [46], [48], [58]. It generally takes place in a fluidic environment, mostly in PBS or distilled water (DW), and yields force-displacement data by indenting the surface of the fibril [48].

3.2.1. The principles of AFM nanoindentation

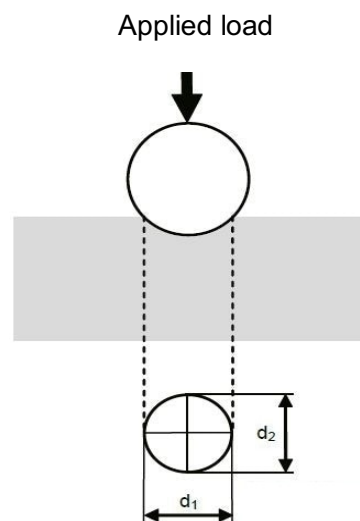


Figure 16: Brinell's indentation test scheme

BRINELL established the first indentation tests for measuring hardness and plasticity of different, mostly hard materials. In case of his traditional indentation setup, a probe of known geometry is driven to approach and puncture the surface of the material applying a given force or displacement, then retracted. The residual trace of the indenter head in the material is assessed visually in its geometrical shape (Figure 16), which is then associated with a hardness number. Today's instrumented indentation (with digital control equipment and precision measurement instruments) enables monitoring and controlling load and displacement on the nanoscale [70].

Nanoindentation is based on the same principle. It employs a measurement probe with dimensions on the nano-scale, so that it usually a good alternative to conventional tensile experiments, capable of providing high load resolution and fine depth-sensing capabilities.

A frequently used instrument for the nanoindentation of collagen fibrils and cells is the atomic force microscope. The principle of the AFM is based on a soft, thin cantilever, with a tip on its end. Its conventional use includes the examination of topography and surface interactions. The vertical displacement of the cantilever holder can be precisely controlled by piezo crystals. This makes the AFM suitable for creating high-resolution force-displacement data, by exerting an approach and retract motion of its cantilever tip and assessing deformations. The X-Y position of the sample plate bedding can be controlled precisely by stepper motors, or can be manually adjusted as in a classic microscopic setting.

3.2.1.1. Optical lever

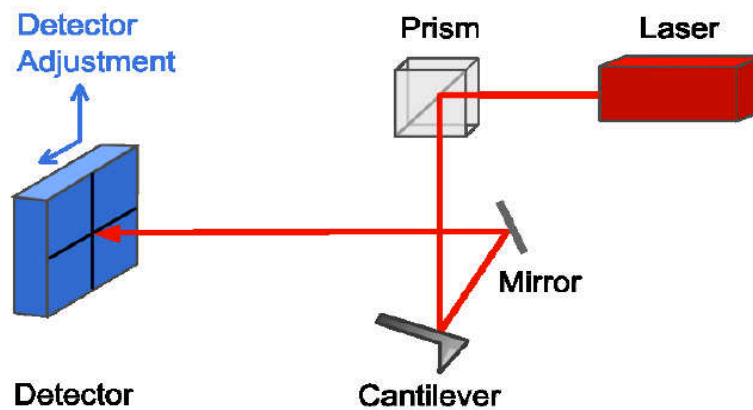


Figure 17: Schematic illustration of the laser beam path in the utilized AFM equipment [71]

The basis of the AFM principle is the optical lever mechanism. The light beam from a superluminescent diode source is directed onto the cantilever. The cantilever has a reflective coating which reflects the light through a lens system onto a segmented photodetector (Figure 17).

Thus, the slightest movement of the cantilever tip can be sensed by the bending and displacement of the cantilever, and consequently by the displacement of the reflected beam on the detector. After appropriate calibration of the sensitivity and the spring constant of the cantilever, various quantities such as the load on the cantilever or the depth $\delta = dh$ can be determined (Figure 18). Fundamental inputs are the change of the Z-displacement, z , the change of the deflection, d (determined as in 3.2.2.2), as illustrated on Figure 18, and the cantilever spring constant k (determined as in 3.3.5.2).

Thus, the depth is determined as follows:
$$\delta = (z - z_0) - (d - d_0) \quad (1)$$

$$dh = dz - dd \quad (2)$$

And the load is given by:
$$F = k \cdot d \quad (3)$$

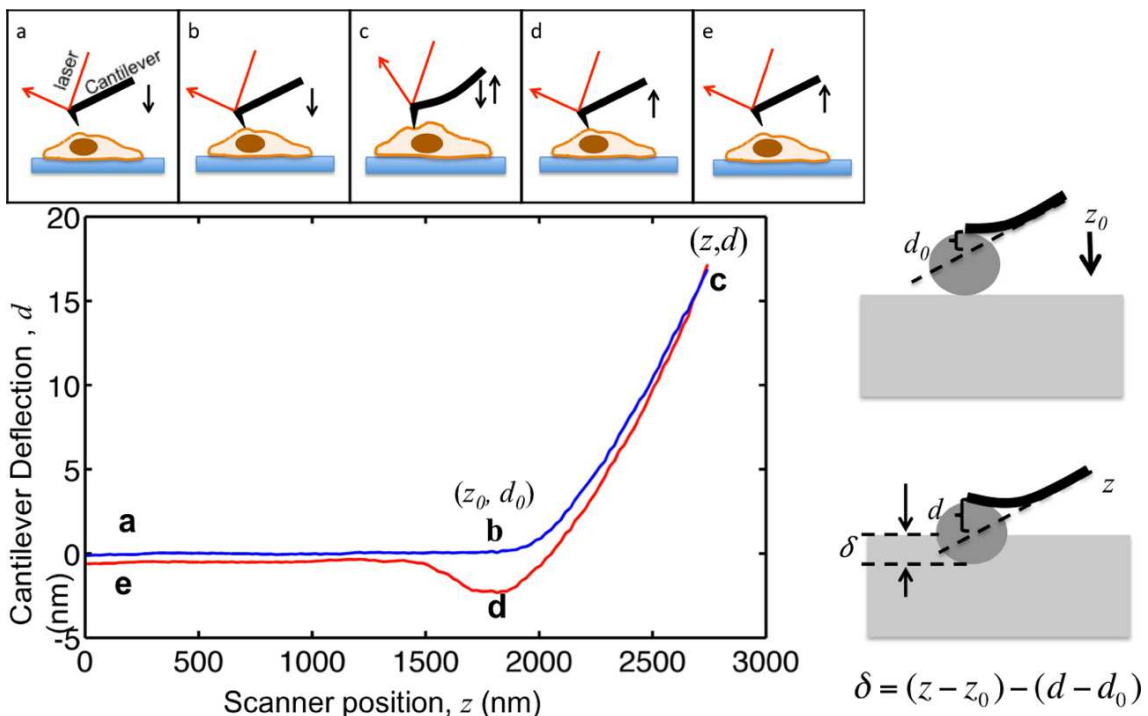


Figure 18: Illustration of AFM indentation, with piezo position z , depth δ , and deflection d [72]

a-b approach, *b-c* load, *c-d* unload, *d-e* retract phase

3.2.1.2. Indentation process

With AFM nanoindentation, Z-movements in nm and loads in pN resolution are possible, making it applicable to measure thin films and tissue samples. An AFM nanoindenter can be utilized to create a force-displacement plot at a fixed X-Y position (Figure 19). The controlled Z-displacement of the cantilever head makes the tip approach the surface and indent the sample up to a pre-set force. During this procedure, the contact force F is measured, which emerges by the resistance of the sample material to indentation (Equation 3).

The resulting force-displacement plot from an indentation is pictured in Figure 19. After being undeformed in the approach phase, the cantilever bends and takes on load as it is pushed onto the surface of the sample. After a defined terminal force is reached, the process turns into the retract phase where the load on the cantilever decreases and the cantilever gradually unbends.

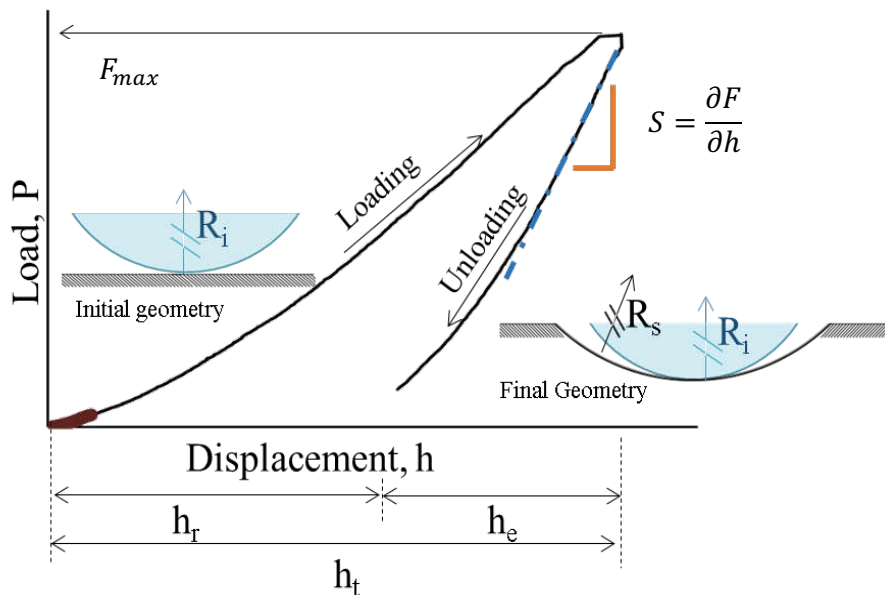


Figure 19: Qualitative force-displacement plot, with the slope (contact stiffness) S of the unloading curve [70]

Once a force-displacement plot is constructed, the primary quantity to be measured on the plot is the contact stiffness S , extracted as the linear slope fitted to the unloading curve.

$$S = \frac{\partial F}{\partial h} \quad (4)$$

There is a consensus since the study of PHARR and BOLSHAKOV, that the first 10-15% of the unloading curve has to be assessed for elastic measurements for the best accuracy [73]. With help of the contact stiffness S , the indentation modulus can be expressed [55]:

$$E_0 = (1 - \nu^2) \frac{S}{2\beta} \sqrt{\frac{\pi}{A}} \quad (5)$$

Where the experimental correction factor β varies with indenter shape, and the contact surface A is defined as the projected area of the indenter surface currently in contact with the sample surface. This surface area can be simply measured in case of indenter shapes of known geometry, such as a cylindrical or spherical indenter. However, in case of pyramidal probes with tip diameters on the nanoscale, the area is often experimentally measured, e.g. by using a TGT1 grating surface (see chapter 3.3.7).

3.2.2. AFM nanoindentation in practice

3.2.2.1. Essential instrument settings

The first fundamental adjustment on the AFM is the choice of the feedback mode, on the basis of which the Z -position is controlled. For the purpose of this study, the contact mode is practicable to use, where the Z -position is controlled in a closed feedback loop by the detected bending of the cantilever tip. Thus, when the cantilever approaches a surface vertically and touches it, the initial bending of the cantilever and the resulting movement of the deflected laser on the segmented photodetector diode provides a voltage signal which triggers the Z -actuator to stop (Figure 18, b). A setpoint value for the voltage signal change of the deflection is set which acts as a threshold for signaling that the cantilever tip lies on a surface.

For the choice of the cantilever for soft biological samples, the general approach prescribes that the spring constant of the cantilever shall be at the same magnitude as the expected contact stiffness of the sample. BALDWIN et al. [24] and GRANT et al. [21], [45] measured moduli of native collagen fibrils in the range of 1 – 10 MPa by nanoindentation.

Rewriting Equation 5 yields the expression for the preliminary choice of the appropriate cantilever, as reported by Kain et al. [60].

$$\frac{2\beta}{(1-\nu^2)} \sqrt{\frac{A}{\pi}} E_0 = S \quad (6)$$

Apart from the cantilever stiffness, the indentation velocity and the terminal force essentially influence the indentation procedure as well. The terminal force defines the level of the sensed force on the cantilever, which is induced in a response to indenting and deforming the material. The terminal force acts as a trigger for the end of the load phase of the indentation, and is thus an important determinant for the resulting indentation depth (Figure 18, c). The force-trigger is often preferred in contrast to the direct control of the depth, as the measurement of the contact point and the resulting depth is often very inaccurate due to adhesion and capillary effects.

3.2.2.2. Calibration of the optical lever sensitivity (OLS)

The correct measurement sensitivity is a crucial factor to the final accuracy of the experiments. During a measurement, the raw voltage (V) signal of the detector pane has to be converted to cantilever deflection $d = D$ [nm] values, to be able to determine the force on the cantilever using the cantilever stiffness (Equation 3). Hence, the deflection per voltage ratio (D/V) is required as the sensitivity value of the cantilever.

The ratio of the detected voltage and deflection, ($V/D = OLS$) can be determined experimentally by multiple indentations on a hard surface (see 3.3.5). Thereby it is assumed that in case of such a Z -displacement of the cantilever, where no indentation of any sample material takes place (depth $dh = 0$), the Z -displacement solely represents the deflection of the cantilever (see Equation 2).

Therefore, it is a well employed method to define the $invOLS = D/V$, the translation of the registered voltage signal (dV) to the observed deflection (dD) of the cantilever, by multiple indentation measurements on a hard surface [61], [74]. The raw $V - D$ slopes of these indentations can be fitted linearly to capture an empirical mean OLS (see Figure 24). Then, the inverse of the OLS, commonly referred to as $invOLS$ [$\frac{nm}{V}$], can be yielded.

3.2.2.3. Tip stiffness and the reference slope

If the measured stiffness M corresponds to a series of 2 stiffnesses, the contact stiffness S and the tip, or reference stiffness, R (as a series of springs), the following relation holds [39]:

$$\frac{1}{M} = \frac{1}{S} + \frac{1}{R} \quad (7)$$

The reference- and contact stiffnesses are measured by their corresponding dD/dZ slopes (based on Equations 2-4), so that the expression for correcting the measured slope by the reference slope is defined:

$$\frac{1}{\text{MeasuredSlope}} = \frac{1}{\text{ContactSlope}} + \frac{1}{\text{ReferenceSlope}} \quad (8)$$

$$\frac{1}{\text{ContactSlope}} = \frac{1}{\text{MeasuredSlope}} - \frac{1}{\text{ReferenceSlope}} \quad (9)$$

Usually, reference slopes values of 0.95 – 1.0 are feasible.

The quotient of the reference slope, as it is clearly the ratio of deflection vs. Z -movement on a hard surface, can be also used to double-check the calibration of the instrument. In an ideal setting, the change in D equals exactly the change in Z , when measured on a hard surface with a hard cantilever tip. Outlying values (< 0.8) suggest that the conversion of the deflection to a signal is improper, hence the calibration of the instrument is not optimal.

3.2.3. Application of AFM imaging and indentation of collagen fibrils

Collagen fibrils are preferably imaged in contact mode in air, to select segments to be observed. Mechanical properties are usually analyzed in PBS environment, which is close to physiological conditions of the fibril in the human body. The commonly employed probes for collagen fibrils is cantilever tips with a radius of 5 – 10 nm , and a cantilever spring constant depending on the expected fibril stiffness, at the 0.1 – 1 $\frac{N}{m}$ order of magnitude.

The indentation modulus is then evaluated from the force-displacement data with the Oliver-Pharr method [23], [46], [57], [75]. To meet the assumptions of the Oliver-Pharr and Hertzian theories (indentation of a flat surface of a semi-infinite half space) only the indentation curves located at the top of the fibril cross section shall be considered [48], [75]. Due to the transverse isotropy of the collagen fibrils, not only the transverse, but also the axial modulus contributes to the modulus measured by indentation, because of the partly lateral reaction forces on the cantilever tip. Therefore it is preferable to denote the value yielded by indentation as indentation modulus [39].

Resulting from the viscoelastic properties of collagenous tissues, the rate of loading during mechanical testing has an effect on the outcome of the stiffness. That is, a higher rate corresponds to a higher resulting stiffness during an indentation experiment [23]. Still, an indentation velocity up to $10 \frac{\mu m}{s}$ should not induce stiffening effects on the collagen fibril [24].

The surface of a fibril demonstrates a certain roughness in the length scale of a few nanometers. Although the alternation of gap- and overlap regions would imply differences in fibril mechanics along the axis during an AFM indentation experiment, the D-band pattern induces differences in E-modules only in the outer shell of 2 nm but not in the fibril's bulk [58]. Thus, a minimum indentation depth is desired, along with a maximum depth of 10% fibril diameter to comply with the theories of HERTZ, OLIVER & PHARR [55], [76].

3.3. AFM measurements applied in this thesis

Mechanical properties of identified fibril segments were examined by AFM nanoindentation in PBS, initially in their unmineralized state, and after all stages of chemical modification according to a specific workflow (Figure 37).

3.3.1. The used AFM equipment

The atomic force microscopy system consisted of multiple individual units (Figure 20): an inverted light microscope (Zeiss AxioObserver.D1, Carl Zeiss Microscopy GmbH, Jena, Germany) with a remote-controlled stage (MotStage SM-01-0047, JPK Instruments AG, Berlin, Germany) was enclosed in a sealable chamber, and insulated by an anti-vibration table.

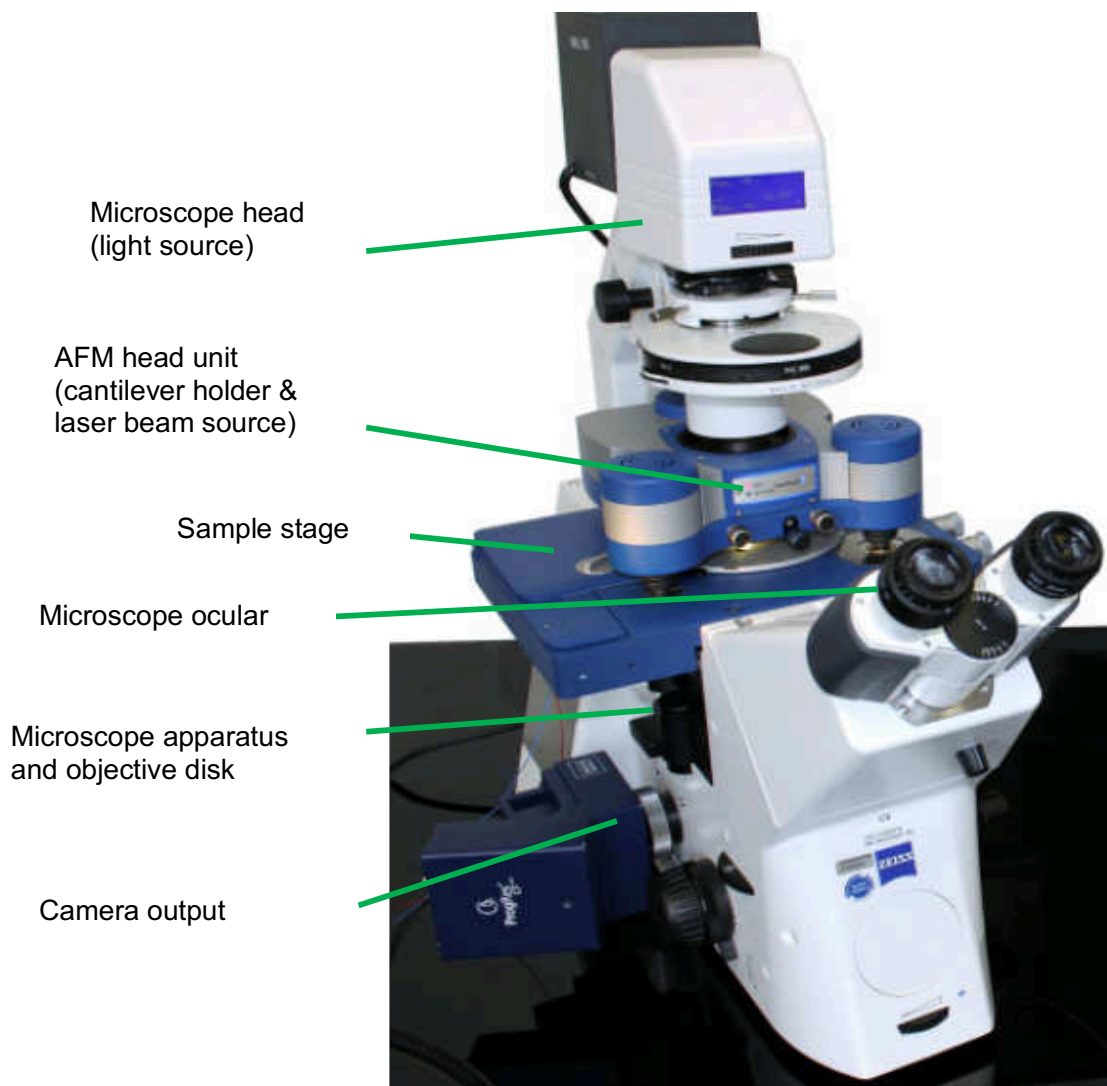


Figure 20: Illustration of the assembly of the employed AFM equipment

The microscope had 16X and 32X objectives installed, and provided up to 10X additional magnification. Image output was available through the ocular or through a camera. The AFM microscope was equipped with the head unit Nanowizard Ultra S JPK00796 (JPK Instruments AG, Berlin, Germany). The precision head unit hosted adjustment knobs for laser positioning and image panning. The activation of the laser beam, such as the vertical Z-position of the head unit was computationally controlled with the help of the JPK Nanowizard Control Software, version 5.0.82 (JPK Instruments AG, Berlin, Germany). The head unit was equipped with a removable prism which conducted the laser beam (Figure 21) and accommodated the AFM chip, a pyrex-nitride probe type PNP-DB (NanoWorld AG, Neuchâtel, Switzerland). The chip could be manipulated with a tweezer, and carried rectangular cantilevers A & B on both ends.

The pointed cantilever ends hosted the pyramidal probe tips. The applied chips were numbered, and their top and bottom ends were noted, so that an exact identification system was established.

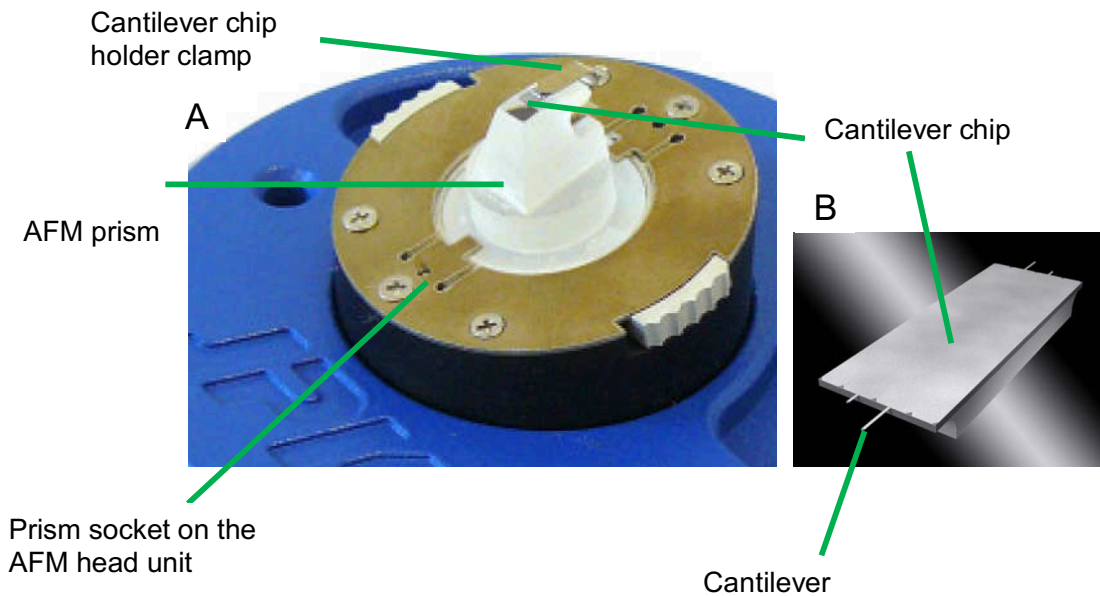


Figure 21: Cantilever holder of the AFM head (A), & magnified illustration of cantilever chip (B)

3.3.2. Instrument settings

All AFM measurements during the experiment sessions were carried out with indentation speeds in the range of $150 - 200 \frac{nm}{s}$, to avoid potential artifacts related to speed (3.2.3).

In our measurements, the indentation depth (max. 10%, as described in 3.2.3) was controlled on the basis of the terminal force, while the control could also be driven by the voltage signal or the deflection of the cantilever. Terminal forces between $0.1 - 1 nN$ were utilized, and specifically calibrated for each type of fibril sample (see 3.3.6.1).

The surface contact point (setpoint), indicating the end of the approach and the beginning of the indentation load phase (Figure 18, b) was hard to detect accurately. Therefore, a threshold level of the deflection signal voltage was used as a trigger for signaling the surface contact. That is, the slightest deformation of the cantilever end, reaching a surface, would result in a change of the deflection voltage. Threshold values of the setpoint deflection were chosen to be $0.4 V$ (cantilever A) and $0.8 V$ (cantilever B). This was enough to detect the end of approach without impacting the surface of the fibrils.

3.3.3. Employed working modes of the AFM

All measurements were taken in contact mode, where the direct bending of the cantilever, hence the deflection signal dD , was used as a feedback signal for the Z-position (3.2.1.1).

3.3.3.1. Imaging

In imaging mode, the topography of samples was extracted by scanning over the surface with the tip constantly being in contact with the surface. After applying the appropriate setpoint voltage, an approach was established, so that the cantilever tip gradually advanced towards the surface while constantly monitoring the occurrence of contact by the feedback loop.

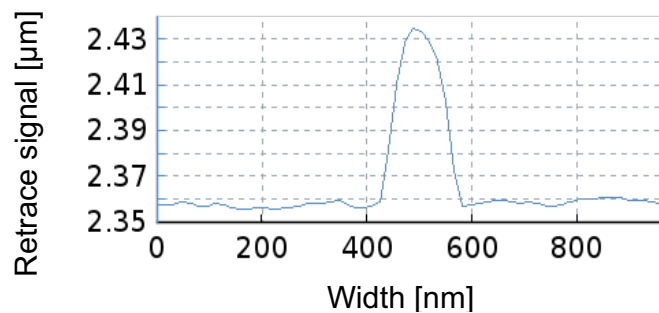


Figure 22: Illustration of the retrace height signal in one cross-section of a fibril image. The change of the deflection was the signal source, hence the height was in reference to the offset of $2.36 \mu\text{m}$.

Once the approach was finished and the tip was in contact, an image could be scanned, whereby the surface was scanned stepwise in lines by the cantilever tip. Topographical features resulted in vertical deflection of the tip, inducing adjustments of the cantilever height (Z) by the control loop. Thus, height-images of fibrils could be created (Figure 22). The line rate i.e. the scan speed was set to 0.3 Hz . Sample areas were imaged with a $6.4 \text{ px}/\mu\text{m}$ resolution, while $2 \mu\text{m}$ long fibril segments were imaged with a $64 \text{ px}/\mu\text{m}$ resolution (see final protocol in 3.5).

3.3.3.2. Quantitative Imaging (QI)

The QI mode of the JPK is a tool to provide topography data from the samples which cannot be scanned in line-traces. During QI measurements, height data was obtained through separate shallow indentations on every pixel. After each pixel, the cantilever retracted vertically, moved to the next pixel, approached and indented again (Figure 23).

The setpoint force of 0.4 nN was used for all QI experiments. Additionally, the Z-length had to be set, which implied the height amplitude of the approach and retract phases between pixels. It was always set higher than the highest expected geometrical feature of the scanned sample. Extend (approach) and retract times were both set to 10 ms . Sample areas were imaged with a $6.4 \text{ px}/\mu\text{m}$ resolution, while $2 \mu\text{m}$ long fibril segments with $32 \text{ px}/\mu\text{m}$ resolution.

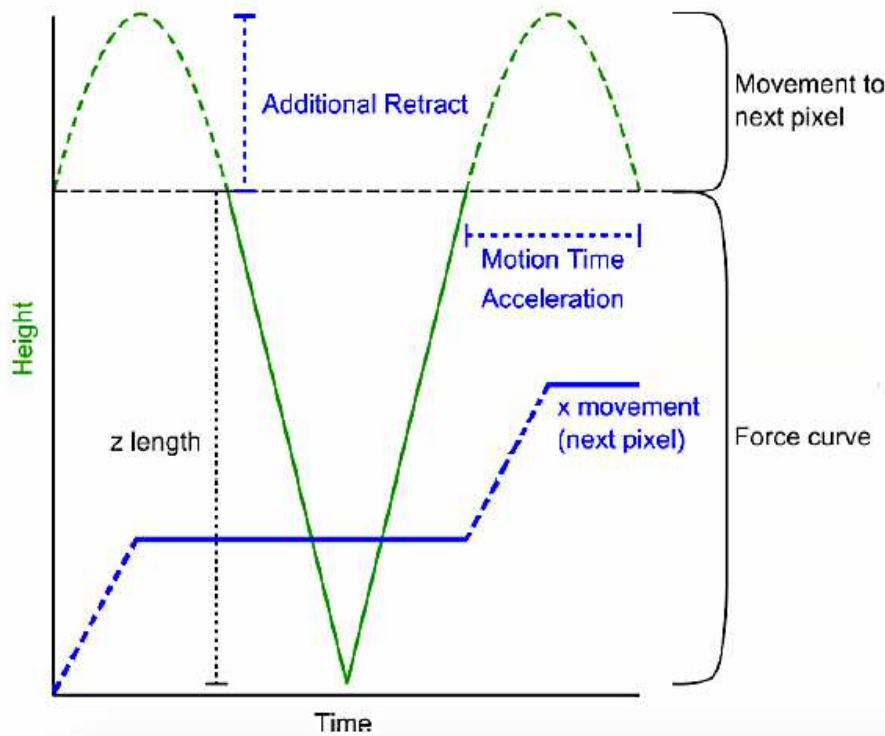


Figure 23: Illustration of the movement of the cantilever tip while capturing a pixel in a QI run [71]

3.3.3.3. Force mapping

The force-displacement relations introduced in Chapter 3.2.1.2 served as a basis for the force-mapping mode, which applied multiple indentation measurements on a predefined sample area. In case of force-mapping, the sample is indented until a defined depth and the resulting force-displacement data is registered, in contrast to the QI mode. As a result, a map of a predefined area, containing a fibril segment, was created, which consisted not only of height data, but also measured dD - dZ plots corresponding to indentation moduli (Figure 18).

3.3.4. DZ-relation and the reference slope

The force & displacement were not directly obtained from the indentations. Raw $D - Z$ data were used as a basis for the calculation of the contact stiffness (Equations 2-5). As elaborated in Chapter 3.2.2.3, the raw D/Z ratio was corrected with a reference slope, using Equation 9.

The reference slope itself was obtained before and during the measurements of each sample, as the mean of 320 measured dD/dZ slopes on a hard surface (mica). Indentation on a hard surface resulted in a slope value which corresponded to the mechanical compliance of the cantilever tip. This (reference) slope was then cancelled from the measured contact stiffness of each sample indentation to yield the actual contact stiffness (3.2.2.3 & 4.1.1).

3.3.5. Calibration for sensitivity and determination of spring constant

Each cantilever used in the experiments were calibrated for their *invOLS* sensitivity prior to sample measurements, using the calculations introduced in 3.2.2.2. As the sensitivity varies in different environments, *invOLS* was measured both in air and in the used PBS solution.

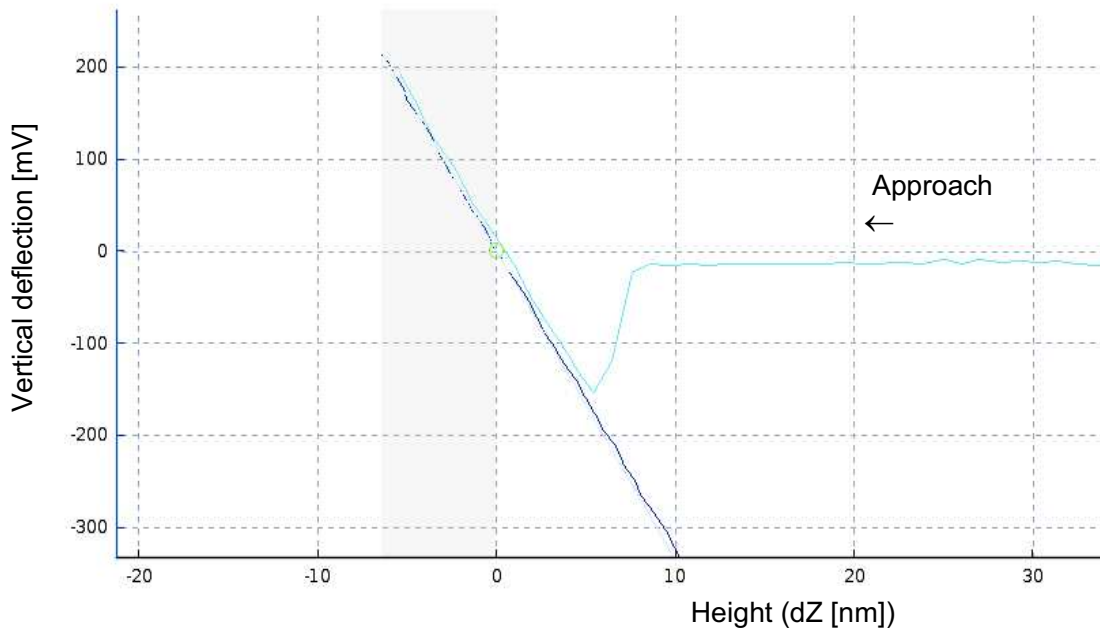


Figure 24: Example of a sensitivity calibration in air, on mica surface (unloading slope in dark blue)

3.3.5.1. Sensitivity in air

To calibrate the arbitrary *invOLS* value of the cantilever, 16 indentation measurements were conducted on clean mica surface in force map mode, over a $10\ \mu\text{m} \times 10\ \mu\text{m}$ square area, with 4×4 indentation resolution. Indentation speed was set to $2.0\ \mu\text{m}/\text{s}$, Z-length to $1\ \mu\text{m}$ and the relative setpoint to $0.4\ V$. The average value of the resulting OLS slope (Figure 24) were taken after observing the distribution of the force map. The inverse of this value (*invOLS*) was then taken as the sensitivity of the cantilever.

3.3.5.2. Measurement of cantilever spring constant

The JPK software provided a built-in interface for determining the spring constant by assessing the power spectral density (PSD) of its resonance to thermal fluctuations in ambient air. The thermal noise method uses the equipartition theorem on the Hamiltonian of the resonating cantilever, and sets up a relation between the temperature, the PSD and the spring constant [77].

Applying this method, first the apparent voltage signal resulting from the thermal noise was captured, and converted to cantilever deflection values by the *invOLS* measured in air. The deflection signal was Fourier-transformed by the software and the amplitude (power) over the frequency was plotted, resulting in the PSD graph (Figure 25). The first harmonic, the lowest frequency with the highest power, was identified and fitted with an approximation function. The area under this curve, corresponding to the mean square of the cantilever fluctuations, was used by the software to calculate the spring constant of the cantilever.

3.3.5.3. Sensitivity in PBS

The *invOLS* in PBS was calibrated to a definite relative setpoint force (terminal force), by an iterative method, employing multiple calibration steps. The iterative algorithm began with one initial calibration using the arbitrary relative setpoint voltage $0.4\ V$ as terminal trigger.

Thereafter, the determined *invOLS* sensitivity value was applied in the software along with the already determined spring constant of the cantilever, to convert voltage values to force values.

$$dF = dV * invOLS * k \quad (10)$$

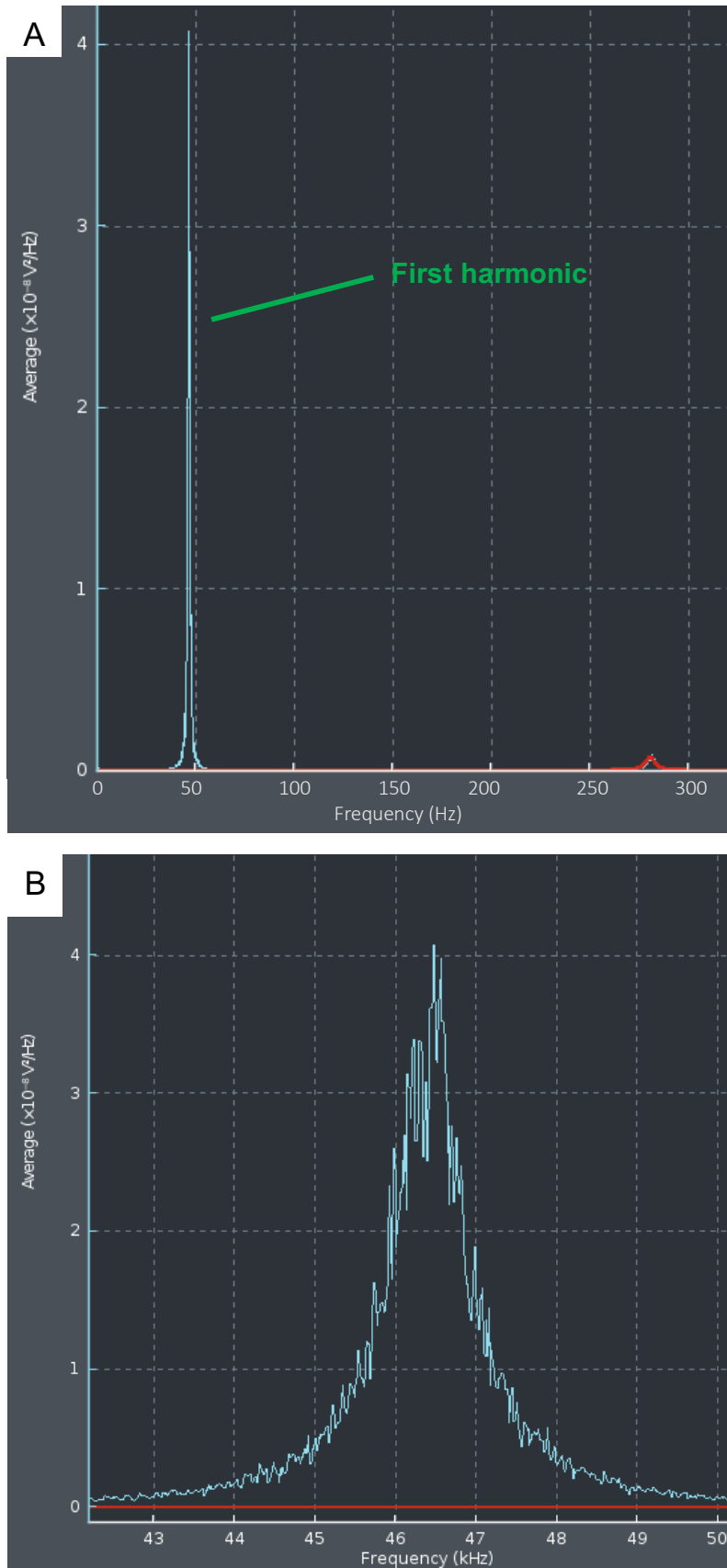


Figure 25: PSD of the thermal noise on cantilever 39A (A: full spectrum, B: first harmonic)

The thereby obtained force value was set as the new terminal setpoint value. This was again converted back to a corresponding voltage value as the new relative setpoint voltage. With this relative setpoint, a new calibration was conducted, and the whole process was repeated iteratively, until a converging behavior of the *invOLS* value was observed. This value was then taken as the *invOLS* in PBS. An exemplary OLS slope in PBS is shown on (Figure 26)

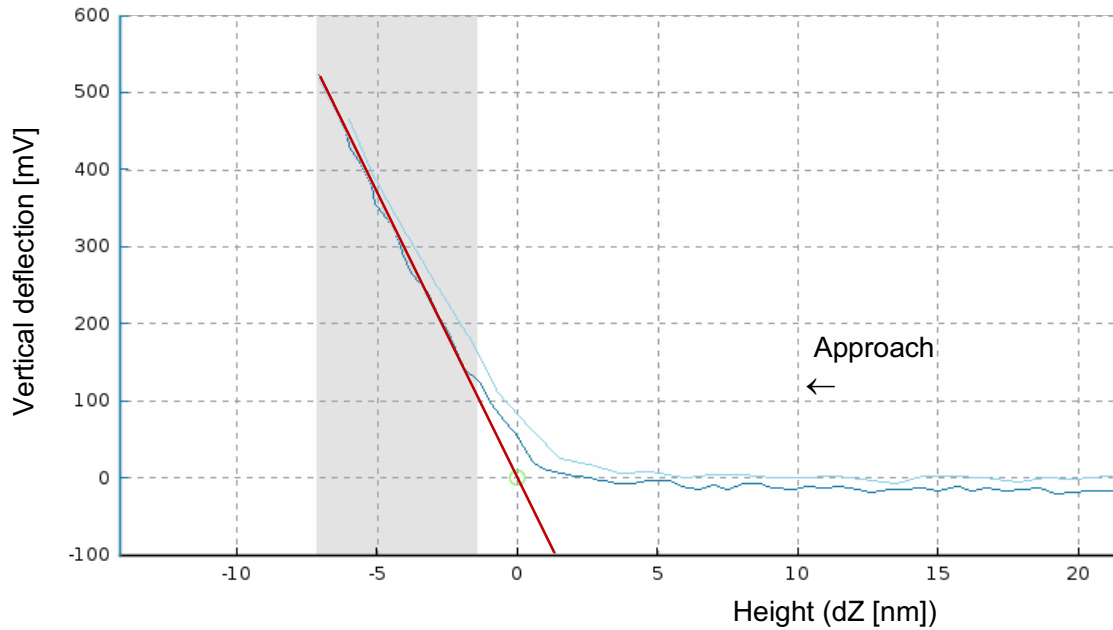


Figure 26: Exemplary plot of sensitivity calibration on mica, in PBS. Red line represents the slope fit

3.3.6. Choice of cantilever

The support chip of the multi-cantilever probe (3.3.1) of size $3.4 \text{ mm} \times 1.6 \text{ mm} \times 0.5 \text{ mm}$ was made of pyrex glass. The support chip held diving board cantilevers of pyrex-nitride, coated with gold, with lengths of $100 \mu\text{m}$ (A) and $200 \mu\text{m}$ (B), and a width of $40 \mu\text{m}$. The cantilevers had a pyramidal tip with the radius of max. 10 nm . The nominal spring constant of the cantilevers was given as 0.48 N/m (A) and 0.06 N/m (B).

The calculation for the cantilever selection was based on Equation 6, using $\beta = 1.02$, $\nu = 0.5$ and an estimated contact area $A = 6 \cdot 10^{-4} \mu\text{m}^2$ of the tip, corresponding to an estimated indentation depth of 15 nm [39]. For the expected indentation modulus in the $1 - 10 \text{ MPa}$ range (2.2.4), the contact stiffness was expected in the range of $0.035 - 0.35 \frac{\text{N}}{\text{m}}$.

Hence, the PNP chip with cantilevers A and B was an appropriate choice, with their spring constants lying in the same order of magnitude. The choice between A or B depended on the actual softness of the fibrils and the actual measured cantilever spring constant (3.3.6.1).

3.3.6.1. Measurement algorithm for the choice of cantilever

In order to conduct measurements with the right preferences, a protocol was established for choosing the appropriate cantilever and indentation force for a given sample: the loop process consisted of several test indentations, the outcomes of which were briefly analyzed to extract specific measures corresponding to the applicability of certain preferences (Figure 27).

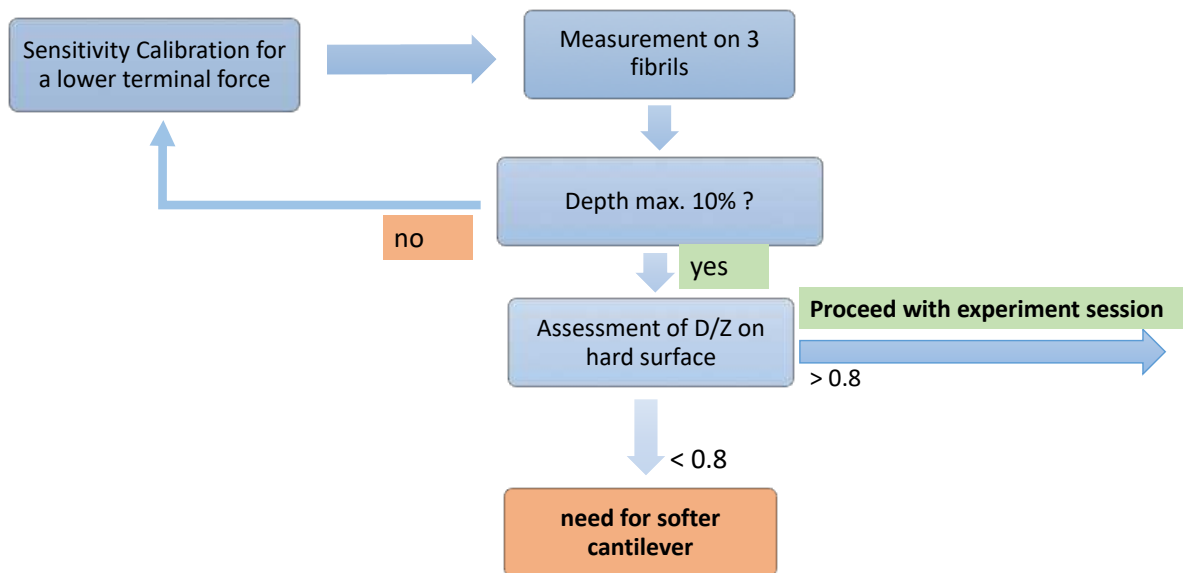


Figure 27: Calibration loop process to determine the appropriate terminal force and cantilever

At the start of the process, initial measurements on 3 random fibril segments of a sample (after preliminary imaging and identification) were taken with 0.7 nN calibrated terminal force, and first the average depth of the indentations was observed. If the depth overcame 10% of the fibril height, the indentations were conducted again with a lower terminal force until the depths fell under 10%. Thus, a fibril-specific appropriate terminal force could be determined. Then, the D/Z-slopes of the last measurement were analyzed (see 3.3.4), to assess whether the applied terminal force was appropriate for the actual cantilever spring constant to maintain sufficient deflection sensitivity. Low D/Z values on the hard substrate surface signaled that the terminal force was reached before proper bending of the cantilever, meaning that the indentation prematurely came into the retract phase, before a linear relation between D and Z existed.

In this case the accuracy of the force maps fell. D/Z values of 0.8 on hard mica surface and 0.4 – 0.55 on the fibril were used as benchmark (Figure 28).

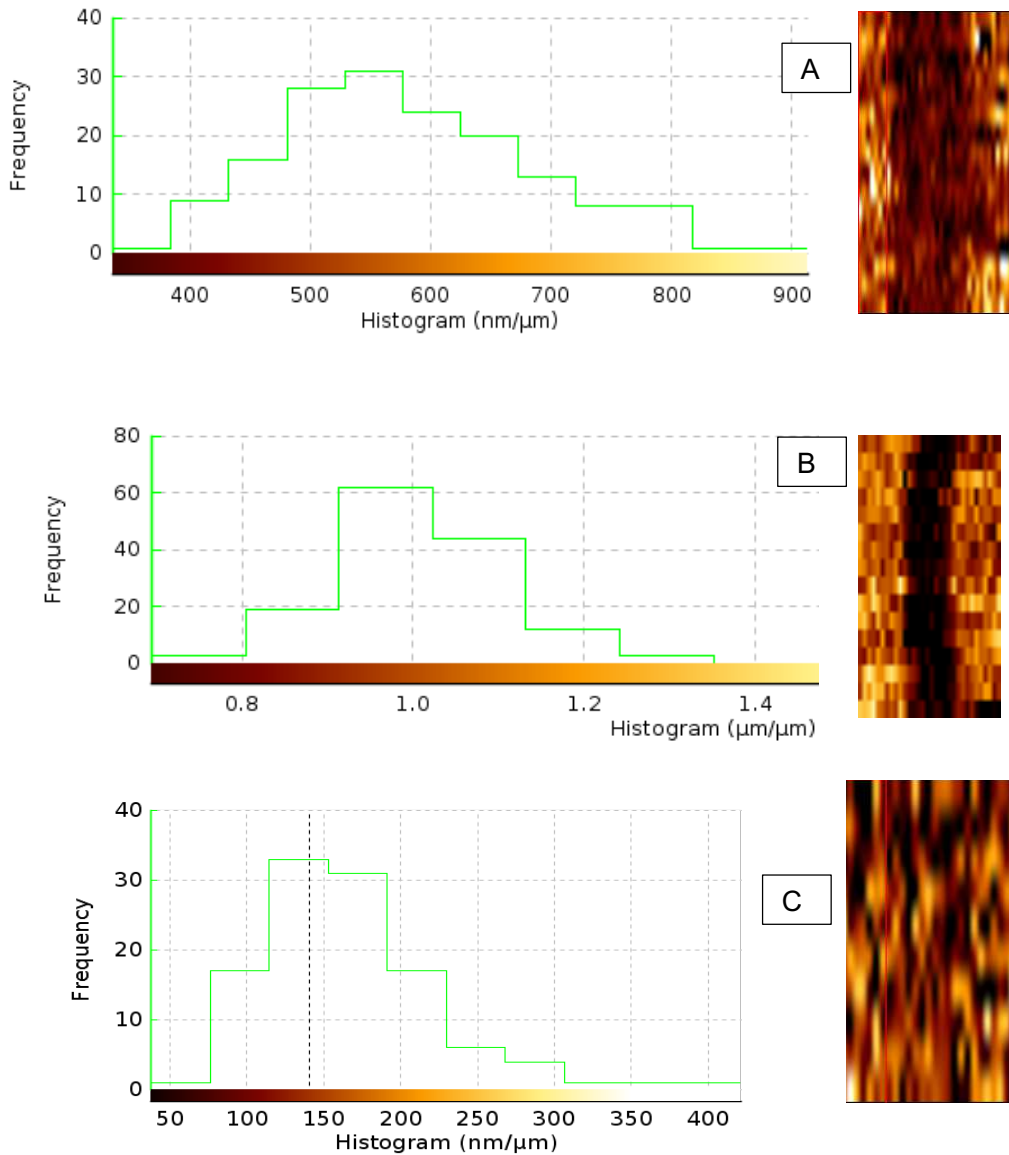


Figure 28: Reference slope histograms with corresponding force-maps on the right, respectively.

A – 0.2 nN terminal force with the stiffer cantilever A, resulting in low reference slopes (mean: 0.55).

B – 0.2 nN terminal force with cantilever B, yielding distinct reference area and appropriate reference slopes (mean: 0.96).

C – An extreme example of using cantilever A with a very low terminal force. This results in a force-map where sample features are lost and indistinct. The indentation terminates at a very low cantilever deflection already, so that similar plots are produced on either soft or hard surfaces.

3.3.7. Cantilever tip shape determination

The exact shape of the cantilever tip was an important factor to determine the contact area, applied in the calculations (Equation 5). Therefore, a precise assessment of the tip shape was necessary. In this study a pyramidal tip having an tip-radius on the nanometer-scale was utilized. Hence, the precise shape of the pyramid had to be scanned and quantified empirically.

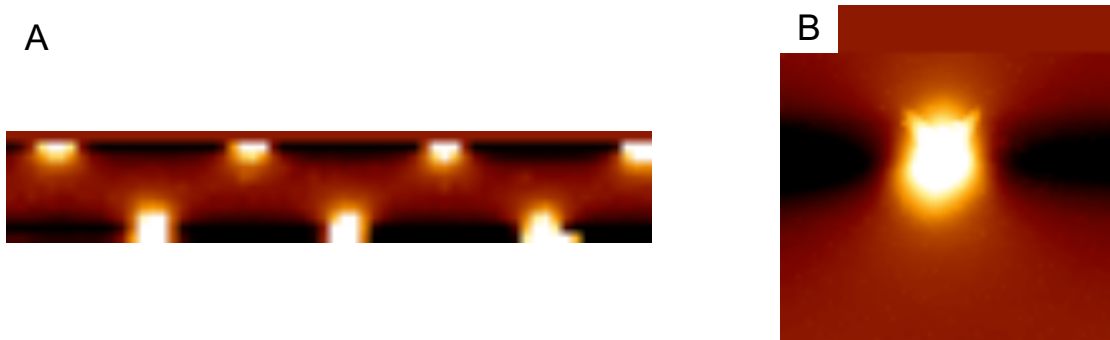


Figure 29: Imaging scan of a TGT1 surface of $10\ \mu\text{m}$ width (A), and a close-up $1.5 \times 1.5\ \mu\text{m}$ scan of one spike (B), both images with 128 pixel size.

A reference-grating (TGT1, NT-MDT, Moscow, Russia) with known surface features was imaged in contact mode (Figure 29). The silicone surface of the grating sample consisted of pointed cones. First, an overview image with the width of $10\ \mu\text{m}$ was scanned with a resolution of 128 pixels and $0.2\ \text{Hz}$ line rate, until the arrangement of spikes could be detected. The conical spikes of the TGT1 substrate are arranged in a regular sequence, in $3\ \mu\text{m}$ distance from each other, and have a nominal height of $300\ \text{nm}$. After choosing a single spike which resembled a proper image without artifacts, a scan of $1.5\ \mu\text{m} \times 1.5\ \mu\text{m}$ size was taken again with 128-pixel resolution which produced better details. The scanning line of this image which swept over the highest peak of the cone was optimized by adjusting the line rate and IGain factor of the feedback loop, to narrow the gap between trace and retrace signals (see 3.3.3.1). After setting these preferences, a highly detailed image of the spike, $1.5\ \mu\text{m} \times 1.5\ \mu\text{m}$ in size and 512×512 pixels in resolution, was scanned.

The resulting image represented the topography of a standard known geometrical shape, containing height data with the resolution of $2.9\ \text{nm}/\text{px}$, from which the geometrical shape of the cantilever tip could be deconvoluted mathematically. The mathematical deconvolution method will be further discussed in 4.1.2.

3.4. Problems affecting the measurements

Until the final measurement protocol was developed, several trial measurements had been conducted, during which the methodology had been continuously improved. All conducted AFM measurements during this study work are listed in Table 1. During method development, procedural errors were eliminated and solved step by step. The difficulties and errors which occurred, are introduced in the following subchapters.

Table 1: Summary table listing sample usage. Multiple samples were used in tryouts and during the development and optimization of the methodology, until the final measurements were made.

Sample	Measurement		
ID	Classification (ID)	Outcome	Purpose
N10	Tryout sessions	Successful indentations	Having AFM experience
R6	Development	Ended at Min2 with artifacts	Methodology development
R7	Development	Ended at Min3 with artifacts	Methodology development
N7	Development	Ended at Min1 with artifacts	Methodology development
N8	Development	Ended at Min1 with artifacts	Methodology development
N9	Development	Successfully ended loop	Cantilever choice
R8	Development	Successfully ended loop	Cantilever choice
R5	Final reconst. (R5)	Successfully ended at Min3	Evaluated in data analysis
N5	Final native (N5)	Successfully ended at Min3	Evaluated in data analysis
N1	Additional (A1)	Successfully ended at Min0	Evaluated in data analysis
N2	Additional (A2)	Ended at Min1_EDTA	Evaluated in data analysis
N6	Additional (A3)	Ended at Min1_EDTA	Evaluated in data analysis

3.4.1. Fibril identification

It was important that the exact same segments of the same fibrils were measured in all stages of a measurement session. In most cases it was hard to find and identify the previously chosen fibril segments in a variable environment, because of changes in the sample area due to the chemical modifications (precipitations). Therefore, in case of all new sessions, the first step was to visually assess the sample area on a macroscopic level, and identify smaller areas where multiple fibrils were available, which were judged to be locatable in all measurements.

Isolated fibrils were preferred, without any mergers or twirls, distinctly positioned in a clean environment. After microscopic assessment, the chosen areas were imaged in air by AFM imaging, and prospective sample fibril sections were defined. The coordinates of the motorized AFM stage position were registered, so that the same position on the sample slide could be found again in the forthcoming stages of the measurement session. The position of the sample glass slide on the microscope stage was also marked to secure the positioning in later steps (the slide was demounted from the microscope stage between each step of the experiment). Thus, a fixed basis system was created where the position of the particular fibrils was always known.

The detachment of native samples from the substrate slide was a recurring phenomenon after multiple treatments. Typically, after 80 hours in an ionic fluidic environment, native fibrils and fascicles came off the substrate and dislocated. As an improvement, the native samples were rather deposited on more adhesive poly-l-lysine (PLL) substrate slides instead of regular glass slides.

3.4.2. Measurement of the reference slope and calibration of sensitivity

It was first practicable to calibrate the sensitivity and determine the reference slope on a clean area of the sample slide close to the fibrils, in a steady environment as seen on Figure 30.

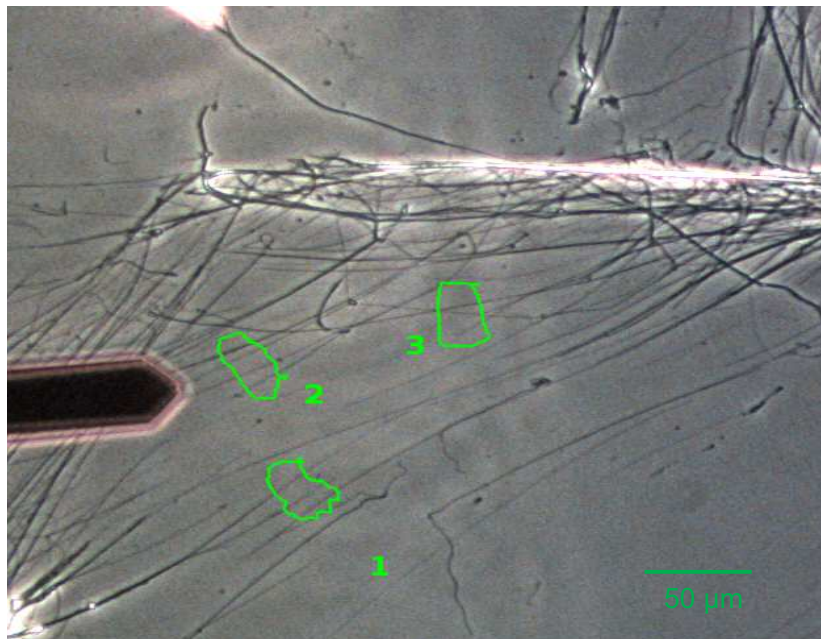


Figure 30: Example of appropriate sample regions. Native fibril segments, which are chosen for measurement, are defined in circular areas

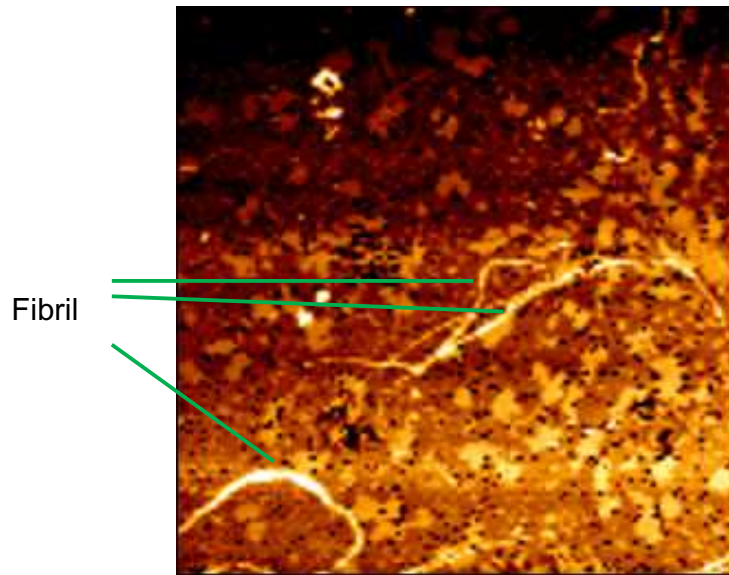


Figure 31: Sample area of *in vitro* reconstituted fibrils ($20 \times 20 \mu\text{m}$, $128 \times 128 \text{px}$). Chemical residues appear as patches on the sample substrate, so that fibrils can be hardly identified.

However, the reference slope measurement in the sample area always resulted in very adverse reference slope values, under 0.8. This was due to a thin film of chemical residues, which precipitated on the sample substrate already during the generation process of reconstituted fibrils (Figure 31), and additionally during mineralization steps (Figure 32). Thus the surface was not sufficiently plain and hard, and could not be used for the calibrations.

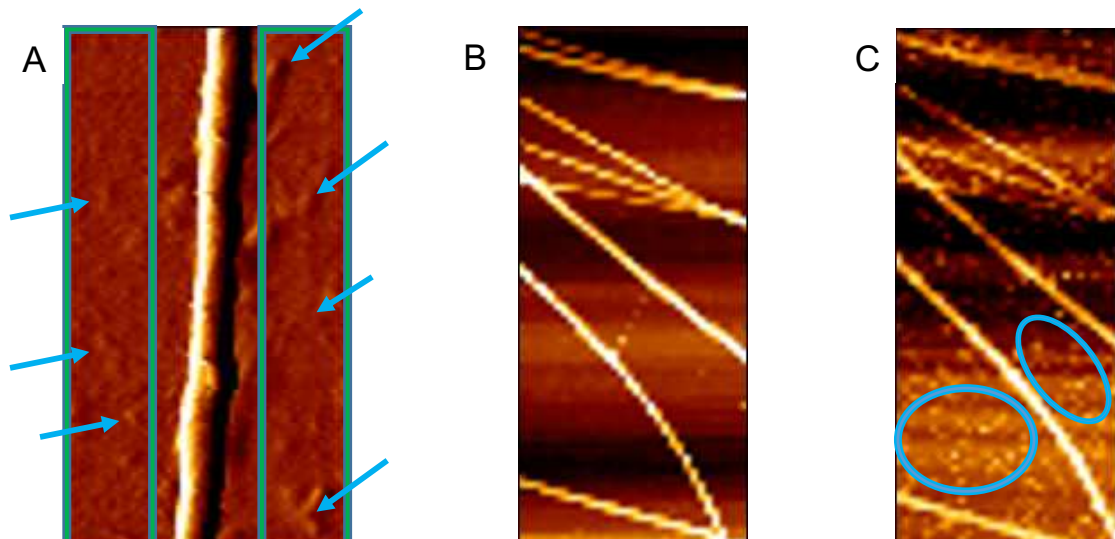


Figure 32: A – originally planned measurement area for reference slopes illustrated on a $0.8 \times 2 \mu\text{m}$ fibril image (green brackets). Surface impurities and precipitation residues are marked with arrows.

B – $10 \times 25 \mu\text{m}$ sample area of native fibrils before mineralization treatment.

C – The same sample area after mineralization. Sample substrate is contaminated (blue circles).

Thus, the sensitivity calibration and the capture of reference slopes had to be conducted elsewhere, but still inside the current fluid cell. Therefore, a $\varnothing 12\text{ mm}$ muscovite mica disk (NanoAndMore GmbH, Wetzlar, Germany) was fixed inside the fluid cell. The mica was glued on the sample slide by the two-component adhesive UHU Plus Epoxy Ultra Quick (UHU GmbH & Co. KG, Bühl/Baden, Germany). All sample slides were prepared alike (Figure 33).

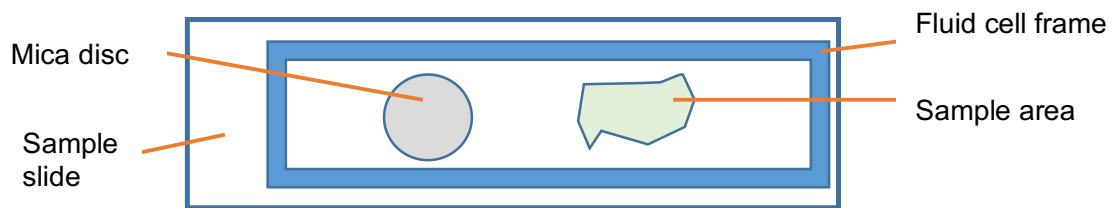


Figure 33: Schematic illustration of the prepared sample slide with fluid cell, mica & sample area

The mica disk could be used to provide new clean and plain surface after every treatment step, by removing some upper layers with an adhesive tape. Thus, the calibration and reference slope steps could take place inside the fluid cell on the sample slide by driving the head away from the sample onto the mica. This method was proven to be fruitful to yield feasible data.

3.4.3. Contaminations on the fibril

It was observed following control mineralization treatments, that relatively large crystals precipitated from the solution and deposited on the substrate as well as on the fibrils (Figure 34). This inhibited proper measurements in most cases, because the crystallization covered the indentation target points.

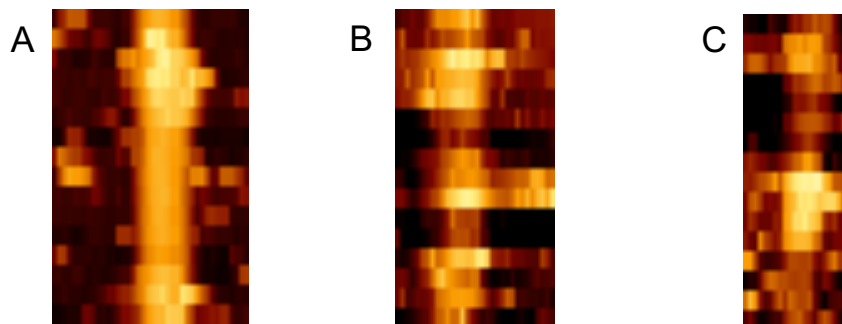


Figure 34: Qualitative examples of contaminated fibril segments (force-maps, $2\ \mu\text{m}$ length), $32 \times 16\text{ px}$

As a resolution, a thorough rinsing process was carried out using distilled water after each chemical treatment step. It was important to rinse the sample directly after taking the slide out of the tube, to prevent the deposition of contamination due to drying.

The treatment in “normal” mineralization solution induced similar effects. However, the contamination effect occurred with much smaller crystal sizes due to the presence of fetuin. Ethylene-diamine-tetraacetic acid (EDTA) was used when needed, as a complementary rinsing substance. Ten seconds after deposition on the sample, the 0.5 M acidic solution was rinsed thoroughly with DW, to hopefully prevent dissolving minerals from inside the fibrils.

3.4.4. Laser interference

In the approach part of the D/Z plot, which is supposed to be a flat signal (Figure 18 a-b), a regular sinusoidal wave form was observed (Figure 35).

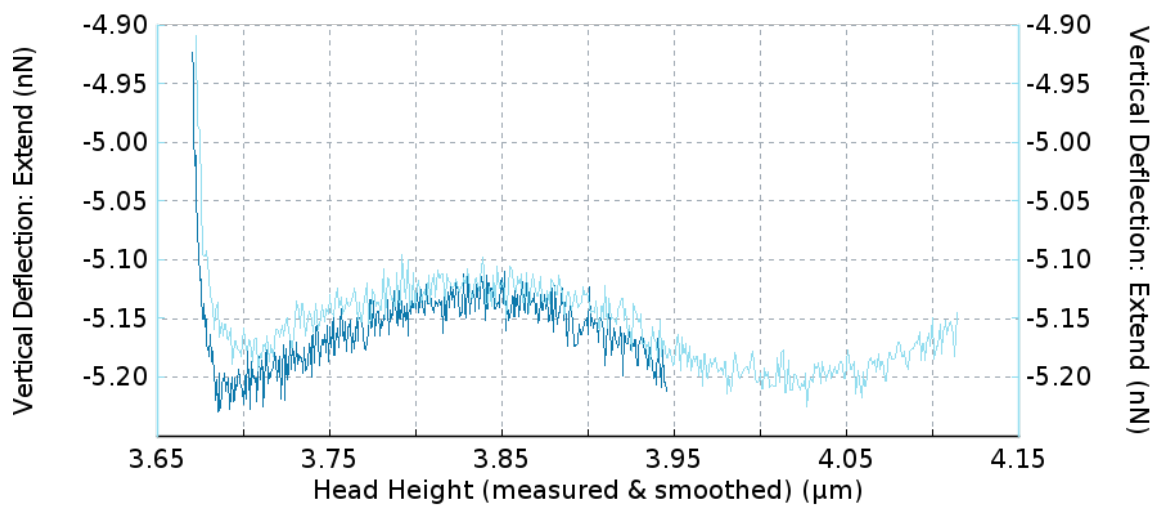


Figure 35: Example of a force-deflection indentation plot with overlapping sinusoidal waves

The reason was the interference of the light waves of the laser (Figure 36) with their reflections from the substrate surface. The problem could be resolved by repositioning the laser beam further towards the stem of the cantilever, with safe distance from its tapered end.

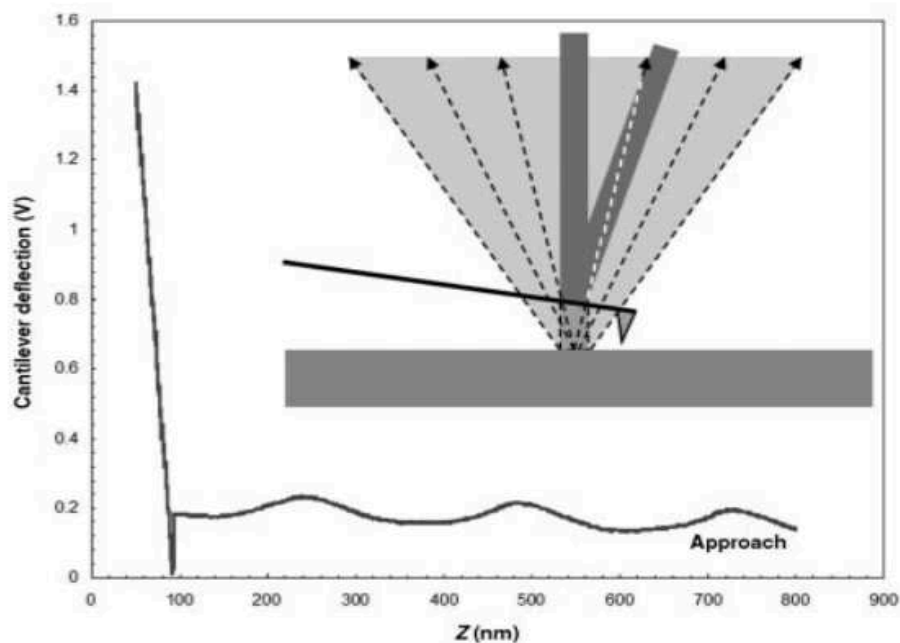


Figure 36: Illustration of an interfered approach signal on an indentation plot, and its cause [61]

3.4.5. Indentation depth

In many measurements, the indentation depth largely exceeded the limit of 10%: often 20-30% were observed in case of reconstituted fibrils. First, all samples were measured with the same type of cantilever (A). Due to high depths, the method for the suitable cantilever selection was established (3.3.6.1). This also elicited another artifact, namely the excess of crystalline contaminations on previous indentation points: traces left by a deep indentation on these segments supposedly provided a favorable spot for large-scale crystallization. Based on the finally developed calibration loop process (Figure 27), the softer cantilever B was determined to be appropriate on the reconstituted fibrils, indenting under 10% depth of the fibril height.

3.4.6. Fibril softening

The analysis of the indentation modulus of the first 3 measurement steps (PBS/Min0/Min1) yielded, that the modulus of the fibrils did not increase throughout the steps, but rather decreased remarkably. This was supposedly correlated with the long time exposure to a tempered fluidic environment with high ionic content. Both native and reconstituted fibrils demonstrated a swelling behavior under aqueous circumstances, which primarily took place rapidly after changing the environment, and secondarily over the entire measurement session.

Along with that, a decrease of indentation moduli took place during the first 3 stages of a measurement session. The two phenomena were supposedly correlated: due to the infiltration of water molecules in between collagen molecules, filling all voids, the inner fibril structure softens [23].

This effect was cancelled by pre-conditioning all sample fibrils before the particular measurement session. This took place in a mailer tube in a duration of 2 days under 37 °C in PBS environment. Thus, this process always took place beforehand not to affect the eventual changes in mechanical properties which took place subsequently during the introduced chemical modifications.

3.5. Final measurement protocol

Finally, the following workflow (Figure 37) was established to yield the aspired experimental data – it incorporates all the empirical findings and working modes which were described above: first, a sample of native (3.1.1) or reconstituted fibrils was deposited on a slide. A mica plate of Ø12 mm was glued next to the sample area. The mica plate and the sample was then enclosed in a fluid cell, by gluing a thin polypropylene frame of 3 mm height on the sample slide (Figure 33). After carrying out the TGT1 and calibration process (Chapters 3.3.5 & 3.3.7), the collagen samples were imaged in air by AFM contact mode imaging.

Nine appropriate fibril segments were identified for subsequent measurements. The sample was preconditioned in PBS solution under 37 °C for 48 hours, to controllably produce swelling and softening effects before the actual chemical modifications start. Afterwards, the sample was scanned (QI mode) again, and the 9 chosen fibril segments were indented in PBS, by force-mapping an area of size $1 \times 2 \mu\text{m}$. During the force-map capture, the longitudinal axis of the fibril segment was aligned to the longitudinal (slow) axis of the image.

The resolution of the force map was always chosen appropriately to the fibril segment width, so that 16 indents were present along the fibril longitudinally, and at least 10 indentation points situated on the fibril in the cross-sectional axis (Figure 38). Thereafter, the sample was put into the control mineralization solution without fetuin for 20h, and the same segments were measured again after identifying them by QI.

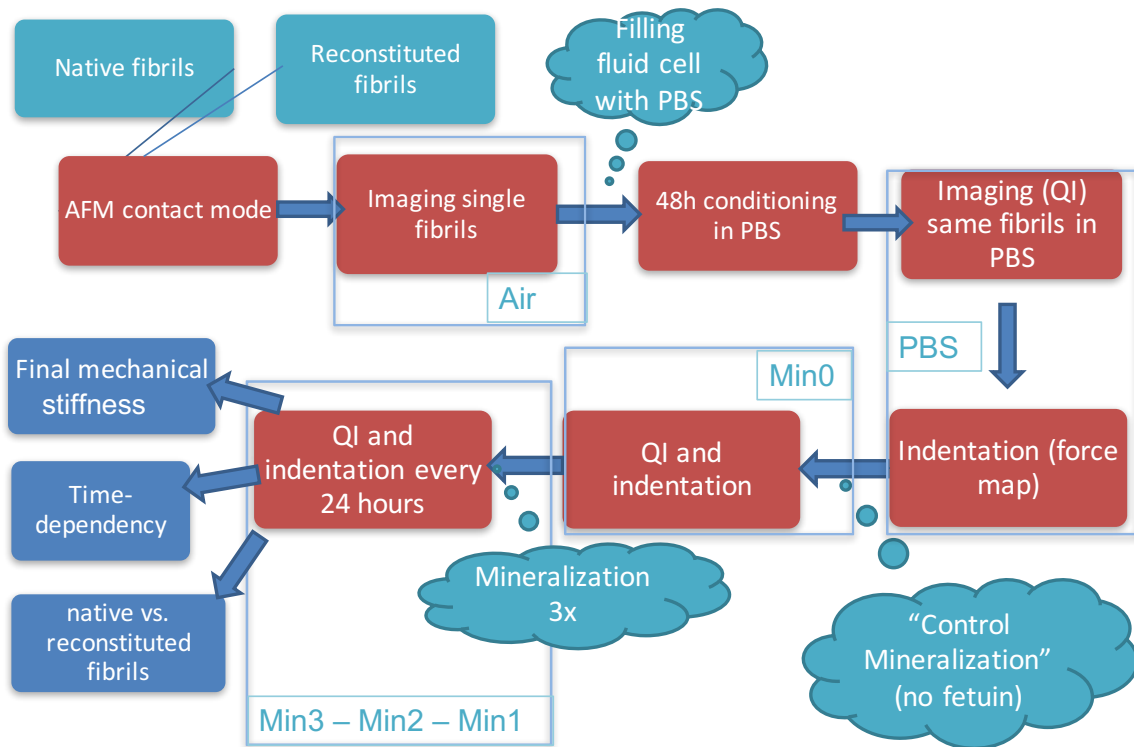


Figure 37: Workflow of an experimental session including chemical and nanomechanical methods

This step was followed by 3 “normal” mineralization steps (“Min1”, “Min2”, “Min3”) using a solution containing fetuin, where actual modification of the fibrils was expected. After each step, the same fibril segments were identified by QI and indented by AFM indentation.



Figure 38: A force-map ($0.8 \times 2 \mu\text{m}$) of a native fibril in PBS, before chemical modification (showing measured height). The size of an indentation-pixel is marked by the yellow rectangle.

This experiment process for a collagen fibril sample was called a “full measurement session”. A full measurement session was carried out for a native (N5) and a reconstituted (R5) sample. R5 underwent no preconditioning. Many samples had been consumed in the course of experiments which had failed due to above mentioned issues.

All indentation measurements took place in PBS of pH 7.4 (see 3.1.4), to avoid adhesion effects and artifacts caused by air humidity. The sample area in the fluid cell was washed with DW between all measurements and mineralizing steps to clean off residues. Thereby, the sample area was rinsed, by repeatedly diluting the persisting solution first, to prevent micro-drying of the sample surface which would result in contaminations in form of mineral residues and precipitations. After diluting with DW, the fluid cell was emptied, and rinsed over with DW multiples times, whereby direct application on the fibril area was avoided to prevent fibril dislocation.

Following each chemical treatment, a new mica surface was created by removing a few layers of the mica platelet after rinsing the fluid cell. New calibration of the AFM was carried out before every measurement step according to Chapter 3.3.5. Rinsing with EDTA had to be carried out only in case of the native sample (N5), after the Min1 and Min3 steps. Subsequent force-map measurements were then labelled as “Min1_EDTA”, or “Min3_EDTA”.

3.5.1. Additional experiments

Alongside the full measurement sessions of a native and a reconstituted sample (Figure 37), complementary experiments were planned and conducted. These were especially focused on the analysis of the effect of contaminations on the measurements. Apart from that, the second focus was on the examination of the effect of the pre-conditioning. For this purpose, 3 native fibril samples of the previously prepared lot (3.1.1) underwent shortened measurement protocols (Figure 39).

- A1. (sample N1): Pre-conditioning for 48h, indentation in PBS, and after a 20h Min0 step
- A2. (sample N2): Pre-conditioning for 48h, indentation in PBS, and after a 20h Min1 step
- A3. (sample N6): Pre-conditioning for 2h, indentation in PBS, and after a 20h Min1 step

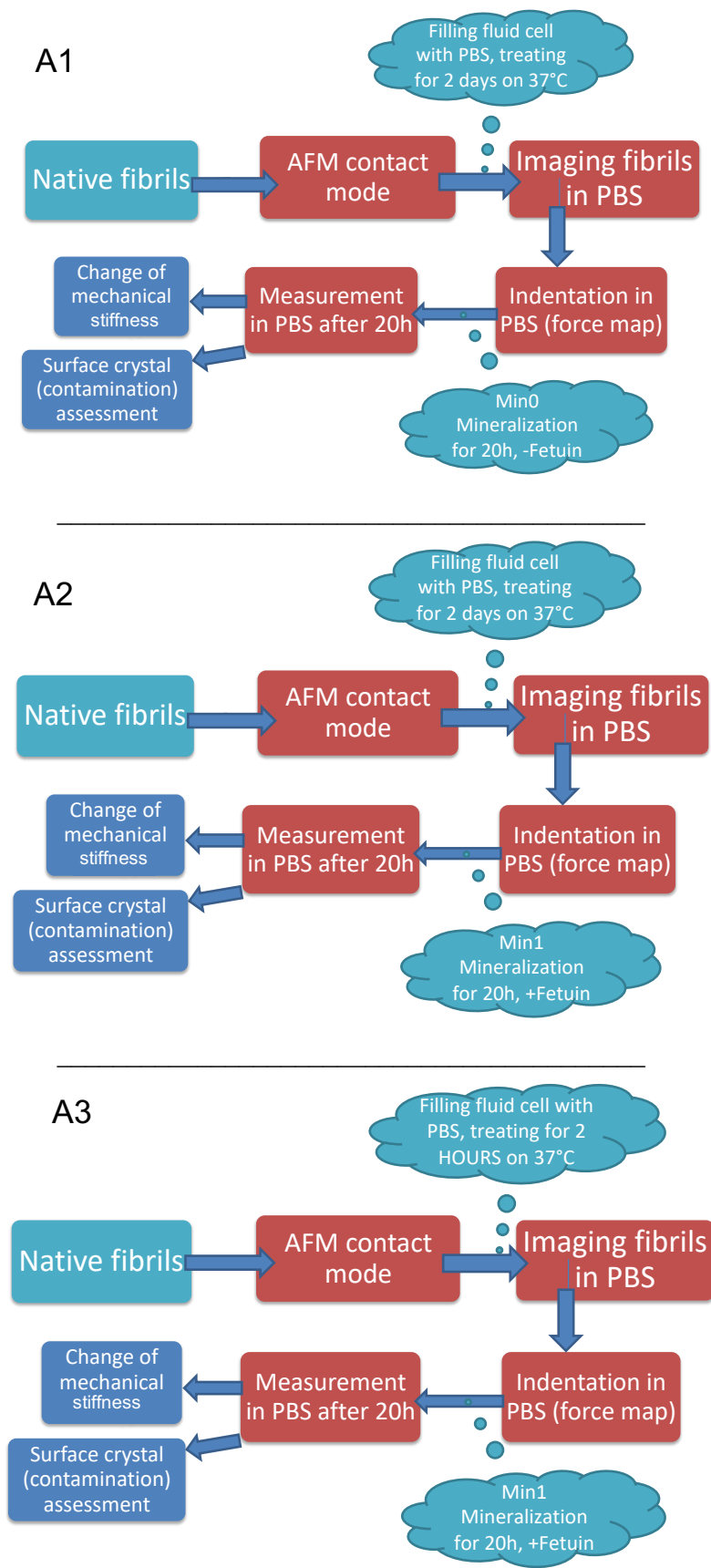


Figure 39: Measurement protocols for the 3 additional samples (A1, A2, A3)

Thereby, A1 was compared to A2 regarding the contamination behavior after undergoing solely a Min0 or a Min1 step. Along with that, A3 was compared to A2 concerning the effect of the different pre-conditioning durations on the softening behavior, i.e. the values of the subsequent indentation moduli. For A2 and A3 undergoing the Min1 step, EDTA had to be applied because of contaminations (3.4.3). These samples were indented before (Min1) and after (Min1_EDTA) the rinse.

4. Data analysis

4.1. Measurement preferences

4.1.1. Reference slopes

The reference slopes, which were captured for every fibril segment separately on the mica (see 3.3.4), were analyzed in the software JPK Data Processor, spm-5.0.82, (JPK Instruments AG, Berlin, Germany). In the software, a process was applied which extracted and plotted tip deflection (dD) data over the Z -displacement (head position dZ). Thereby, the raw deflection signal in *volts* (dV) was converted with the calibrated *invOLS* coefficient (see 3.3.5.3) to yield the dD value for the displacement of the tip, as described in (3.2.2.3 & 3.3.4).

The inclination of the first 15% of the produced slopes was taken as a measure of the ratio, and an average was built over an entire force map of 20×16 *pixels*, taken on the mica over an area of $0.67 \times 2 \mu m$. The average value was taken as the reference slope value ($\frac{dD}{dZ}$). This was expected to lie very close to 1.0, as it is obvious, that in case of pushing the cantilever tip on an infinitely hard surface, the further Z -displacement of the head equals the deflection of the cantilever tip relative to the head in opposite direction ($dD = dZ$).

4.1.2. Cantilever tip shape

The shape of the cantilever tip was important to be determined to be able to employ the exact value of the contact surface in the calculations for every nanometer of depth (Chapter 3.3.7). The image height data was acquired via the TGT1 process introduced in 3.3.7. The data was analyzed by Matlab R2019b (Mathworks, inc., Natick, USA), on a Linux OS, using a script developed by DR. ANDRIOTIS.

The input height image basically represented the height coordinates of every contact point of the cantilever tip on the imaged TGT spike, with a resolution of 2.93 nm/px . From that image data, the shape of the cantilever could be determined by a deconvolution process, as introduced by KELLER and FRANKE [78].

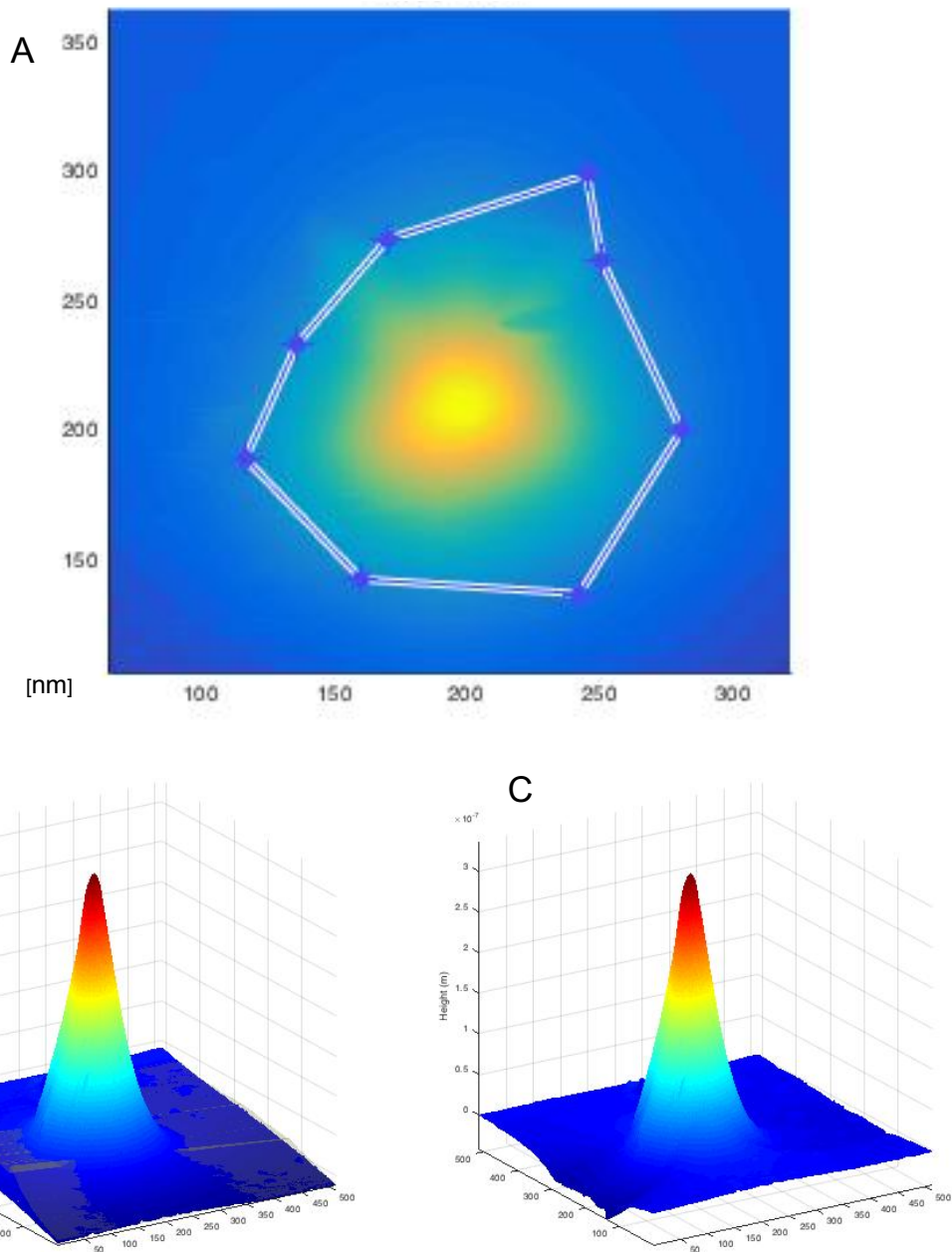


Figure 40: Height image of a TGT1 spike as it appears in the MATLAB process (A), and 3D view of the data (C). Reconstructed 3D-shape of the cantilever is illustrated qualitatively (B).

First, the image file was input, and height data corresponding to X-Y coordinates was read out. Then, the position of the spike was manually determined (Figure 40, A), and further evaluated by the process. From the height data of the spike, the tip shape was determined by deconvolution, comprising of X-Y coordinates allocated to tip height (Figure 40, B). Thereby, the surface points of the tip, in every height nanometer running from the tip end, were determined and included in a vector array in MATLAB.

4.2. Sample analysis

4.2.1. Morphology

The force-maps of fibril segments were not only analyzed to extract force-displacement plots from the indentation data, but also height data was extracted. The force-map dataset contained the coordinates for the contact point (setpoint), indentation depth, and corresponding cantilever deflection signal values in each indentation point. From this dataset, the height-coordinates for the contact point, i.e. start of the indentation (Figure 18, point b) could be mapped in a MATLAB process, thereby creating a height-image for the force-map area.

This height image included the 2D topography image of the analyzed fibril segment, from which the maximum height of the fibril could be extracted by the script process in each of the 16 cross-sections, in reference distance to the surrounding sample substrate surface. Thereby, the reference surface line was determined as the medial line of the surrounding contact points distinct from the fibril shape. The distance of the highest point in the cross-section from the reference was implied as the fibril height (diameter). Fibril diameters in each cross-section, as well as their mean value for a fibril segment were used for subsequent analysis.

Finally, medians of the resulting height values were extracted for each measured fibril segment. Fibril segment medians in different chemical treatment (PBS-Min0-Min1-Min2-Min3) were noted, as well as sample averages from the medians of all measured samples.

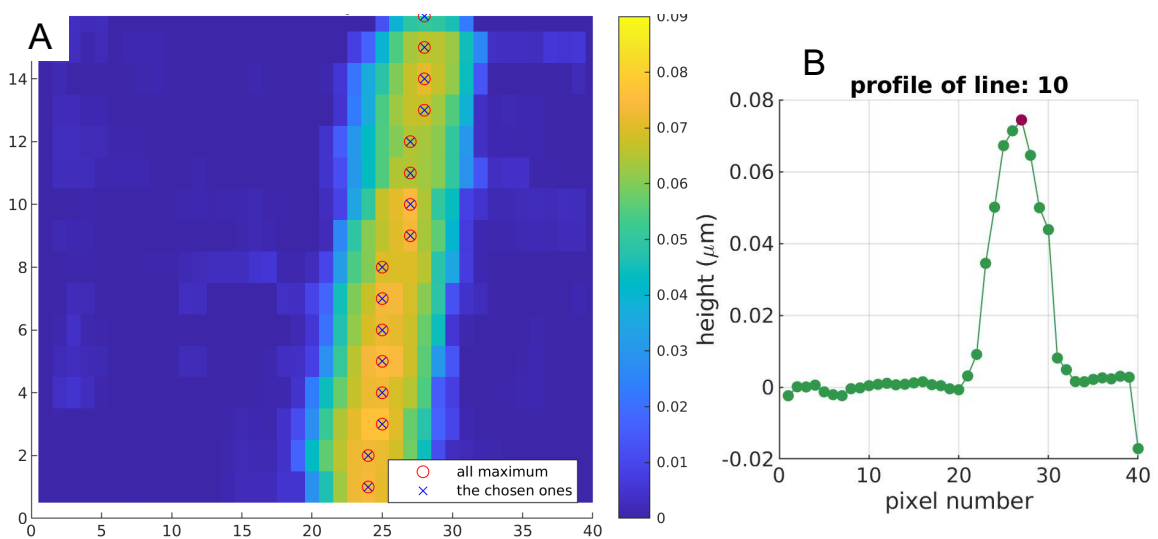


Figure 41: Height image (A) of a fibril, with a corresponding line shape in one cross-section (B)

4.2.2. Indentation modulus

Indentation moduli in each indentation point and their mean for a fibril segment were determined using the MATLAB process developed by DR. ANDRIOTIS. The script extracted the raw D/Z curves of all indentations on a given force-map. The slow scan axis size of force-maps was $2\ \mu\text{m}$, to capture a fibril segment of corresponding length, and the fast axis size varied between $0.6 - 1.0\ \mu\text{m}$, according to the fibril diameter. Accordingly, indentation resolution of the force-maps was 16 longitudinally (slow), and $32 - 40$ in the width (see 3.5).

First, the script analyzed the topography data of the force-map, extracting the Z -displacement coordinate where the approach phase of the indentation ends (contact point, start of indentation) in every indentation point, similarly to the morphology analysis. By scanning the topography data, the fibril was identified based on its cross-sectional shape. In each of the 16 cross-sectional lines along the slow axis, the highest point on the fibril was determined (Figure 41, right, red dot). These 16 indentations were then further used as the applicable indentation points on the given fibril segment, because it was at the largest diameter of the fibril, where the Hertzian and Oliver-Pharr criteria were best met.

The D/Z plots of the 16 indentations were then visually assessed for their integrity and shape. Indentation curves had to match certain criteria to be marked as feasible, resembling the shape of Figure 18: a flat approach and retract phase, sharply distinct from the inclined load-unload phase of the indentation. A distinct contact point must have been able to be identified as the beginning of a firm upward momentum arising from the flat approach phase. Disturbances/oscillations in the curve signaled artifacts resulting from adhesion, surface tension, interference, and wavering of the tip, and corresponding curves must have been excluded from further calculations (Figure 42, A).

The remaining curves were further analyzed: data for the exact indentation depth and the corresponding deflection slopes were processed with the determined reference slope and calibration constants using Equations 9 and 10. Finally, with the help of Equations 4 and 5 and by applying the determined tip contact surface, the contact stiffness and the corresponding indentation modulus was calculated.

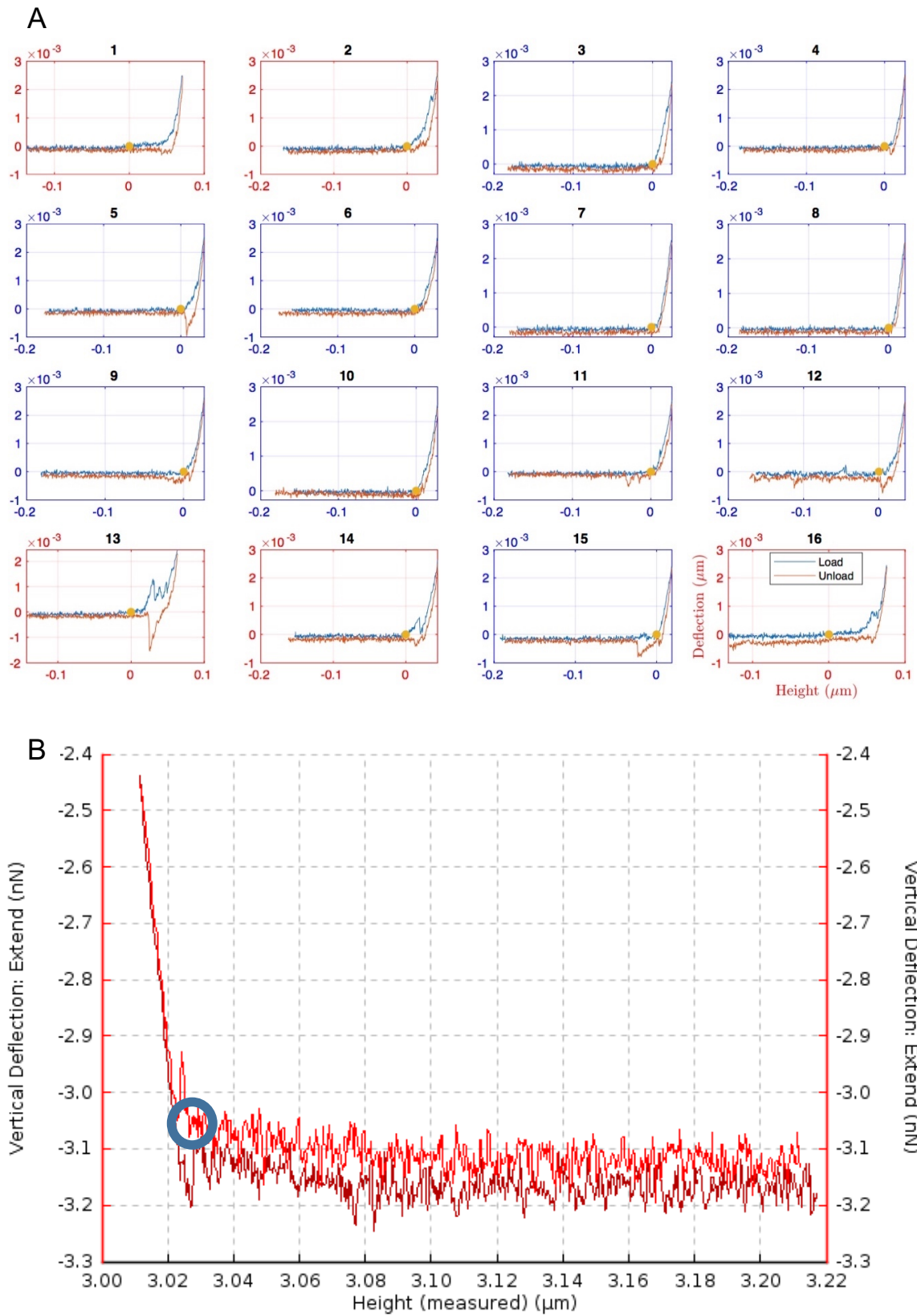


Figure 42: Overview of 16 indentation curves on a fibril segment (A), with excluded curves in red, and an example of a feasible force-displacement plot, with the start of indentation marked (B)

Thereby, the following assumptions were maintained to comply with the Oliver-Pharr indentation models: the deformation during the indentation was elastic-plastic. The indenter was considered as a rigid punch, since the expected indentation modulus of the sample lies in the 10^0 MPa order of magnitude, while in comparison the indenter tip (silicon-nitride) has a Young's modulus of 10^5 MPa order of magnitude. The sample could be considered as an elastic-plastic half-space in which the indentation takes place, because the indenter tip radius (< 5 nm) was at least ten times smaller than the fibril radii (> 50 nm). The sample material was also assumed as homogeneous, isotropic, and linear (no time-dependent behavior). Apart from that, collagen was considered to be transversely isotropic.

Additionally, the raw value of the corrected D/Z slope was registered in every indentation point on the fibril. This served as a measure for the accuracy of the indentation measurement. Indentations with D/Z values out of the $0.2 < D/Z < 0.8$ interval were considered as erroneous [60] and these were excluded from the statistics.

The remaining indentations on each fibril segment were used for statistical analysis. Indentation data was tested for normal distribution (Shapiro-Wilk test, $\alpha = 0.05$) on each fibril segment in every chemical treatment step. Means and variances were built for each measured fibril. After the verification of the distribution, the difference of the fibril means between two neighboring steps was tested by two-sample t-tests ($\alpha = 0.05$).

Additionally, indentation data of all fibrils in a particular steps were pooled, and statistical variables were calculated by the pooled variance method. These were used to compare the average values of a sample in different treatment steps. Comparisons were evaluated by Hedge's G value, using means μ_i , and variances σ_i^2 , where n_i are the number of values in each population.

$$G = \frac{\mu_1 - \mu_2}{\sigma_{12_pooled}} \quad (11)$$

$$\sigma_{12_pooled} = \frac{(n_1 - 1)\sigma_1 + (n_2 - 1)\sigma_2}{(n_1 + n_2 - 2)} \quad (12)$$

5. Results

5.1. Sample preparation

5.1.1. Reconstituted fibril resources

Reconstituted fibrils were prepared based on the protocol (Annex B) developed by BURNS [63]. From 8 samples (R1-R8), samples R5-R8 (1 h settling-time) were used in the experiments as reconstituted samples. These samples provided enough deposits of single fibrils, which were applicable for measurements. R5 was used for the final measurement.

5.1.2. Native fiber dissection

Ten sample slides of native fibrils were prepared (N1-N10), as described in Chapter 3.1.1. Each sample slide contained a smeared fiber of mouse tail tendon, acting as a rich resource of native collagen fibrils. The smearing process could not unbundle and spread out most of the fibril bundles, so that the sample surface primarily consisted of thicker fibril bundles and fiber remains, along with void areas where stacks of unbundled single fibrils were exposed (Figure 43, B). Segments of these single fibrils served as the objects for subsequent AFM measurements. On samples N3 and N4, no suitable group of appropriately exposed single fibrils could be found, therefore these samples were discarded. N5 was used for the final measurement.

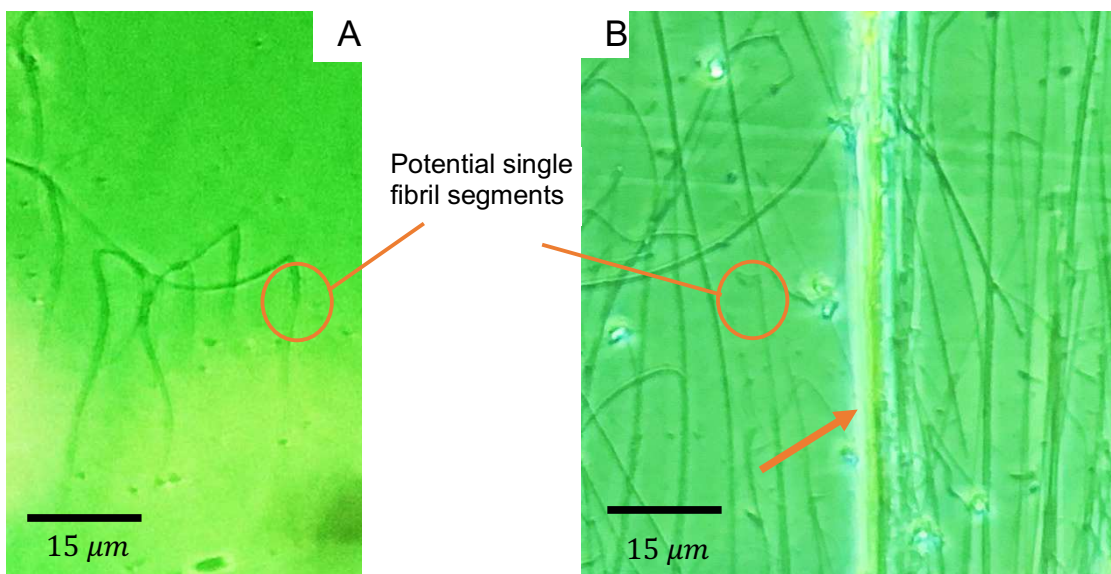


Figure 43: Microscopical images (320x magnification) of collagen fibrils on reconstituted (A) and native (B) samples. A thick fiber bundle (arrow is apparent on B spanning longitudinally in the image).

5.2. Fibril morphology

5.2.1. Comparison of reconstituted and native fibril morphologies

The microscopic observation of reconstituted samples revealed shorter and thinner fibrils than fibrils of the native samples. While the reconstitution process usually resulted in bundling and spiraling fibril groups, with thin and tapered fibril ends, native fibrils were more distinguished and robust (compare Figure 43). For comparability, only single segments were observed.

Height data were obtained from the indentation data of the 16 indentation points per fibril segment (see 4.2.1), for all measured native and reconstituted samples. In both samples R5 and N5, the measurement of 8 of the 9 chosen segments could be completed. To compare the height (diameter) of native and reconstituted samples, the data in the unmodified “PBS” state was used. Table 2 below contains the height data of the measured native (8 segments on sample N5) and reconstituted (8 segments on sample R5) collagen fibrils in PBS. For additional comparison, the native fibril samples from the additional measurements had mean heights of 86 nm (A1), 131 nm (A2), and 155 nm (A3).

Table 2: Median height values (nm) of fibril segments on reconstituted (R5) & native (N5) samples in PBS. Statistical values for all segments per sample are given additionally at the end of the table.

Fibril	1	2	3	4	5	6	7	8	Median	Mean(SD)
R5 [nm]	60	58	48	33	65	36	49	53	51	50 (11)
N5 [nm]	184	123	179	221	237	204	234	117	194	187 (47)

Apart from the mean height difference, native fibrils demonstrated a smoother and more distinguished peak curve measured across their cross-section, than reconstituted fibrils (Figure 44). The height shapes of native fibrils were also more distinct from the substrate than the shapes of the reconstituted fibrils, due to large amounts of chemical residues on the reconstituted sample slides which built a thin film around generated fibrils (Figure 31).

Analyzing the height shapes of reconstituted and native fibrils also confirmed that reconstituted fibrils appear wider than native fibrils, having the same or lower height, probably because of residual collagen and chemical residues surrounding the fibril.

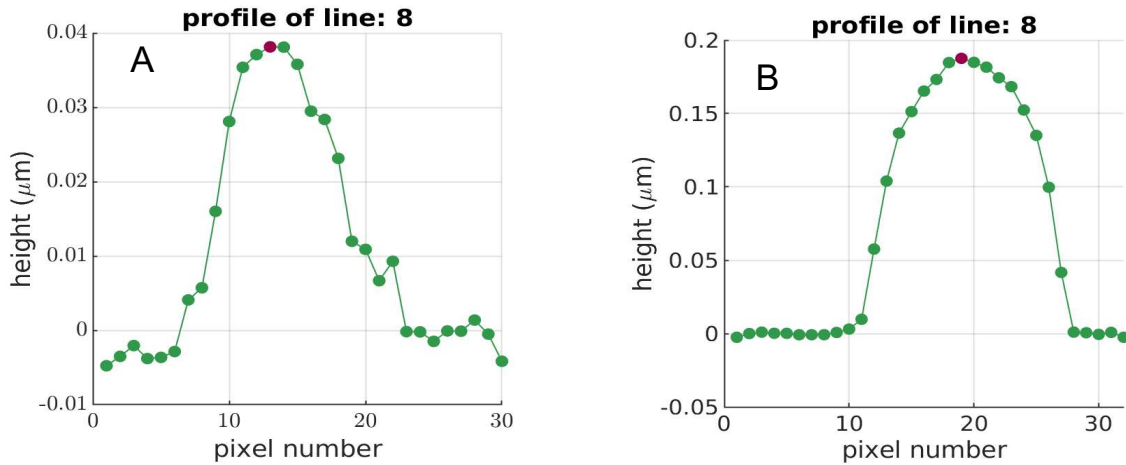


Figure 44: Cross-sectional curves, shaped by the 8th line of indentations of R5 (A) and N5 (B).

The D-banding pattern of native fibrils was found to be more definite as well, in contrast to the D-banding of reconstituted fibrils. D-banding on reconstituted fibrils often appeared in a combination of multiple skewed patterns with the same amplitude, suggesting that even thin (50 nm wet height) reconstituted fibrils might comprise of merged “microfibrils” (Figure 45).

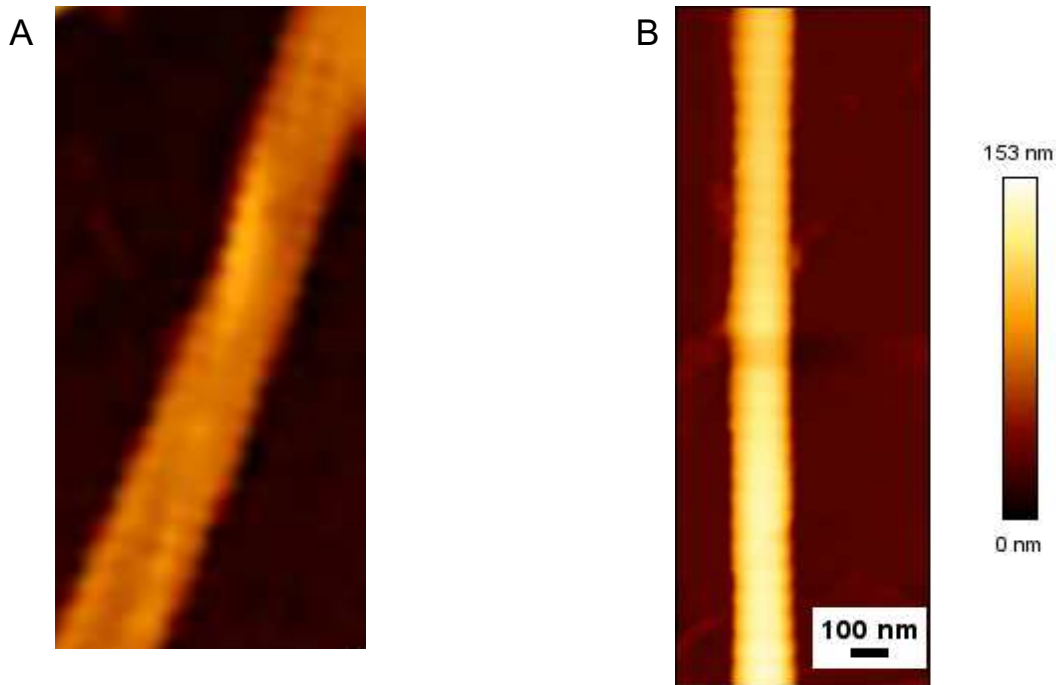


Figure 45: Images (contact mode imaging in air) of a fibril segment on sample R6 (A) and N6 (B). The scales on the right refer to both images. While the D-banding of the native fibril appears solid and definite, the reconstituted segment demonstrates a staggered pattern of multiple D-banding series, especially in the upper half of the imaged segment, due to overlapping multiple microfibrils.

5.2.2. Fibril swelling behavior

The morphological properties of the measured collagen fibrils were assessed in every step along with the mechanical examination. That is, the thickness (diameter) of a measured fibril segment was quantified as the height of the fibril with respect to the substrate surface.

The height values of a force-map were analyzed as described in 4.2.1. Height data was sourced from topography images made by contact mode imaging in ambient air, and from the indentation force-maps in PBS environment in steps PBS, Min0, Min1, Min2, and Min3 (see Figure 37). The primary focus was on the comparison of diameters in air and PBS environment. Both native (N5) and reconstituted (R5) fibrils demonstrated a similar swelling phenomenon between the two steps, with a $1.5 \times$ average increase in fibril height.

As elaborated in 3.4.6, the duration, for which the fibrils were immersed in the PBS solution after the first examination step in air, was crucial with regard to how the swelling phenomenon came to its climax. Based on multiple tryout sessions, it was apparent that the swelling effect takes time to saturate, as insufficient conditioning time resulted in subsequent swelling and eventual softening of the mechanical stiffness (3.4.6). Therefore, a 48 *hour* conditioning time was added to the final protocol (Figure 37). This proved to be a sufficient time for the full diameter change, as the diameter growth was already neglectable throughout the subsequent steps (Figure 46). This observation was also underlined by the comparison of samples A2 and A3 between the PBS and the mineralization step (5.3.6).

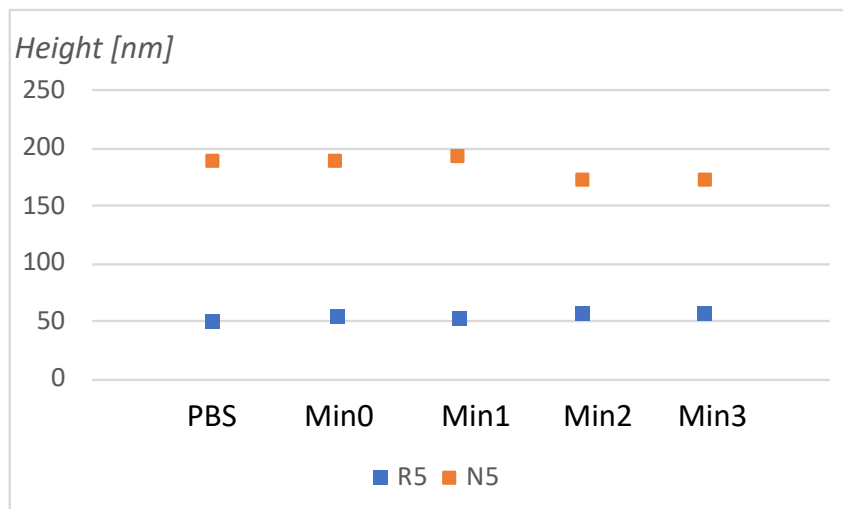


Figure 46: Median height (QI) of the fibril segments of samples R5 & N5 across the experiment steps, illustrating the effect of a 48h pre-conditioning: the diameter change of the fibrils was neglectable.

5.2.2.1. D-banding appearance

It was observed, that along with the swelling phenomenon between the ambient “air” and “PBS” state, the captured surface morphology of the fibrils changed as well. High-resolution images in air showed distinct and clean gap-overlap patterns of D-periodicity of a fibril segment, with an approximate measured period of 67 nm and a depth of 2 – 3 nm (Figure 47, A & C).

High-resolution QI images in PBS revealed less pure topographies of fibril surfaces with an apparent roughness of a higher frequency, while the depth and periodicity of the original D-banding was still observable (Figure 47, B & D).

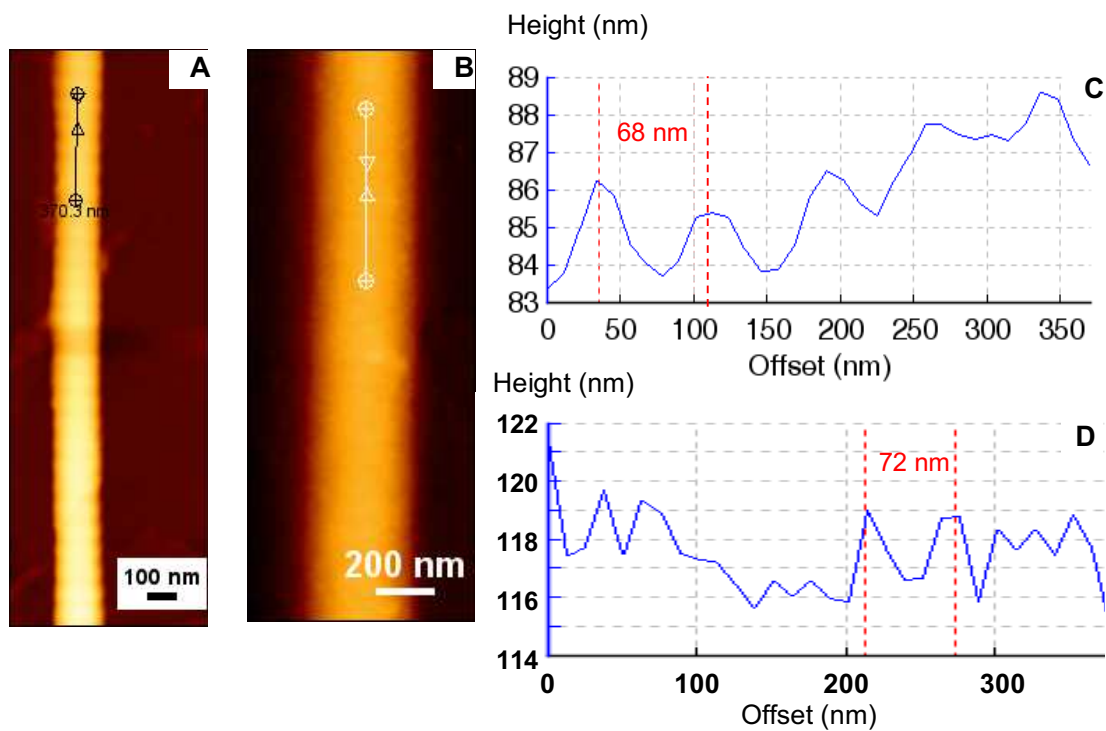


Figure 47: Images and topographic lines of fibril segment 1 of the native sample A3. A - imaging in contact mode in air. B – QI image (64x170 px) of the same fibril segment in swelled state in PBS. C - Plot of the surface topography as height data along the marked trajectory on A. D - Plot of the surface topography height data along the marked trajectory on B. Measured D-banding (red) on C and D.

5.2.3. Morphology of mineralized fibrils

5.2.3.1. Morphology in control mineralization (Min0)

The QI images and topography surface plots of fibril segments in the Min0 state did not show visible differences in contrast to the PBS state. Subsequent swelling behavior was neglectable in both N5 and R5 samples (see Figure 46) due to the sufficient pre-conditioning in PBS before measuring these. Outcomes of the complementary A1 experiment, focusing on the two steps PBS and Min0, very well illustrated the height indifference (Figure 48).

Considering the contamination of the sample area in general, no changes were observed comparing the PBS and Min0 steps (Figure 49). The contamination level remained low. Large crystals might have precipitated during the Min0 step due to the absence of fetuin, but they were not adhered to fibrils and they were apparently successfully rinsed before measurement.

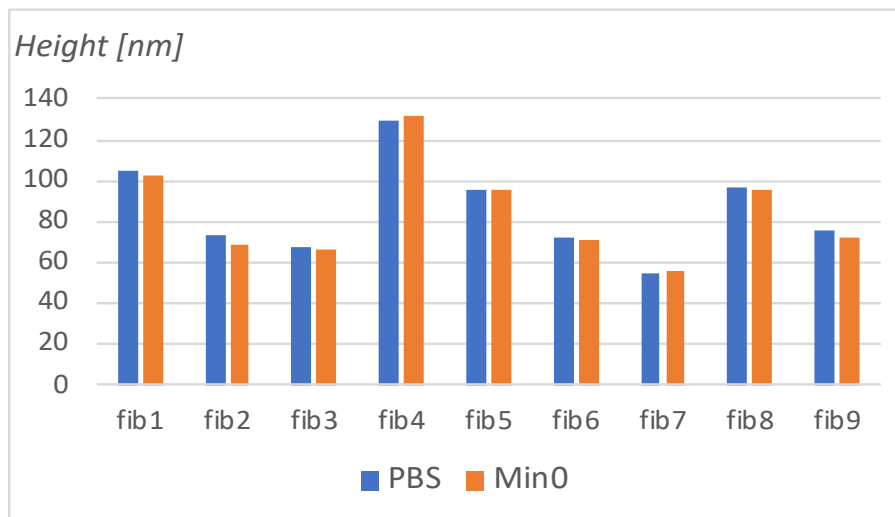


Figure 48: Heights of the 9 fibril segments in sample A1 in the PBS and Min0 steps. Height values are yielded as the median (to avoid outlier effects) of the 16 indentation height values on the fibril ridge.

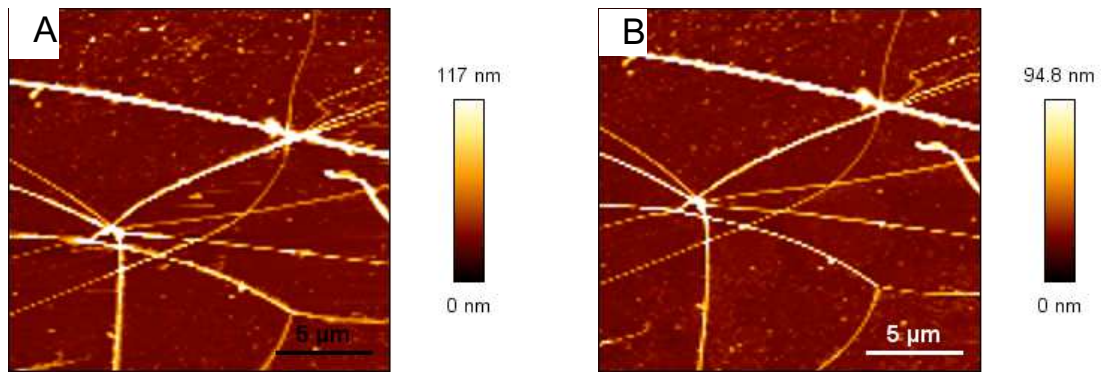


Figure 49: Sample area of A1 in the PBS (A) and in the Min0 (B) state (Imaging, 128x128 px).

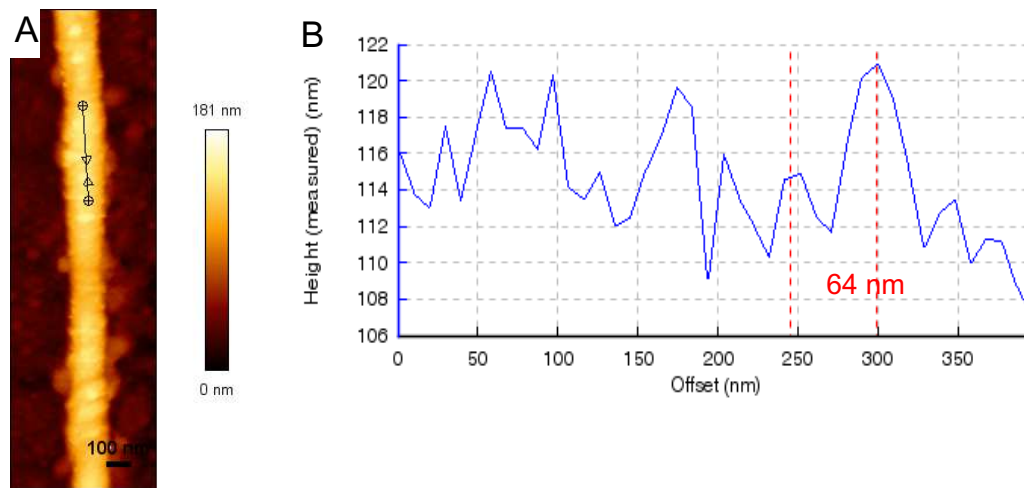


Figure 50: QI image of 64x170 px size (A) and height plot (B) of the marked surface trajectory of fibril segment 1 of the native sample A1 in the Min0 state. D-banding marked in red.

Table 3: Median height values (nm) of fibril segments on A1-A3 in their PBS and modified states.

Statistical values for all segments per sample are given additionally at the end of the table.

Segments 7-9 on A3 in Min1_EDTA could not be measured because of sample dryness.

Segment	1	2	3	4	5	6	7	8	9	Median	Mean(SD)
A1 PBS	105	73	67	129	96	72	55	97	76	76	86 (23)
A1 Min0	103	69	66	132	96	71	56	95	72	72	84 (24)
A2 PBS	88	131	147	122	117	167	162	180	217	147	148 (39)
A2 Min1_EDTA	94	134	170	158	125	172	155	184	223	158	157 (37)
A3 PBS	139	183	136	67	136	119	130	86	187	136	131 (39)
A3 Min1_EDTA	136	188	139	70	153	135	-	-	-	138	137 (38)

The topography of the fibrils, especially the appearance of the D-banding pattern did not show any remarkable difference to the PBS state (Figure 50, B): D-banding and impurities appear with similar heights and amplitudes (compare with Figure 47, D).

5.2.3.2. Morphology in mineralization

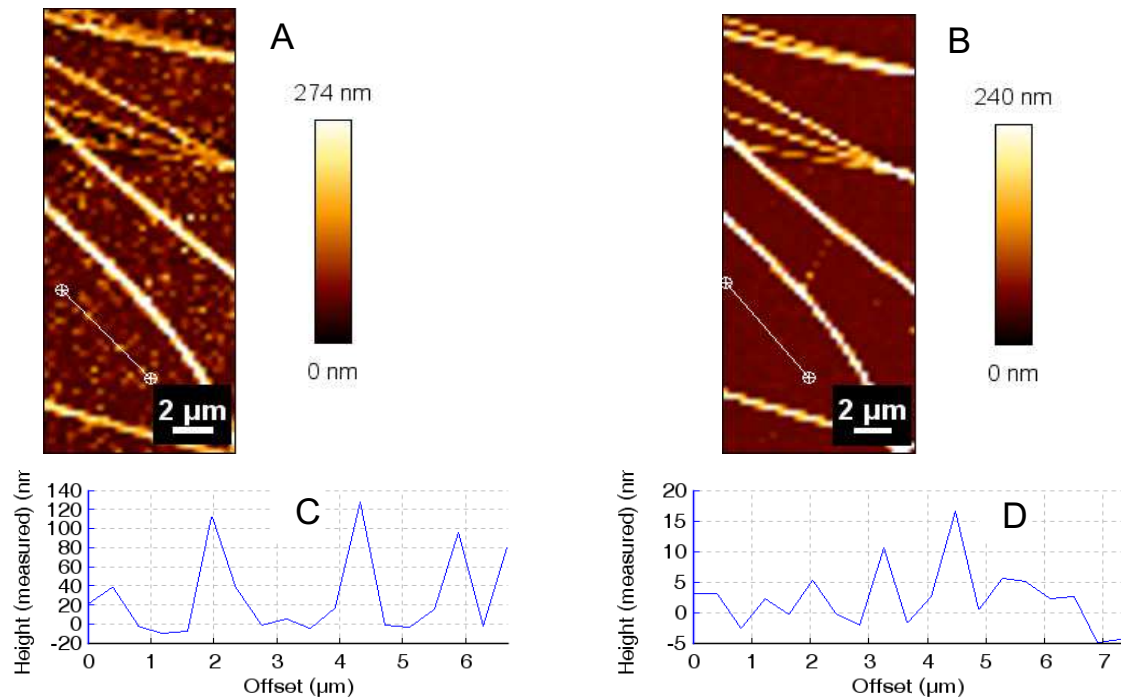


Figure 51: QI images (350x128 px) of the sample area of A3, in the Min1 (A), and Min1_EDTA (B) state. Below each image, the height [nm] plot of the same cross section is shown (C,D).

In contrast to the Min0 modification, sample areas as well as fibril surfaces tended to contaminate strongly during the mineralization steps. As an example, the sample A3, undergoing a measurement in PBS and a subsequent measurement after one mineralization step (Min1), was disturbed by large precipitations in Min1. The sample area, as well as the fibrils themselves, was covered by deposits of up to 120 nm size. These could be removed after an EDTA rinse (Min1_EDTA), as illustrated in Figure 51.

The excessive crystallization affected the topography of fibril segments as well. In case of sample A3, large crystal platelets were observed after mineralization (Min1), inserted in and probably sticking out of the surface of the fibril. The example of sample N5 in its Min1 state showed similar phenomena, and thus confirmed that crystals embedded into the fibrils in the mineralization step. Crystalline features on fibril surfaces appeared at 20 nm – 40 nm height above the fibril surface, as illustrated in Figure 52. Similar to A3, the sample area of N5 was contaminated as well. After the EDTA rinse (Min1_EDTA), fibril surface roughness was still present to a larger extent than in the original PBS state (Figure 53, G-H), but the median height was not remarkably different (Table 3, A2 & A3 in PBS and Min1_EDTA state).

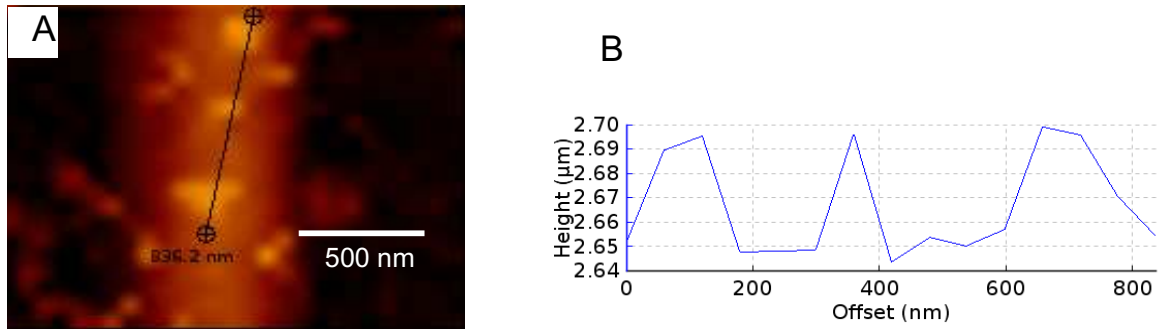


Figure 52: QI (64x24 px) of fibril 7 of sample N5 in Min1 (left), with the height plot of a surface trajectory (right).

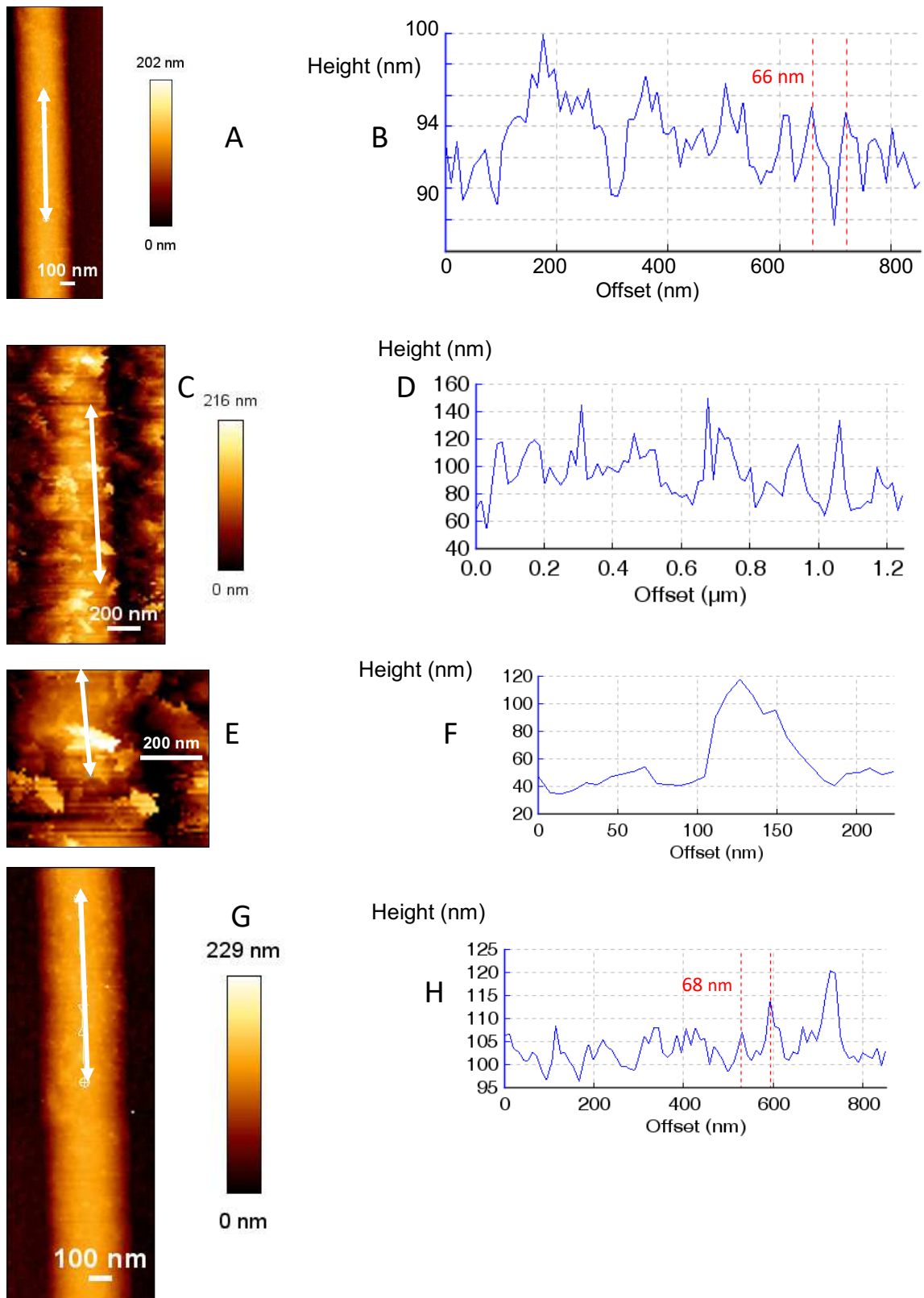


Figure 53: QI (64x170 px) images of fibril segment 5 of sample A3 in 3 stages, with corresponding height plots of a surface trajectory (double-arrow): A,B – in PBS (D-banding marked red). C,D – after Min1. E,F – 2X zoom of a segment after Min1. G,H – After Min1_EDTA (D-banding marked red)

5.3. Mechanical properties

5.3.1. Comparison of unmodified reconstituted and native fibrils

Both samples R5 and N5 were indented in their unmineralized state, in stage “PBS” (Figure 37). Nine $2\ \mu\text{m}$ long fibril segments were measured on each sample, with 16 indentations each. In general, 5-10 indentations could be included in the calculations per segment. The mean moduli E for each fibril segment per sample are collected in Table 4. In case of N5, 5 fibril segments were excluded (“Excl.”) from the calculations, due to unfeasible or faulty indentations (DZ slope out of bounds). For R5, 2 fibril segments were excluded (“Excl.”) for above reasons. The overall pooled averages were in the same range for R5 (2.52 MPa) and N5 (2.20 MPa).

Table 4: Mean indentation moduli (MPa) for each fibril segment on samples R5 and N5 in the PBS step. Statistical values for all segments per sample are given additionally at the end of the table.

Segment	1	2	3	4	5	6	7	8	9	Median	Mean(SD)
R5 [MPa]	3.10	Excl	2.06	2.99	Excl	1.68	3.2	2.32	2.28	2.32	2.52 (0.58)
N5 [MPa]	2.15	1.00	1.30	Excl	Excl	4.40	Excl	Excl	Excl	1.73	2.20 (1.54)

5.3.2. The effect of mineralization

In the Min1 step, crystallization inside and on the surface caused artifacts for many indentations on various fibril segments. It was apparent that after mineralization, faulty indentations increase, and large variances appeared due to crystal inserts on fibrils, as described in 3.4.3. In the Min1 contaminated state, some extremely high indentation moduli occurred on the samples, in the 100 MPa order of magnitude. These were excluded due to D/Z-slope inaccuracy.

Additionally, the sites of each indent on a fibril segment were visually analyzed, to be able to find the reason for the stiff indents, but no correlation could be observed between height (crystallization topography on fibril) and the artifacts. That is, it was not necessarily the highest point on the fibril (an assumed crystal) which had a high stiffness. This phenomenon will be discussed in 6.2.2.

5.3.3. Reconstituted fibrils (R5) in different mineralization stages

The average of the pooled data of seven fibril segments of sample R5 were compared from step PBS to Min3 (Figure 54 A). No EDTA were used in any stage. In an overall view, the indentation modulus shows a continuous decline, probably due to softening effects. However, the moduli remain in the 1 – 2 MPa range. The overall sample behavior is underlined in detail on Figure 54-B by the behavior of individual fibrils. Two-sample t-tests for the difference between treatment steps only revealed significance between Min0 & Min1 for 1, and between Min1 & Min2 for 2 out of 7 fibrils. Thus, the overall behavior is not to be considered significant.

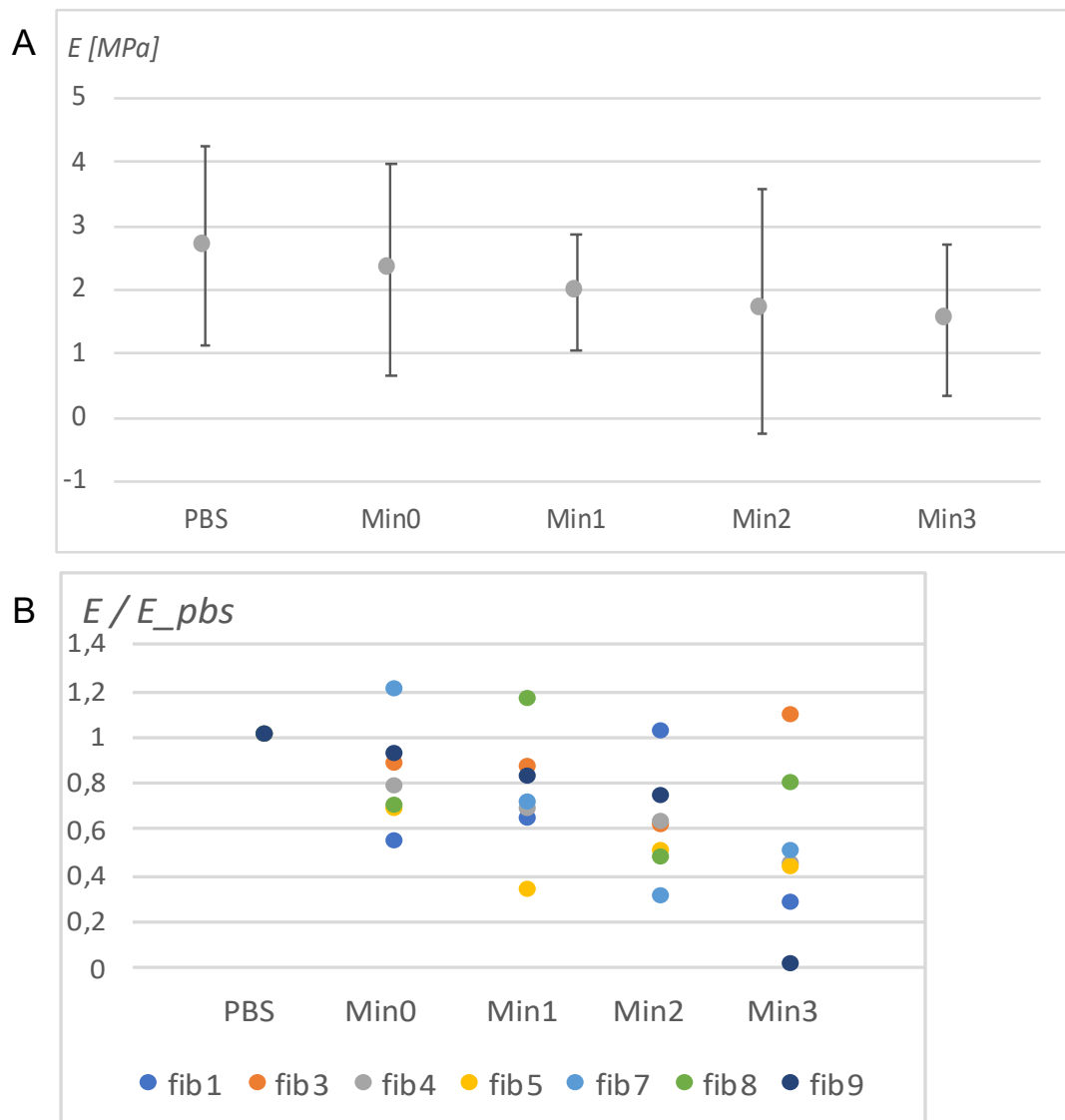


Figure 54: Mean indentation moduli in each step for sample R5;

A – pooled over 7 fibril segments, with standard deviations

B – focusing at the change of each individual fibril, normalized to the PBS values

5.3.4. Native fibril (N5) in different mineralization stages

The measurements of three fibril segments on N5 were feasible to be included in the calculations in every step. The pooled data was analyzed and compared across the measurement session, from stage PBS to Min3 (Figure 55).

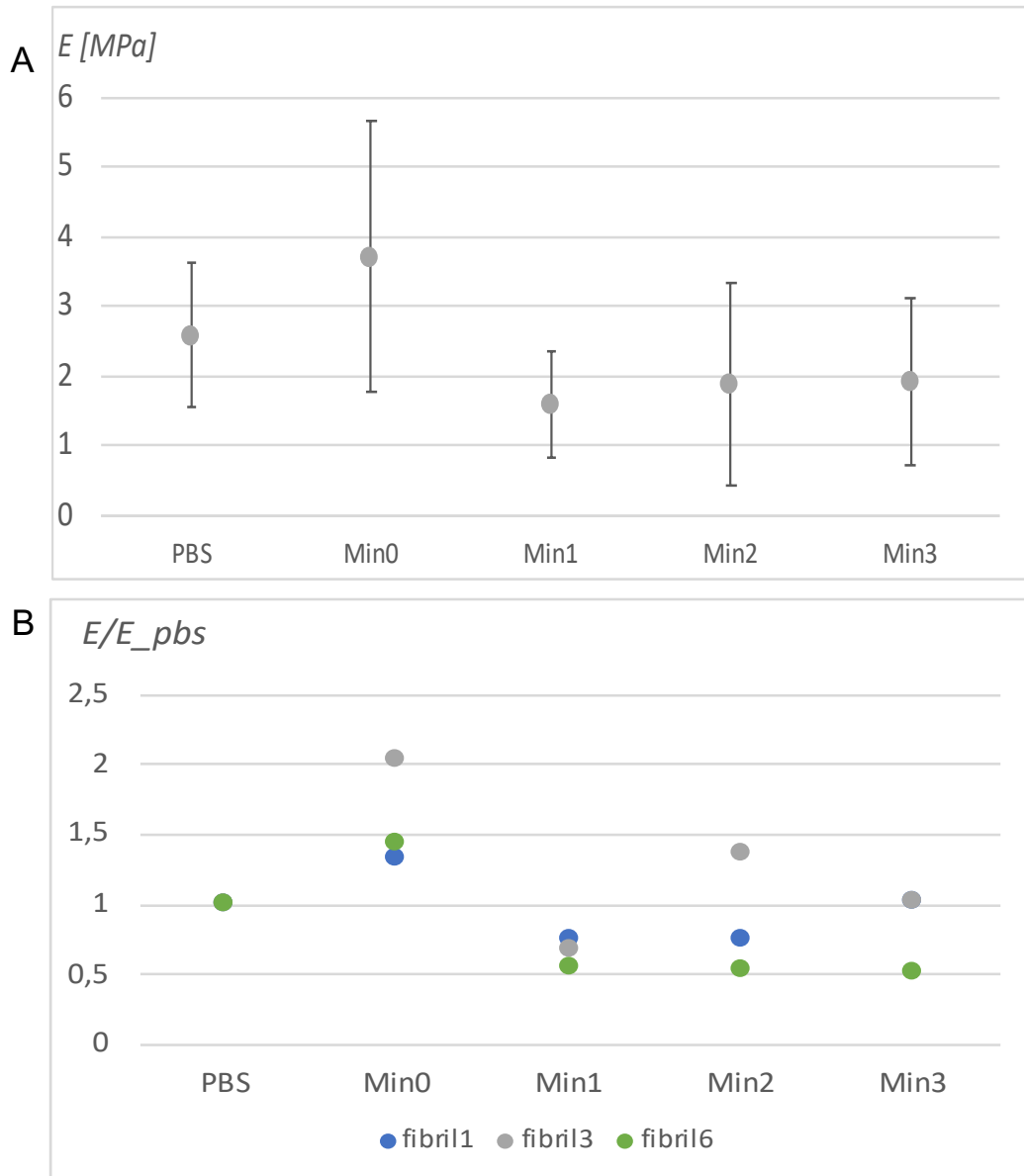


Figure 55: Mean indentation moduli in each step for sample N5;

A – pooled over the 3 fibril segments, with standard deviations

B – focusing at the change of each individual fibril, normalized to the respective PBS values

The developments of the individual fibrils were assessed by two-sample t-tests between neighboring steps (Figure 55, B). All three fibril moduli demonstrated a significant peak throughout PBS-Min0-Min1. No significance is revealed for the changes of moduli afterwards.

The peak in Min0 is probably due to large crystal deposits on the fibril segments. EDTA were used before measurement in the Min1 and Min3 stages, due to excess crystallization on the fibrils. Indentation moduli decline from Min0 to Min1 significantly, probably induced by the EDTA treatment. In contrast, EDTA use in the Min3 step did not cause a similar decrease, but might have inhibited the growth of *E*. That is, the average pooled indentation modulus (Figure 55, A) increased by 18% from Min1 to Min2, and only 2% from Min2 to Min3. Additionally, it is apparent, that in the steps where EDTA rinse was applied, the variance of the data shrinks.

5.3.5. The effect of the Min0 step (A1)

The influence of the Min0 step was further examined by the conduction of the additional experiment A1 on a native fibril sample, which underwent the control mineralization step only. In this case, a more refined rinsing after Min0 was already employed, unlike in the case of N5.

In the case of A1, no crystallization and no contamination was observed after the Min0 treatment (Table 5). Regarding the mean indentation moduli of the fibril segments, the two-sample t-tests did not reveal any significant difference for any fibril between PBS and Min0.

Table 5: Mean indentation moduli (MPa) for each fibril on sample A1 in PBS and Min0
Statistical values for all fibril segments per sample are given at the end of the table.

Segment	1	2	3	4	5	6	7	8	9	Median	Mean (SD)
A1 PBS	10.0	4.93	4.67	4.63	4.83	6.53	2.79	3.28	3.99	4.67	5.14 (2.13)
A1 Min0	8.20	4.46	4.60	4.54	4.27	5.91	2.42	3.57	4.88	4.54	4.73 (1.60)

5.3.6. The effect of the preconditioning (A2-A3)

Due to strong contaminations after the Min1 treatment, measurements had to be intervened in case of both samples. On sample A2, fibril segments 1-6 could be measured, on A3 segments 1-5. The performed indentations in Min1 yielded data with frequent outliers, due to a lot of extremely stiff indents (impacting a crystal).

After EDTA rinse, the samples were measured again (Min1_EDTA), whereas all fibril segments could be successfully examined already. For the evaluation, the Min1_EDTA measurements of both samples were used.

In case of sample A3, fibril segments 7-9 were excluded from the calculations due to an accidental drying during the Min1_EDTA measurement. Therefore, only fibrils 1-6 were drawn for comparison. In case of A2, all fibrils could be measured, but subsequently captured accuracy errors left 4 fibril segments to analyze.

While all other parameters of the experiment session being identical, the pre-conditioning time of A3 was set to 2 *hours* only, in contrast to 48 *hours* for A2. As a result, a larger (−27%) softening effect was observed for A3 in the subsequent Min1 step, than for A2 (−12%, Figure 56 A&B). T-tests for the mean indentation modulus of individual fibrils between PBS & Min1 resulted in significant ($\alpha = 0.05$) difference for 3 out of 9 fibrils in A2, and 5 out of 6 fibrils in A3 (Figure 56 C&D).

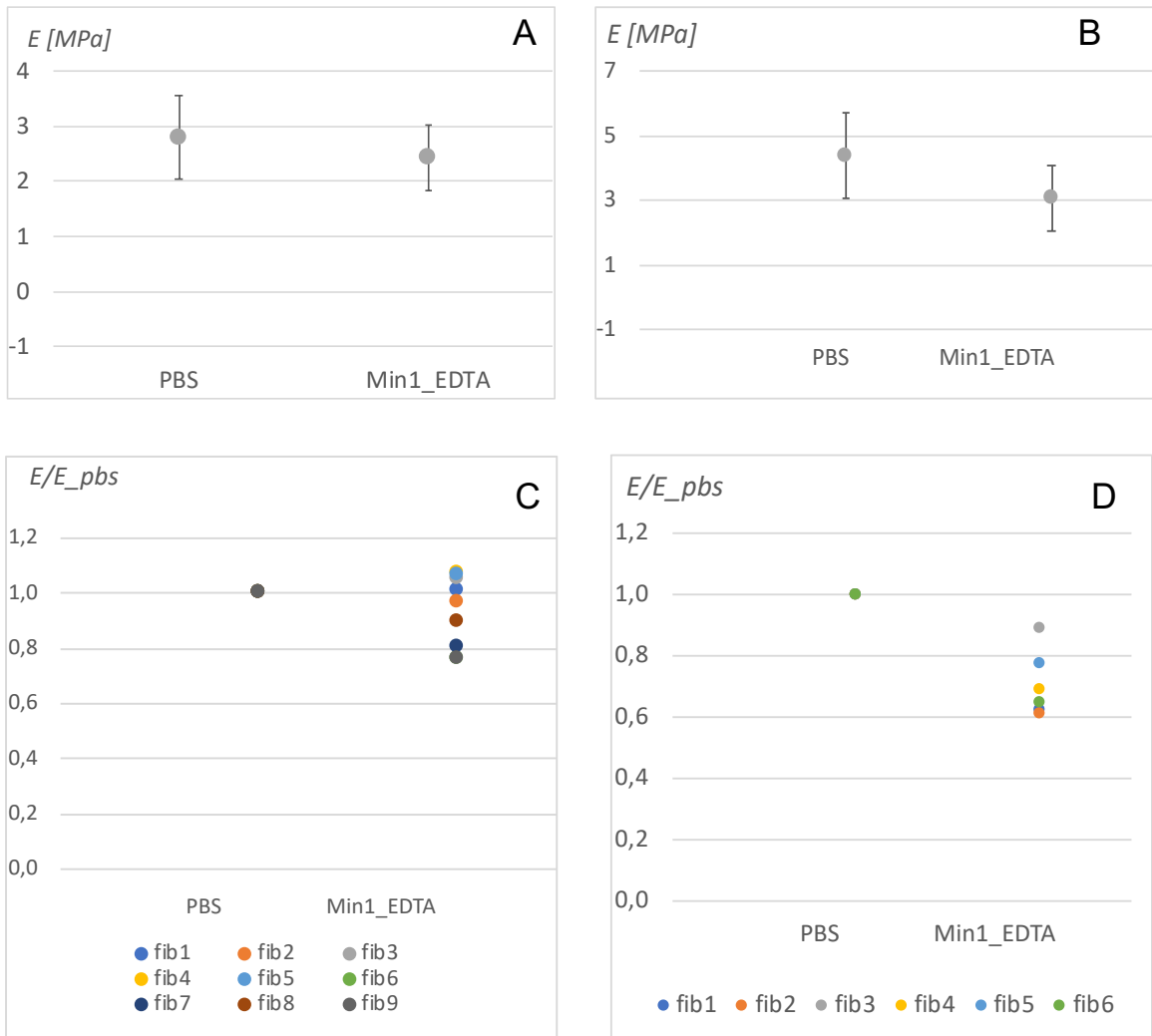


Figure 56: A & B: Average indentation modulus and standard deviation of each treatment step of samples A2 (A) and A3 (B), calculated by the pooled variance method. Hedge's G test yielded a decrease by 0.74x standard deviations for A2, and by 1.2x for A3.

C & D – Mean indentation moduli on individual fibrils in each step on samples A2 (C) and A3 (D). Values are normalized to the value in PBS for each sample, to focus on the variation between 2 steps.

6. Discussion

The primary aim of this thesis was the testing of collagen fibril samples from different sources, modified by an established methodology. Many planned experimental steps could not be properly achieved, though, and needed interim redesign. Hence, the experimental activity evolved into a work, which to a large part consisted of the development and testing of the methodology itself. Thus, important observations arose regarding the applicability of AFM nanoindentation and imaging in different environments, as well as the behavior of differently sourced collagen fibril samples throughout the specific chemical modifications. The time- and workframe of the master thesis did not allow for further development of the methods.

6.1. Interpreting the results

In contrast to the planned outcomes, reconstituted and native samples could not be compared to each other in this study. Similarly, no significant difference was detected regarding the indentation modulus of the unmineralized (PBS) and mineralized (Min3) state of any sample.

However, the obtained indentation moduli data is still applicable for the comparison of fibril behavior of individual samples after different chemical treatment steps. Apart from that, the different methodological acts can be assessed with respect to their individual influence.

6.1.1. Assessment of the morphology

Reconstituted fibrils often demonstrated an irregular cross section and surface topography in their unmodified state, compared to native fibrils, as illustrated on Figure 10 and described in 5.2.1. This phenomenon was also observed by SILVER et al. [31], and it was underlined by the fact that the raw height data on a reconstituted fibril segment showed a greater variance compared to a native fibril segment. Additionally, the mechanical stiffness showed a larger variation on individual reconstituted fibrils than on native fibrils: the indentation moduli of the reconstituted fibrils on R5 had larger standard deviations relatively to their means, than the fibrils on the native sample N5, suggesting that the stiffness and/or the cross section of the tropocollagen-assembly of reconstituted fibrils is irregular. The presence of microfibril-like structures (Figure 45 A) in the reconstituted fibril structure may also imply that the *in vitro* generation can lead to irregular morphologies. Consequently, an *in vitro* reconstitution process might not provide even and homogenous fibril structures.

On the other hand, it is apparent that the variance among individual fibrils is lower in the reconstituted sample than in the native sample: the ratio of the standard deviation to the sample average is 21% for R5, while 25-30% for N5 and A1-3 (compare Tables 2 and 3). This suggests, that in spite of an irregular structure per fibril, the overall fibril thickness in a reconstituted sample is more uniform. Native samples often contain fibrils of different thicknesses: *ex vivo* tissue samples show a greater variety. Consequently, an *in vitro* reconstituted sample proves to be applicable when a sample of rather consistent morphology is required, that is, when the same kind of measurements are to be conducted on a large amount of fibrils of one sample.

As described in 5.2.2.1, D-banding of both native and reconstituted samples appeared clean and distinct on images made in air. On average, the gap-overlap profile of D-banding appears with a 3 – 4 nm depth, whereas 6 nm was reported in literature [48]. On PBS images (first measurement stage after pre-conditioning), the clean pattern diminished under the influence of higher-frequency topography features, but could be still determined on topography plots. The disturbance might be caused by substances precipitating from the PBS solution and embedding into or onto the fibril structure. After mineralization, the D-banding pattern was not observable anymore: either it was covered by the large-scale crystallization on the fibril (Figure 52), or disturbed by the residual nanoscale precipitations (Figure 53 G-H) after the use of EDTA.

6.1.2. Effect of hydration

After the evaluation of the tryout measurement sessions, the outcomes regarding the mechanical stiffness were far from the expected. The indentation modulus did not increase throughout the first 3 (PBS/Min0/Min1) steps; on the contrary, it decreased. This was supposedly correlated with the long time (total of 2 days) exposure to a tempered fluidic environment with high ionic content. Both native and reconstituted fibrils demonstrated a swelling behavior under fluidic conditions, which primarily took place rapidly after changing the environment. An additional 5-10% diameter growth was observed in the long term in the course of 1-2 days. Along with that, a decrease of indentation moduli took place. The two phenomena were supposed to be correlated: due to the infiltration of water molecules in between collagen molecules, the inner fibril structure softens [58].

The observed swelling ($1.5 \times$ PBS/air) and softening behavior of both native and reconstituted fibrils, described in 5.2.2, was an expected phenomenon based on [22], [23], [45], [47].

However, in contrast to the rapid morphological change, the mechanical softening effect of the hydration occurred in a longer period. While the swelling phenomenon during measurements could be cancelled by even 2h of pre-conditioning (Table 3), the subsequent mechanical softening occurred also after 48h of pre-conditioning (Figure 56 – A). This is well underlined by the behavior of R5 through the measurement cycle: the morphological change across the steps is neglectable (Figure 46), in contrast to the continuous decline of the indentation modulus Figure 54. Still, as proven by the experiments A2 and A3, a sufficient pre-conditioning in fluidic environment (PBS) does partly suppress the subsequent softening (5.3.6 & Figure 46).

The softening effect could also occur due to a limited thermal stability of the collagen used. Depending on the hydroxyproline content of the molecules, which is affected by the tissue from which the collagen monomer is sourced, tropocollagen coils might have limited thermal stability at 37°C [79], [80]. This phenomenon could also co-affect the softening behavior. This is underlined by the study of BALDWIN et al., who observed a significant decrease of stiffness after exposing collagen fibrils to 50 °C for a short period (30 min). The fibrils presented in this thesis were exposed to a lower temperature, but for essentially longer periods (up to 120 hours).

6.1.3. Assessment of mechanical properties

The average indentation modulus of the unmineralized N5 and R5 samples lie in the same range (5.3.1), whereby the native sample average is about 10% lower compared to R5. The reason for the difference can be the naturally occurring stiffness variation (~20%), or the pre-conditioning of N5. Due to the different sample sizes, no tests were conducted for significance. The similarity between R5 and N5 implies that a reconstituted sample could theoretically well resemble the properties of a native sample.

Generally, average indentation modulus results for unmineralized fibrils are consistent with values in previous studies in the range of 2 – 5 MPa [21], [24], [45], [46].

Regarding the softening behavior during subsequent treatments, FIELDER et al. found that the hydration effect depends on the mineral content [47]. The softening behavior of A3 (Figure 56 – B) and R5 (Figure 54 – A), between PBS and Min1 is similar to the rate of decline for a fibril with 0 wt% mineral content in the study of FIELDER et al. Thereafter, the rate of stiffness

decrease in R5 throughout Min1-Min3 is smaller, similarly to the stiffness decline for a 20 wt% mineralized fibril in the molecular model in [47]. This suggests that the applied mineralization method in the present study had an increasing effect on the stiffness of the fibril. In sample N5 (Figure 55), where the hydration process was more saturated because of 48h preconditioning, the mineralization already induced a slight increase in the indentation modulus Min1-Min3. However, this increase remains insignificant, but indicates that clearer results may be obtained in future studies with larger sample sizes and improved methodology.

The absence of important NCPs, especially in case of the reconstituted sample, might inhibit a proper stiffening effect upon mineralization. Using samples of formerly demineralized fibrils might yield better results as suggested by NUDELMAN et al. [34].

The peak at Min0 on sample N5 actually represents the effect that was expected by mineralization steps, but not by the control mineralization step (5.3.4). The reason for the large increase could lie in nano-size precipitation on the fibril, which could not be cleaned off properly by rinsing with distilled water. It is shown by the later additional experiment A1, with improved rinsing, that no significant stiffness increase takes place at a Min0 treatment (5.3.5).

6.2. Methodology

Until the final measurement protocol was developed, several preliminary trial measurements had been conducted, during which the methodology was continuously improved. Procedural errors were eliminated step by step, so that in the end a successful experimental session could be conducted both for native and reconstituted fibril samples.

6.2.1. Control mineralization

The mineralization steps were supposed to promote mineral growth in the gap regions of collagen fibrils, thereby inducing actual change in mechanical properties which would be observed by AFM nanoindentation (see Figure 37 in chapter 3.5). Fetuin was added to the treatment solution in these steps, which limits the growth of crystals in size, thereby promoting infiltration of minerals in the 40 nm gap zones.

The control mineralization step, in contrast, applied a chemical treatment of the same conditions as mineralization, except for the presence of fetuin. It was intended to prohibit the inclusion of crystals into the fibril gap zones by allowing crystals to grow large with the exclusion of fetuin from the solution. Thus, actual mineralization should not have taken place, and thereby solely the effects of the tempered ionic fluidic environment was planned to be assessed.

Thus, it was planned to capture the tempering effect of the ionic solution on the fibrils. Any change which would be then caused by actual mineralization could be distinctly assigned to the mineralization process enabled by fetuin, and the general effects of ionic and thermal treatment could be excluded. However, the outcomes of the experiments N5 and R5 do not allow for such a comparison, because the differences between a Min0 and Min1 state was suppressed by the softening behavior (R5) and surface crystallization (N5 - Min0).

It is apparent from the comparison of the additional measurements A1 and A2, that the Min0 solution did not have any significant effect on the fibrils compared to mineralization when properly rinsed with DW after treatment. Any possible effect was suppressed by the slightest softening behavior of the fibrils in this stage of the measurement sessions. As it reads from the resulting indentation moduli data, A1 and A2 (both having the same pre-conditioning times) undergo the same extent (E decline of -10%) of softening (Table 5, and Figure 56 - A&C).

6.2.2. Contaminations

As described in 3.4.3, contaminations prohibited proper measurements on certain fibril segments. The immersion of a cool sample slide in a pre-heated solution could be considered as the cause for the precipitations on the slide, but precipitations also occurred in early stages of the methodology development where the solution was not pre-heated yet.

In the Min0 step of N5, the observed peak in E is due to the presence of large hard crystals in multiple indentation points. In contrast, this did not occur in case of R5 or A1. The possible reason is that the improved post-Min0 rinse (with DW) was not yet applied for N5. Regarding the precipitation of smaller crystals after mineralization treatment steps, which occurring in all samples, the additional EDTA-rinse proved to be an appropriate solution. During the final experiments R5, A1, A2, A3, EDTA had to be used rarely, only in cases where contaminations prevented a proper measurement. In case of N5 it was used twice, after Min1 and Min3.

It is considerable that EDTA rinsing might have also partly cleared off intrafibrillar mineralization, so that it might have counteracted the stiffening effect of mineralization, suppressing the enhancement of E-modules. For instance, in case of N5, it is apparent on Figure 55, that in contrast to the average E increase from step Min1 to Min2, there is no apparent average increase from Min2 to Min3. Increases of individual fibrils remain insignificant.

Furthermore, the crystallization in mineralization steps, which appeared problematic and affected the methodology, is probably the result of the desired regular mineralization of the fibrils. For instance, the close-up image of a fibril segment in Figure 52 resembles a regular mineralized fibril as illustrated on Figure 11. The disturbing effect of these ordinary mineral features can be avoided by using tensile tests in future studies instead of nanoindentation.

6.2.3. Adhesion of native fibril samples

The detachment of native fibril samples from the substrate slide was a recurring phenomenon after the second mineralization process, before the improvement of the methodology (3.4.1). By the Min2 stage of a measurement session, the fibrils were tempered in PBS for 20 hours, in the control mineralization buffer for 20 hours, and in the mineralization solution twice for 20 hours. After 80 hours in an ionic fluidic environment, native fibrils and fascicles came off the substrate and dislocated. The originally defined sample segments could not be found any more, either because of being covered by large fiber bands or because they detached and dislocated themselves. The native samples were deposited on PLL substrate slides, instead of regular glass slides, in the further course of experiments.

6.2.4. Appropriate substrate for reference slope and sensitivity calibration

As described in Chapter 3.3.4, the measurement of the reference slopes and the sensitivity calibration required a plain solid surface area, where multiple indentations could take place in close proximity to each other with the same surface hardness and roughness properties.

Based on conventional indentation protocols, it had been practicable to carry out the sensitivity calibration on the sample slide close to the fibrils, in the same environment in which the measurements would have taken place. For this purpose, a clean sample area was generally used, with an infinite hardness and stiffness assumed.

Along with that, the reference slope was to be captured, from the same force map data which contained the fibril indentations. Thereby, the size of the force map area had been chosen accordingly to capture a width which contained not only measurements on the fibril, but also plain sample slide area on both sides of the fibril. Thereby the reference slope was to be assessed on the force-map of the sample.

However, in this study the assessment of the reference slope on the sample area always resulted in adverse reference slope values, by far under 0.8. The visual assessment of the sample area, by the naked eye and with the microscope, revealed a thin film of chemical residues covering the sample slide in all cases. In fact, residues precipitated on the surface already during the reconstitution process of *in vitro* generated fibrils (Figure 31), and additional contaminations adhered on the surface during mineralization steps of both native and reconstituted samples (Figure 32). Therefore, the measured material on the substrate surface was not homogeneous and infinitely hard and stiff, so that reference slopes were appeared softer than on a truly hard surface. Similarly, because the measured surface did not provide sufficient consistency for sensitivity values, the calibration process (see 3.3.5.3) did not converge to an end-value in PBS, but drifted in every iteration step to a diverging result. Thus, the sensitivity calibration could not be carried out successfully, and also had to be done elsewhere. Switching the substrate slide to a new glass slide on every occasion was no option, because every environmental change resulted in a change of the apparent sensitivity, which again would have required a new sensitivity calibration after switching back to the original sample slide.

Hence, the clean calibration surface had to be provided on the sample slide, in the same fluid cell where the sample fibrils laid. The alternative mica disk setup (Figure 33), as described in 3.3.5.3 was then used for every sample.

The use of the mica disk provided a new clean and atomically plain surface after every treatment step which included immersing the sample in chemical fluids. After drying the area of the mica disk, the upper surface and several other underlying layers of the mica were removed by an adhesive tape, so that a clean new surface was revealed. Thus, the initial sensitivity calibration could take place inside the fluid cell on the sample slide by driving the head away from the sample onto the mica.

Furthermore, reference slopes could be captured henceforth after every fibril measurement by bringing the cantilever to the mica and back to the sample area, without moving the AFM head or changing the environment. If reference slope values lay outside of the 0.9 – 1.1 range, an instant recalibration of the sensitivity could take place on the mica (in that case, the respective fibril segments had to be measured again with the recalibrated sensitivity). This method proved to be successful in yielding feasible data.

6.2.5. Interference in the optical lever mechanism

The laser interference phenomenon, described in 3.4.4, occurred frequently after measuring in PBS for some time. The approach part of the D/Z plot, which supposed to be a flat signal (as seen on Figure 18 a-b), appeared as a regular sinusoidal wave form (Figure 35). If this phenomenon occurred, it occurred for an entire measurement day, that is, at all sample fibril segments of one stage of the experimental session, corresponding to the adjusted preferences and calibration which were preliminary set for that measurement day.

The reason for a sinusoidal wave signal in the deflection signal was the interference of the light waves of the laser. That is, if the laser beam was positioned close to the edge of the tapered end of the cantilever, peripheral waves of the AFM laser passed by the edge. These light waves were then eventually reflected from the sample slide surface. Thereby, on the detector plane they interfered with the working laser beam reflected by the cantilever surface, creating a superimposed wave signal on the baseline of the deflection-displacement plot (Figure 36).

This artifact could be resolved by repositioning the laser beam on the cantilever further towards the stem of the cantilever, with safe distance from its tapered end. Generally, there was enough free cantilever surface for this, considered that even a position up to the half of the cantilever length maintains the accuracy and sensitivity in detecting the right cantilever deflection [61].

6.2.6. Indentation depth

The artifact, which induced the improvement of the final cantilever choice and force calibration process (see 3.3.6.1), was that the indentation depth on reconstituted fibrils highly exceeded the correct limit of 10% height: mostly 20-30% were observed using cantilever A.

This also elicited another artifact, namely it was observed after 1-2 measurement steps (PBS & Min0), that in the next stage, crystalline contaminations were excessively present at fibril segments indented before. This can be explained by the crater traces which were left by a too deep indentation on these segments, and which may have provided a favorable spot for large-scale crystallization. Based on the finally developed calibration loop process (Figure 27), the softer cantilever B was determined to be appropriate on the reconstituted fibrils, indenting under 10% depth of the fibril height. Thus, this artifact could be resolved.

6.2.7. Data analysis algorithm

The algorithm by ANDRIOTIS et al. [39] is a reproducible and effective tool to evaluate indentations. It works most accurately on unmineralized fibril samples with smooth surfaces. However, in case of mineralized fibrils, artifacts and errors often occurred during the algorithm. This was due to the identification of the highest point of a cross section in the first place. As suggested by ANDRIOTIS et al, and the indentation assumptions, force curves shall be captured at the spine of a fibril [39]. In case of mineralized fibrils, mineral contamination and crystal inserts often affected the identification of the highest point: at several cross sections, the chosen force curve is an indentation on the spike of a residing mineral. That either produced an extremely high modulus (hard surface), or a softer outlier value (if the crystal moved under load, or the indenter tip slid down on the crystal). This issue in the algorithm could not be resolved in the course of this thesis, only the resulting erroneous indentations could be manually captured and eliminated from the final dataset. Thereby, important indentations (on stiffer, mineralized locations) might have been cancelled from the data analysis (Figure 57).

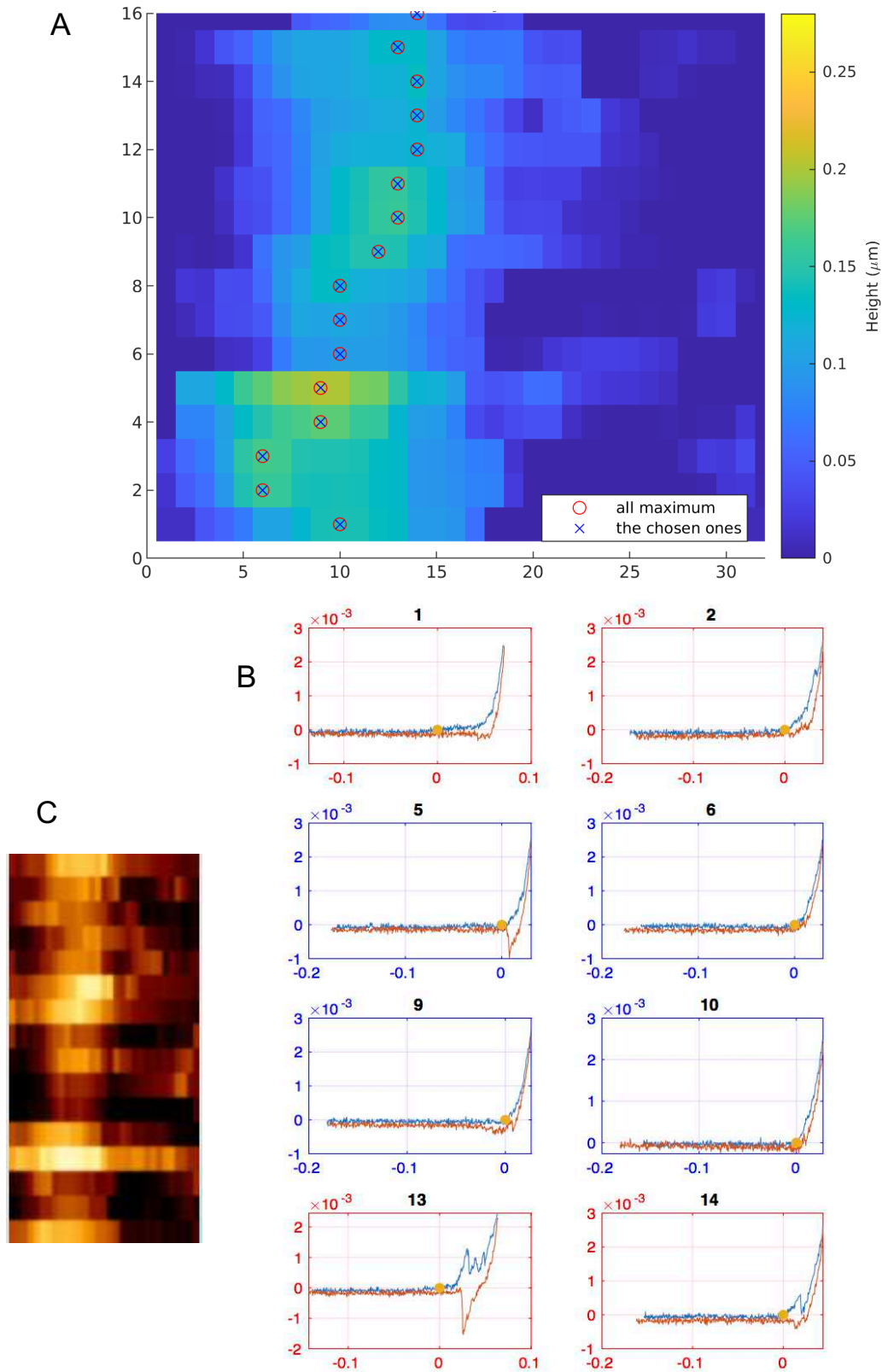


Figure 57: Fibril 2 of sample A1 in the Min1 stage. A - Height map captured by indentation, marking the 16 indentations at the highest points. C - Force map of the indentation, illustrating the stiffer regions on the fibril by brighter colors. B - 8 indentation plots of 16. Discarded indentations are marked by red.

6.3. Assumptions

The following assumptions were maintained, primarily to comply with the Oliver-Pharr and Hertzian indentation principles: the indenter was considered to be a rigid punch, since the expected indentation modulus of the sample lies in the 10^0 MPa order of magnitude, while in comparison the indenter tip (silicon-nitride) has a Young's modulus of 10^5 MPa order of magnitude. The cantilever spring constant was of the same order of magnitude ($10^{-1} - 10^{-2}$ N/m) as the expected contact stiffness. For instance, BALDWIN et al. used a 0.25 N/m cantilever for hydrated fibrils [24], similar to our cantilever A, with measured spring constants (3.3.5.2) lying in the range of 0.25 – 0.27 N/m.

The deformation during the indentation was elastic, and the sample could be considered as an elastic-plastic half-space in which the indentation takes place, because the indenter tip radius (< 5 nm) was at least ten times smaller than the fibril radii (> 50 nm). Additionally, the indentation depth was controlled to remain under 10% of the actual fibril height. The sample material was assumed as homogeneous, transversely isotropic, and linear (no time-dependent behavior). However, this assumption is only partially fulfilled, as collagen in fact demonstrates non-linear, viscoelastic behavior [58]. Apart from that, homogeneity could be assumed in dependence of the size of inhomogeneities. At low indentation speeds, the viscoelastic behavior does not take a remarkable effect. In our case, the maximum speed was 2000 nm/s, well below the threshold of 10000 nm/s suggested by BALDWIN et al. [24].

It was found that 10 indentations along the fibril width are sufficient to have an indent on the fibril crest at its peak height, as also suggested by ANDRIOTIS. With 10 indentations per fibril width, the duration of the experiments was also optimized and the tip lifetime was lengthened. Regarding the accuracy of data, some errors could be already captured during the calculations, by the assessment of the D/Z slopes. The raw value of the D/Z ratio was registered in every indentation point. According to the analysis of KAIN et al. [60], the optimal sensitivity/error ratio on collagen fibrils occurs at $D/Z = 0.414$. Sufficient accuracy lies in $0.2 < D/Z < 0.8$. A too soft DZ slope signaled that at the particular indentation point the fibril was softer than what was calibrated for. Also, when the indentation point was too stiff with regard to the calibrated cantilever, the terminal force was reached earlier, at a smaller depth, than the other indentations. Thereby, the subtraction of the small Z-displacement and deflection signal values resulted in low signal-to-noise ratio, when calculating the indentation depth dh (Equation 2).

Based on the Shapiro-Wilk tests conducted on the population of indentations of each individual fibril in each step, the data on each fibril was considered normally distributed.

7. Conclusion

In this study, the mechanical properties of collagen fibrils were investigated *in vitro* in different stages of mineralization. Reconstituted and native collagen Type I fibrils were measured by AFM nanoindentation for their indentation modulus, in their unmodified state and after repeated steps of mineralization *in vitro*. The expected outcome of this investigation was the change in mechanical properties of the fibrils across multiple mineralization stages. Yet, the emerged findings mainly relate to the application of chemical and nanomechanical methods themselves.

For instance, the use of a mica disc as a supplemental clean surface for sensitivity calibration and reference slope determination proved to be utmost successful, as it can provide a pure fresh surface next to the sample after a chemical treatment with high precipitation potential.

By employing the same AFM cantilever under the same environmental conditions, the indentation modulus of a sample could be well compared in different stages of modification. The results suggest that a sample of reconstituted fibrils could well resemble the mechanical properties of native fibrils, and even provides less variance among fibrils than a native sample. However, the morphological (diameter) and mechanical properties on one individual fibril segment have a much higher variety on a reconstituted fibril, than on a native fibril.

The formation of crystals by the employed protocol could be observed on all examined samples. However, the effect of mineralization inside the fibrils could not be verified by mechanical tests. Crystals formed in a large part on the fibrils, covering eventual modified features inside the fibrils. Thus, the contaminations mostly prohibited a proper indentation of the fibrils, and the resolving EDTA rinse might have again had influence on the inner crystallization. Therefore, tensile tests might provide better result for the future examination of mechanical properties of mineralized fibrils, avoiding the influence of surface contaminations. Additionally, the change of the test protocol towards shorter incubation and rinsing times might restrain the effect of excessive crystallization and precipitations.

The observation of the stiffening effect of mineralization might have also been prohibited by the absence of important non-collagenous proteins in reconstituted and native (mice tendon) samples, which would catalyze intrafibrillar mineralization. Using samples of formerly demineralized fibrils might yield better results in the future.

Bibliography

- [1] H. Follet, G. Boivin, C. Rumelhart, and P. . Meunier, “The degree of mineralization is a determinant of bone strength: a study on human calcanei,” *Bone*, vol. 34, no. 5, pp. 783–789, May 2004.
- [2] G. Boivin *et al.*, “The role of mineralization and organic matrix in the microhardness of bone tissue from controls and osteoporotic patients,” *Bone*, vol. 43, no. 3, pp. 532–538, Sep. 2008.
- [3] Y. Bala, D. Farlay, and G. Boivin, “Bone mineralization: from tissue to crystal in normal and pathological contexts,” *Osteoporos. Int.*, vol. 24, no. 8, pp. 2153–2166, Aug. 2013.
- [4] J. García-Rodríguez and J. Martínez-Reina, “Elastic properties of woven bone: effect of mineral content and collagen fibrils orientation,” *Biomech. Model. Mechanobiol.*, vol. 16, no. 1, pp. 159–172, Feb. 2017.
- [5] Y. Wang and A. Ural, “Effect of modifications in mineralized collagen fibril and extra-fibrillar matrix material properties on submicroscale mechanical behavior of cortical bone,” *J. Mech. Behav. Biomed. Mater.*, vol. 82, pp. 18–26, Jun. 2018.
- [6] G. J. Tortora and B. Derrickson, *Principles of Anatomy and Physiology*, 13th editi. USA: Wiley, 2012.
- [7] C. N. Maganaris and J. P. Paul, “*In vivo* human tendon mechanical properties,” *J. Physiol.*, vol. 521, no. 1, pp. 307–313, Nov. 1999.
- [8] P. Fratzl, “Collagen: Structure and mechanics, an introduction,” in *Collagen: Structure and Mechanics*, Springer US, 2008, pp. 1–13.
- [9] J. F. Vincent and J. D. Currey, *The Mechanical properties of biological materials*. Cambridge: Published for the Society for Experimental Biology by Cambridge University Press, 1980.
- [10] S. Weiner and H. D. Wagner, “THE MATERIAL BONE: Structure-Mechanical Function Relations,” *Annu. Rev. Mater. Sci.*, vol. 28, no. 1, pp. 271–298, Aug. 1998.
- [11] V. Cvetkovic *et al.*, “A comparison of the microarchitecture of lower limb long bones between some animal models and humans: a review,” *Vet. Med. (Praha)*, vol. 58, no. No. 7, pp. 339–351, Aug. 2013.
- [12] C. Hellmich and F. Ulm, “Average hydroxyapatite concentration is uniform in the extracollagenous ultrastructure of mineralized tissues : evidence at the 1 – 10- 1 m scale,” vol. 2, pp. 21–36, 2003.
- [13] P. J. Thurner, “Atomic force microscopy and indentation force measurement of bone,” *Wiley Interdiscip. Rev. Nanomedicine Nanobiotechnology*, vol. 1, no. 6, pp. 624–649, Nov. 2009.
- [14] F. A. Shah, P. Thomsen, and A. Palmquist, “Osseointegration and current interpretations of the bone-implant interface,” *Acta Biomater.*, vol. 84, pp. 1–15, Jan. 2019.
- [15] G. Boivin and P. J. Meunier, “The Degree of Mineralization of Bone Tissue Measured by Computerized Quantitative Contact Microradiography,” *Calcif. Tissue Int.*, vol. 70, no. 6, pp. 503–511, Jun. 2002.
- [16] P. Roschger, E. P. Paschalis, P. Fratzl, and K. Klaushofer, “Bone mineralization density distribution in health and disease,” *Bone*, vol. 42, no. 3, pp. 456–466, Mar. 2008.
- [17] M. Xue and C. J. Jackson, “Extracellular Matrix Reorganization During Wound Healing and Its Impact on Abnormal Scarring,” *Adv. Wound Care*, vol. 4, no. 3, pp. 119–136, Mar. 2015.

- [18] K. E. Kadler, C. Baldock, J. Bella, and R. P. Boot-Handford, “Collagens at a glance.,” *J. Cell Sci.*, vol. 120, no. Pt 12, pp. 1955–8, Jun. 2007.
- [19] K. E. Kadler, D. F. Holmes, J. A. Trotter, and J. A. Chapman, “Collagen fibril formation.,” *Biochem. J.*, vol. 316 (Pt 1, no. 1, pp. 1–11, May 1996.
- [20] M. H. Ross and W. Pawlina, *Histology : a text and atlas : with correlated cell and molecular biology*. Wolters Kluwer/Lippincott Williams & Wilkins Health, 2011.
- [21] C. A. Grant, D. J. Brockwell, S. E. Radford, and N. H. Thomson, “Effects of hydration on the mechanical response of individual collagen fibrils,” *Appl. Phys. Lett.*, vol. 92, no. 23, p. 233902, Jun. 2008.
- [22] O. G. Andriotis *et al.*, “Structure-mechanics relationships of collagen fibrils in the osteogenesis imperfecta mouse model,” *J. R. Soc. Interface*, 2015.
- [23] O. G. Andriotis, S. Desissaire, and P. J. Thurner, “Collagen Fibrils: Nature’s Highly Tunable Nonlinear Springs,” *ACS Nano*, vol. 12, no. 4, pp. 3671–3680, Apr. 2018.
- [24] S. J. Baldwin, A. S. Quigley, C. Clegg, and L. Kreplak, “Nanomechanical mapping of hydrated rat tail tendon collagen i fibrils,” *Biophys. J.*, 2014.
- [25] Z. L. Shen, “Tensile Mechanical Properties of Isolated Collagen Fibrils Obtained by Microelectromechanical Systems Technology,” Case Western Reserve University, 2010.
- [26] J. A. J. van der Rijt, K. O. van der Werf, M. L. Bennink, P. J. Dijkstra, and J. Feijen, “Micromechanical Testing of Individual Collagen Fibrils,” *Macromol. Biosci.*, vol. 6, no. 9, pp. 697–702, Sep. 2006.
- [27] A. L. Fidler, S. P. Boudko, A. Rokas, and B. G. Hudson, “The triple helix of collagens - an ancient protein structure that enabled animal multicellularity and tissue evolution.,” *J. Cell Sci.*, vol. 131, no. 7, p. jcs203950, Apr. 2018.
- [28] K. L. Goh, A. Listrat, and D. Béchet, “Hierarchical mechanics of connective tissues: Integrating insights from nano to macroscopic studies,” *J. Biomed. Nanotechnol.*, vol. 10, no. 10, pp. 2464–2507, 2014.
- [29] A. J. Hodge and J. A. Petruska, “Recent studies with the electron microscope on ordered aggregates of the tropocollagen macromolecule,” *G N Ramachandran, Ed. Asp. Protein Struct. Proc. a Symp. p.*, Mar. 1963.
- [30] D. J. Hulmes, T. J. Wess, D. J. Prockop, and P. Fratzl, “Radial packing, order, and disorder in collagen fibrils,” *Biophys. J.*, vol. 68, no. 5, pp. 1661–1670, 1995.
- [31] F. H. Silver, J. W. Freeman, and G. P. Seehra, “Collagen self-assembly and the development of tendon mechanical properties,” *J. Biomech.*, vol. 36, no. 10, pp. 1529–1553, Oct. 2003.
- [32] Z. Xu *et al.*, “Molecular mechanisms for intrafibrillar collagen mineralization in skeletal tissues,” *Biomaterials*, vol. 39, pp. 59–66, Jan. 2015.
- [33] M. J. Glimcher, “The nature of the mineral component of bone and the mechanism of calcification.,” *Instr. Course Lect.*, vol. 36, pp. 49–69, 1987.
- [34] F. Nudelman, A. J. Lausch, N. A. J. M. Sommerdijk, and E. D. Sone, “In vitro models of collagen biomineralization,” *J. Struct. Biol.*, vol. 183, no. 2, pp. 258–269, Aug. 2013.
- [35] W. J. Landis, J. J. Librizzi, M. G. Dunn, and F. H. Silver, “A study of the relationship between mineral content and mechanical properties of turkey gastrocnemius tendon,” *J. Bone Miner. Res.*, vol. 10, no. 6, pp. 859–867, Jun. 1995.
- [36] H. J. Lei, Z. Q. Zhang, F. Han, B. Liu, Y.-W. Zhang, and H. J. Gao, “Elastic Bounds of Bioinspired Nanocomposites,” *J. Appl. Mech.*, vol. 80, no. 6, Nov. 2013.
- [37] F. Nudelman *et al.*, “The role of collagen in bone apatite formation in the presence of hydroxyapatite nucleation inhibitors.,” *Nat. Mater.*, vol. 9, no. 12, pp. 1004–9, Dec. 2010.

- [38] B. Depalle, Z. Qin, S. J. Shefelbine, and M. J. Buehler, “Large Deformation Mechanisms, Plasticity, and Failure of an Individual Collagen Fibril With Different Mineral Content,” *J. Bone Miner. Res.*, vol. 31, no. 2, pp. 380–390, Feb. 2016.
- [39] O. G. Andriotis *et al.*, “Nanomechanical assessment of human and murine collagen fibrils via atomic force microscopy cantilever-based nanoindentation,” *J. Mech. Behav. Biomed. Mater.*, vol. 39, pp. 9–26, Nov. 2014.
- [40] N. Sasaki and S. Odajima, “Elongation mechanism of collagen fibrils and force-strain relations of tendon at each level of structural hierarchy,” *J. Biomech.*, vol. 29, no. 9, pp. 1131–1136, Sep. 1996.
- [41] A. Gautieri, S. Vesentini, A. Redaelli, and R. Ballarini, “Modeling and measuring viscoelastic properties : From collagen molecules to collagen fi brils.” 2013.
- [42] S. Varma, J. P. R. O. Orgel, and J. D. Schieber, “Nanomechanics of Type I Collagen,” *Biophys. J.*, vol. 111, no. 1, 2016.
- [43] N. Karathanasopoulos, G. Arampatzis, and J.-F. Ganghoffer, “Unravelling the viscoelastic, buffer-like mechanical behavior of tendons: A numerical quantitative study at the fibril-fiber scale,” *J. Mech. Behav. Biomed. Mater.*, vol. 90, pp. 256–263, Feb. 2019.
- [44] Z. L. Shen, M. R. Dodge, H. Kahn, R. Ballarini, and S. J. Eppell, “Stress-Strain Experiments on Individual Collagen Fibrils,” *Biophys. J.*, vol. 95, no. 8, pp. 3956–3963, Oct. 2008.
- [45] C. A. Grant, D. J. Brockwell, S. E. Radford, and N. H. Thomson, “Tuning the elastic modulus of hydrated collagen fibrils,” *Biophys. J.*, 2009.
- [46] M. Schulze, M. Rogge, and R. W. Stark, “Atomic force microscopy measurements probing the mechanical properties of single collagen fibrils under the influence of UV light in situ,” *J. Mech. Behav. Biomed. Mater.*, vol. 88, pp. 415–421, Dec. 2018.
- [47] M. Fielder and A. K. Nair, “Effects of hydration and mineralization on the deformation mechanisms of collagen fibrils in bone at the nanoscale,” *Biomech. Model. Mechanobiol.*, pp. 1–12, Aug. 2018.
- [48] M. Balooch, S. Habelitz, J. H. Kinney, S. J. Marshall, and G. W. Marshall, “Mechanical properties of mineralized collagen fibrils as influenced by demineralization.,” *J. Struct. Biol.*, vol. 162, no. 3, pp. 404–10, Jun. 2008.
- [49] O. Akkus, “Elastic Deformation of Mineralized Collagen Fibrils: An Equivalent Inclusion Based Composite Model,” *J. Biomech. Eng.*, vol. 127, no. 3, p. 383, Jan. 2005.
- [50] J. S. Yerramshetty and O. Akkus, “The associations between mineral crystallinity and the mechanical properties of human cortical bone,” *Bone*, vol. 42, no. 3, pp. 476–482, Mar. 2008.
- [51] D. R. Baselt, J. P. Revel, and J. D. Baldeschwieler, “Subfibrillar structure of type I collagen observed by atomic force microscopy.,” *Biophys. J.*, vol. 65, no. 6, pp. 2644–55, Dec. 1993.
- [52] S. Scheuring, D. Fotiadis, C. Möller, S. A. Müller, A. Engel, and D. J. Müller, “Single Proteins Observed by Atomic Force Microscopy,” *Single Mol.*, vol. 2, no. 2, pp. 59–67, Jul. 2001.
- [53] S. Habelitz, M. Balooch, S. J. Marshall, G. Balooch, and G. W. Marshall, “In situ atomic force microscopy of partially demineralized human dentin collagen fibrils.,” *J. Struct. Biol.*, vol. 138, no. 3, pp. 227–36, Jun. 2002.
- [54] E. A. G. Chernoff and D. A. Chernoff, “Atomic force microscope images of collagen fibers,” *J. Vac. Sci. Technol. A Vacuum, Surfaces, Film.*, vol. 10, no. 4, pp. 596–599, Jul. 1992.
- [55] W. C. Oliver and G. M. Pharr, “Measurement of hardness and elastic modulus by

instrumented indentation: Advances in understanding and refinements to methodology,” 2004.

- [56] D. M. Ebenstein, D. Coughlin, J. Chapman, C. Li, and L. A. Pruitt, “Nanomechanical properties of calcification, fibrous tissue, and hematoma from atherosclerotic plaques,” *J. Biomed. Mater. Res. - Part A*, vol. 91, no. 4, pp. 1028–1037, 2009.
- [57] S. Strasser, A. Zink, M. Janko, W. M. Heckl, and S. Thalhammer, “Structural investigations on native collagen type I fibrils using AFM,” *Biochem. Biophys. Res. Commun.*, vol. 354, no. 1, pp. 27–32, Mar. 2007.
- [58] M. R. Uhlig and R. Magerle, “Unraveling capillary interaction and viscoelastic response in atomic force microscopy of hydrated collagen fibrils,” *Nanoscale*, 2017.
- [59] X. Pang, L. Lin, and B. Tang, “Unraveling the role of Calcium ions in the mechanical properties of individual collagen fibrils,” *Sci. Rep.*, 2017.
- [60] L. Kain *et al.*, “Calibration of colloidal probes with atomic force microscopy for micromechanical assessment,” *J. Mech. Behav. Biomed. Mater.*, vol. 85, no. December 2017, pp. 225–236, 2018.
- [61] G. Haugstad, *Atomic Force Microscopy*. Hoboken, NJ, USA: John Wiley & Sons, Inc., 2012.
- [62] S. J. Eppell, B. N. Smith, H. Kahn, and R. Ballarini, “Nano measurements with micro-devices: mechanical properties of hydrated collagen fibrils,” *J. R. Soc. Interface*, vol. 3, no. 6, pp. 117–21, Feb. 2006.
- [63] C. Burns, “In Vitro Reconstitution and Mineralisation of Collagen Fibrils,” Vienna University of Technology, 2018.
- [64] P. A. Price, D. Toroian, and J. E. Lim, “Mineralization by inhibitor exclusion. The calcification of collagen with fetuin,” *J. Biol. Chem.*, 2009.
- [65] S. L.-Y. Woo, M. A. Gomez, Y.-K. Woo, and W. H. Akeson, “Mechanical properties of tendons and ligaments,” *Biorheology*, vol. 19, no. 3, pp. 397–408, Jun. 1982.
- [66] J. McElhaney, *Dynamic mechanical properties of scalp and brain*. 1969.
- [67] K. Miller and K. Chinzei, “Mechanical properties of brain tissue in tension,” *J. Biomech.*, vol. 35, no. 4, pp. 483–490, 2002.
- [68] T. Katoh, M. P. Griffin, H. W. Wevers, and J. Rudan, “Bone hardness testing in the trabecular bone of the human patella,” *J. Arthroplasty*, vol. 11, no. 4, pp. 460–8, Jun. 1996.
- [69] T. M. Wright and W. C. Hayes, “Tensile testing of bone over a wide range of strain rates: effects of strain rate, microstructure and density,” *Med. Biol. Eng.*, vol. 14, no. 6, pp. 671–680, Nov. 1976.
- [70] M. T. Abba, “Spherical Nanoindentation Protocols for Extracting Microscale Mechanical Properties in Viscoelastic Materials Spherical Nanoindentation Protocols for Extracting Microscale Mechanical Properties in,” no. December, 2015.
- [71] JPK Instruments, “JPK Instruments AG- NanoWizard3 User Manual. SPM Software Release 4.2,” 2012.
- [72] G. Thomas, N. A. Burnham, T. A. Camesano, and Q. Wen, “Measuring the Mechanical Properties of Living Cells Using Atomic Force Microscopy,” *J. Vis. Exp.*, no. 76, pp. 1–8, 2013.
- [73] G. M. Pharr and A. Bolshakov, “Understanding nanoindentation unloading curves,” 2002.
- [74] S. M. Cook, K. M. Lang, K. M. Chynoweth, M. Wigton, R. W. Simmonds, and T. E. Schäffer, “Practical implementation of dynamic methods for measuring atomic force microscope cantilever spring constants,” *Nanotechnology*, vol. 17, no. 9, pp. 2135–2145, May 2006.
- [75] M. P. E. Wenger, L. Bozec, M. A. Horton, and P. Mesquida, “Mechanical properties of

collagen fibrils.,” *Biophys. J.*, vol. 93, no. 4, pp. 1255–63, Aug. 2007.

- [76] H. Hertz, *Miscellaneous papers*. London ;;New York: MacMillan and Co., 1896.
- [77] J. L. Hutter and J. Bechhoefer, “Calibration of atomic-force microscope tips,” *Rev. Sci. Instrum.*, vol. 64, no. 7, pp. 1868–1873, Jul. 1993.
- [78] D. J. Keller and F. S. Franke, “Envelope reconstruction of probe microscope images,” *Surf. Sci.*, vol. 294, no. 3, pp. 409–419, Sep. 1993.
- [79] C. L. Jenkins, L. E. Bretscher, I. A. Guzei, and R. T. Raines, “Effect of 3-hydroxyproline residues on collagen stability,” *J. Am. Chem. Soc.*, vol. 125, no. 21, pp. 6422–6427, May 2003.
- [80] S. Xu, M. Gu, K. Wu, and G. Li, “Unraveling the Role of Hydroxyproline in Maintaining the Thermal Stability of the Collagen Triple Helix Structure Using Simulation,” *J. Phys. Chem. B*, vol. 123, no. 36, pp. 7754–7763, Sep. 2019.

Annex A - Mineralization protocol

(Ciara Burns, [63])

MATERIALS

CHEMICALS:

- Di-Sodium hydrogen phosphate dihydrate ($\text{Na}_2\text{HPO}_4 \cdot 2\text{H}_2\text{O}$; Carl Roth, Article No.: T877.2)
- Distilled water
- Calcium chloride (CaCl_2 ; Carl Roth, Article No.: CN93.1)
- HEPES (SIGMA Aldrich, Article No. H3375-100g)
- Fetuin (SIGMA Aldrich, Article No. F3385-100MG)

EQUIPMENT:

- Piston pipett (100-1000 μL ; Item No.:_EP 3123000063)
- Compressor (OMA, Article No.: ICO P20)
- Bellows
- Petri dishes.

BUFFER PREPERATION

Buffer C: $\text{Na}_2\text{HPO}_4 \cdot 2\text{H}_2\text{O}$ (10mM) + HEPES (0,2M)

Adjusted to pH 7,4

Buffer D: CaCl_2 (10mM) + HEPES (0,2M)




Adjusted to pH 7,4

Buffer E: Mix 10mL of Buffer C, 10 mL of Buffer D and 20 mg fetuin until the fetuin is completely dissolved.

PROCEDURE Timing: 25h



MINERALISATION REQUIRES SUCCESSFUL IN VITRO RECONSTRUCTION OF NATIVE COLLAGEN FIBRILS

- 1| Place glass slides with previously reconstructed collagen fibrils in a petri dish.
- 2| Place 200 - 300 μL of mineralisation buffer on the glass slide.
 **CRITICAL STEP:** Make sure to use enough volume, to prevent solution from drying on the glass slide.
- 3| Leave for 24h.
 **PAUSE POINT**
- 4| Rinse remaining solution from the glass slide with distilled water.
 **CRITICAL STEP:** Make sure not to direct the stream right into the centre of the area where the solution was placed.

5| Dry remaining solution from the glass slide.

▲ **CRITICAL STEP:** Make sure not to direct the air stream right into the centre of the area where the solution was placed. The fibrils might be blown away.

↕ **VARIATION STEP:**

5.1| Dry glass slide with compressor.

5.2| Dry glass slide with glass bellows.

Reference:

F Nudelman, K Pieterse, A George, PHH Bomans, H Friedrich, LJ Brylka, PAJ Hilbers, NAJM Sommerdijk. The role of collagen in bone apatite formation in the presence of hydroxyapatite nucleation inhibitors. *Nature materials*, 9(12):1004-1009, 2010.

Annex B - Reconstitution protocol

(Ciara Burns, [63])

MATERIALS

CHEMICALS:

- Di-Sodium hydrogen phosphate dihydrate ($\text{Na}_2\text{HPO}_4 \cdot 2\text{H}_2\text{O}$; Carl Roth, Article No.: T877.2)
- Distilled water
- Potassium chloride (KCl; Carl Roth, Article No.: 6781.3)
- Collagen Monomer: 3mg/ml in 0.01 N HCl (Advanced Bio Matrix, Article No.: 5005)

EQUIPMENT:

- Microfuge tube (1,5 mL; Carl Roth, Article No.: AET8.1)
- Glass slides (VWR, Article No.: 631-1553)
- Heatblock (Labnet International Inc., SKU.: I5110-230V)
- Piston pipett (0,5-10 μL ; Item No.:_EP 3123000020)
- Piston pipett (10-100 μL ; Item No.:_EP 3123000020)
- Vortex with microfuge shaking accessory (VWR International, Type VV3)
- Compressor (OMA, Article No.: ICO P20)
- Bellows

BUFFER PREPERATION

Buffer A: $\text{Na}_2\text{HPO}_4 \cdot 2\text{H}_2\text{O}$, 200 mM, adjusted to pH 7

Buffer B: KCl, 400 mM

PROCEDURE Timing: 6h

- 1| Preheat the heatblock to 37°C.
- 2| Transfer 6 μL of distilled water into microfuge tube.
- 3| Transfer 20 μL of Buffer A into the same microfuge tube.
- 4| Transfer 10 μL of Buffer B also into the same microfuge tube.
- 5| Transfer 4 μL of collagen monomer into the same microfuge tube.
- 6| Mix the content of the microfuge tube thoroughly.



VARIATION STEP:

- 6.1| Mix with Piston pipett.
- 6.2| Mix with Vortex.

7| Place microfuge tube in the heatblock for 3 – 4 h.

■ PAUSE POINT

8| Prepare as many glass slides as required samples.

9| Place glass slides into a petri dish.

10| Remove microfuge tube from heatblock.

11| Place a drop of 5 - 20 μ L on each glass slide.

▲ **CRITICAL STEP:** Make sure to use enough volume, to prevent solution from drying on the glass slide. If it dries crystal formation will prevent fibril formation.

12| Let fibrils settle on the glass slide for 5 min – 1h.

■ PAUSE POINT

13| Rinse remaining solution from the glass slide with distilled water.

▲ **CRITICAL STEP:** Make sure not to direct the stream right into the centre of the area where the solution was placed.

14| Dry remaining solution from the glass slide.

▲ **CRITICAL STEP:** Make sure not to direct the air stream right into the centre of the area where the solution was placed. The fibrils might be blown away.

↕ **VARIATION STEP:**

13.1| Dry glass slide with compressor.

13.2| Dry glass slide with glass bellows.